High-Energy Astrophysics with Neutrino Telescopes

T. Chiarusi and M. Spurio

Dipartimento di Fisica dell'Università di Bologna and INFN

Viale Berti Pichat 6/2 - 40127 Bologna (Italy)

Abstract

Neutrino astrophysics offers new perspectives on Universe investigation: high energy neutrinos, produced by the most energetic phenomena in our Galaxy and in the Universe, carry complementary (if not exclusive) information about the Cosmos with respect to photons.

While the small interaction cross section of neutrinos allows them to come from the core of astrophysical objects, it is also a draw-back, as their detection requires a large target mass. This is why it is convenient to place neutrino telescopes in natural locations, like deep underwater or under-ice sites. In order to supply for such extremely hostile environmental conditions, new frontiers technologies are under development.

The aim of this work is to review the motivations for high energy neutrino astrophysics, the physics and the technologies used in underwater/ice Cherenkov experiments, with a special focus on the project of the construction of a km^3 scale detector in the Mediterranean Sea.

1 Introduction

The recent years have seen spectacular astrophysical discoveries using new experimental techniques or new photons wavelengths (for instance the TeV gamma astronomy using Imaging Air- Cherenkov Technique). High energy neutrino astronomy is a young discipline derived from the fundamental necessity of extending conventional astronomy beyond the usual electro-magnetic messengers.

One of the main questions in astroparticle physics is the origin and nature of high-energy cosmic rays, CRs (§2). It was discovered at the beginning of the last century that energetic charged particles strike the Earth and produce showers of secondary particles in the atmosphere. While the energy spectrum of the cosmic rays can be measured up to very high energies, their origin remains unclear. There are many indications of the Galactic origin of the CR bulk (protons and other nuclei up to $\sim 10^{15} \div 10^{16}$ eV), although it is not possible to directly correlate the CR impinging directions on Earth to astrophysical sources since CRs are generally deflected by the galactic magnetic fields. However, the highest energy CRs are probably originated from extragalactic sources, as indicated by recent measurements (§2.1.3). Protons with $E > 10^{19}$ eV interact with the cosmic microwave background. This effect, known as the Greisen-Zatsepin-Kuzmin cutoff, limits the origin of high energy protons to a small fraction of the Universe, of the order of 100 Mpc.

Assuming that at acceleration sites a fraction of the high-energy CRs interact with the ambient matter or photon fields, pions and then γ-rays and neutrinos are be created. Recent advances on ground-based γ-ray astronomy have led to the discovery of more than 80 sources of TeV gamma-rays, as described in §3. Candidates for neutrino sources are in general also TeV γ-ray sources. The *astrophysical hadronic models* describe the mechanisms which lay behind the production of neutrinos and high energy photons from CR interactions with the propagation medium. The energy spectrum of secondary particles follows the same power law of the progenitor CRs. For this reason it is possible to put constraints to the expected neutrino flux from sources where γ-rays are observed.

While the small interaction cross section of neutrinos allows them to come from far away, it is also a draw-back, as their detection requires a large target mass. The idea of a neutrino telescope based on the detection of the secondary particles produced in neutrino interactions was first formulated in the 1960s by Markov [1]. He proposed *to install detectors deep in a lake or in the sea and to determine the direction of the charged particles with the help of Cherenkov radiation*. The detection of neutrinos is mainly based on the detection of muons which are created in the charged-current interactions of muon-neutrinos (§4). These muons, at sufficiently high-energies (§4.1), retain information on the direction of the incident neutrino and can traverse several kilometers of ice or water (§4.2) . Along their trajectory, the muons emit Cherenkov light. From the measured arrival time of the Cherenkov light (§4.3), the direction of the muon can be determined. This process is referred to as muon track reconstruction.

As we will show in §5, starting from the Markov idea and from the present knowledge of TeV γ-rays astronomy, a kilometer-scale detector is needed to detect cosmic neutrinos. We derive also in a simple way that the number of optical sensors required to reconstruct muon tracks is of the order of 5000.

The models of neutrino production, mainly connected to the recent observational results on γ-ray astronomy, are highlighted in §6. Potential sources of high-energy neutrinos include both Galactic sources (supernova remnants, microquasars,..) and extragalactic sources (active galactic nuclei, gamma-ray burstsers). The prediction of high energy neutrino sources of extra-Galactic origin is a direct consequence of the UHE CR observations.

This connection between CRs, neutrinos and γ-rays can also be used (§6.2) to put upper bounds on the expected neutrino flux from extragalactic sources, since the neutrino energy generation rate will never exceed the generation rate of high energy protons.

The properties of water and ice connected to the possibility of detecting high energy neutrinos are discussed in §7. The pioneering project for the construction of an underwater neutrino telescope was due to the DUMAND collaboration [2], which attempted to deploy a detector off the coast of Hawaii in the 1980s (§8). At the time technology was not advanced enough to overcome these challenges and the project was cancelled. In parallel, the BAIKAL collaboration [3] started to work in order to realize a workable detector systems under the surface of the frozen Baikal lake.

Regarding deep ice, a major step towards the construction of a large neutrino detector (see §9) is due to the AMANDA collaboration [4]. AMANDA deployed and operated the optical sensors under the ice surface of the Antarctic starting from 1993. After the completion of the detector in 2002, the AMANDA collaboration proceeded with the construction of a much larger apparatus, IceCube. 59 of the 80 scheduled strings (April 2009) are already buried in the ice. Completion of this detector is expected to be around 2011.

In water, the pioneering DUMAND experience is being continued in the Mediterranean Sea by the ANTARES [5], NEMO [6] and NESTOR [7] collaborations, which demonstrated the detection technique (see §10). In particular, the ANTARES collaboration has completed (May 2008) the construction of the largest neutrino telescope (~ 0.1 km^2) in the Northern hemisphere, currently under data tacking. These project has lead to a common design study towards the construction of a km^3-scale detector in the Mediterranean Sea (§11). KM3NeT [8] is an European deep-sea research infrastructure, which will host a neutrino telescope with a volume of at least one cubic kilometre at the bottom of the Mediterranean Sea that will open a new window on the Universe.

In the following, we review most of the aspects regarding the phenomenology of neutrino astrophysics, and the status and future prospective of Cherenkov telescopes.

2 The connection among primary Cosmic Rays, γ rays and neutrino astronomy

2.1 Primary Cosmic Rays

Cosmic Rays (CRs) are mainly high energy protons (Fig. 1) and heavier nuclei which are constantly hitting the upper shells of the Earth's atmosphere. The energy spectrum spans from $\sim 10^9$ eV to more than 10^{20} eV, is of non-thermal origin and follows a broken power-law of the form:

$$\left[\frac{dN_P}{dE}\right]_{obs} = K \cdot E^{-\alpha} \tag{1}$$

Direct or *indirect* techniques are used to measure the CR spectrum. The measured power-low spectrum of CRs (eq. 1) is characterized by an index $\alpha = 2.7$ up to energies of roughly 3×10^{15} eV. Most likely, Galactic supernova remnants are the sources responsible for the acceleration of particles. After 3×10^{15} eV, the index becomes $\alpha = 3.1$. This feature in the energy spectrum is known as the $knee$. There is no consensus on a preferred accelerator model for energies above the $knee$ up to 10^{19} eV, where there is a flattening in the spectrum denoted as the $ankle$.
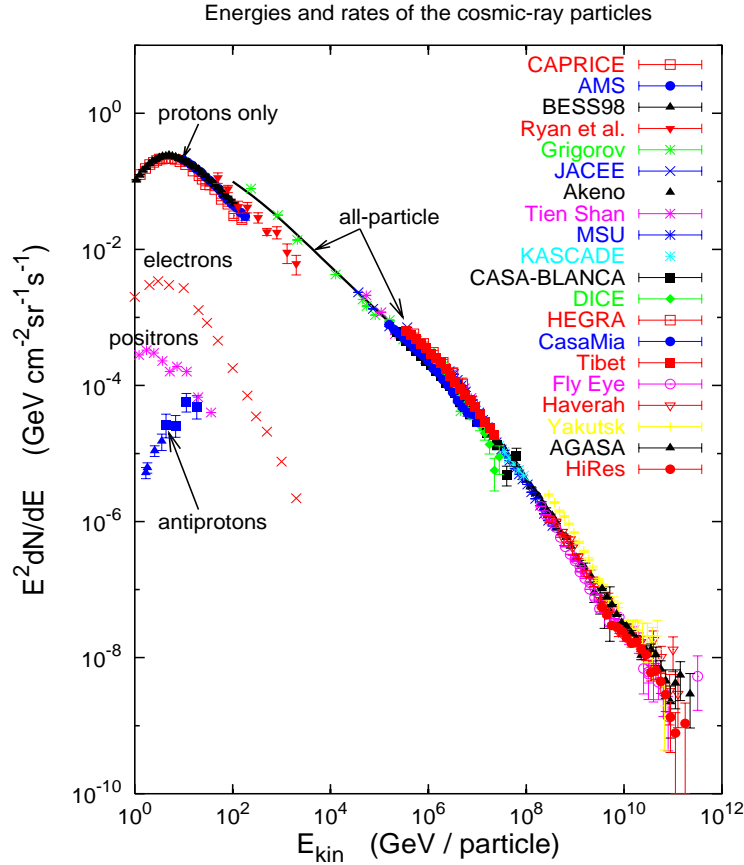
Figure 1: *Cosmic Ray spectrum from 10^9 to 10^{21} eV as measured on Earth, from [9]. Note that the vertical scale has been multiplied by E^2. On the low-energy domain, when the measurements are available, the contribution of protons, electrons, positrons and antiprotons it is also reported. Go to [9] for the reference to the experiments.*

The highest CRs exceed even 10^{20} eV. After the *ankle*, it is generally assumed that CR sources are of extragalactic origin. The experimental search for sources of these ultra high energy CRs has recently entered a very hot phase. Detailed reviews of the theory and measurement of the primary CR spectrum are in [10, 11, 12].

2.1.1 Below the *knee*

Up to energies of 10^{14} eV, the CR spectrum is directly measured above the atmosphere. Stratospheric balloons or satellites have provided the most relevant information about the composition of CRs in the Galaxy and had contributed to establish the standard model of Galactic CRs. Measurements show that $\sim 90\%$ are protons, $\sim 9\%$ are Helium nuclei and $\sim 1\%$ are heavier nuclei.

In this energy range, the mechanism responsible for the acceleration of particles is the Fermi mechanism [13, 14]. This mechanism explains particle acceleration by iterative scattering processes of charged particles in a shock-wave. These shock-waves are originated in

environments of exceptional disruptive events, like stellar gravitational collapses. In each scattering process, a particle with energy E gets an energy gain of $\Delta E \sim \beta E$, where $\beta \sim 10^{-2}$. Due to the magnetic fields confinement, the scattered particles are trapped inside the acceleration region and have a small probability to escape. This iterative process of acceleration of charged particles is a very appealing scheme for the origin of CRs, since it naturally explains the power law tendency in the spectrum.

Supernova remnants (SNR) in the Galaxy are the most accredited site of acceleration of CRs up to the knee [15], although this theory is not free from some difficulties [16]. The Fermi mechanism in the SNR [17], predicts a power law differential energy spectrum $E^{-\alpha_s}$, with $\alpha_s \sim 2$, and fit correctly the energy power involved in the Galactic cosmic rays of $\sim 5 \times 10^{40}$ erg/s.

The measured spectral index ($\alpha \sim 2.7$) is steeper than the spectrum near the sources, because of the energy dependence of the CR diffusion out of the Galaxy, as explained by the so called *leaky box* [18]. In the leaky box model, particles are confined by galactic magnetic fields ($\overline{B} \sim 3\mu G$) and have a small probability to escape. The gyromagnetic radius for a particle with charge Z, energy E, in a magnetic field B is given by $R \simeq \frac{E}{eZB}$.

The value of R (in parsec) for CRs having energies E expressed in PeV (=10^3 TeV) in the galactic magnetic field B (in μG) is:

$$R(pc) = 10 \cdot E(PeV)/ZB(\mu G) \qquad (2)$$

During propagation high energy particles (at a fixed value of Ze) have higher probability of escaping from the Galaxy due to their larger gyromagnetic radii. As a consequence, an energy-dependent diffusion probability P can be defined. P is experimentally estimated through the measurement of the ratio between light isotopes produced by spallation of heavier nuclei. It was found that $P(E) \sim E^{\alpha_D}$, with the diffusion exponent $\alpha_D \sim 0.6$ [10]. The differential CR flux at the sources is estimated as the convolution of the measured spectrum (1) and the CR escape probability P:

$$\left[\frac{dN_P}{dE}\right]_{sources} \propto \left[\frac{dN_P}{dE}\right]_{obs} \times P(E) \propto E^{-\alpha_{CR}} \qquad (3)$$

with $\alpha_{CR} = \alpha - \alpha_D \sim 2$, as predicted by the Fermi model.

The *knee* of the CR spectrum is still an open question and different models have been proposed to explain this feature [19]. Some models invoke astrophysical reasons: due to the iterative scattering processes involved in the acceleration sites, a maximum energy for the CRs is foreseen. This maximum energy depends on the nucleus charge Ze, and this leads to the prediction of a different energy cut-off for every nucleus type. As a consequence, CRs composition is expected to be proton-rich before the *knee*, and iron-rich after. Other more exotic models try to explain the steepening in the CR flux, for instance the hypothesis of new particle processes in the atmosphere [20].

2.1.2 Between the *knee* and the *ankle*

Above $\sim 10^{14}$ eV, CR measurements are only accessible from ground detection infrastructures. The showers of secondary particles created by interaction of primary CRs in the atmosphere are distributed in a large area, enough to be detected by detector arrays (scintillation counters or water tanks in which charged particles emit Cherenkov light). The energy region around the knee and shortly above has been explored by different experiments, as

for instance KASCADE [21]. Although the experimental techniques are very difficult and have poor resolution, observations of this region of the energy spectrum seem to indicate that the average mass of CRs increases when passing the knee.

The SNR models cannot explain the CRs flux above $\sim 10^{16}$ eV, but there is no consensus on a preferred accelerator model up to 10^{19} eV. CRs can be accelerated beyond the *knee* if, for instance, the central core of the supernova hosts a rotating neutron star. In some models already accelerated particles can also suffer additional acceleration due to its strong variable magnetic fields. The maximum energy cannot exceed $\sim 10^{19}$ eV.

2.1.3   After the $ankle$

The flux above 10^{19} eV, still dominated by protons and nuclei [22], is one particle per kilometer square per year per stereoradian. It has long been assumed [23] that ultra high energy cosmic rays (UHECR) are extragalactic in origin [24], and can be detected only by very large ground-based installations. Therefore, the structure in the CR spectrum above $\sim 10^{19}$ eV (the $ankle$) is usually associated with the appearance of this flatter contribution of extra-galactic CRs. In fact, above the $ankle$ the gyroradius (2) of a proton in the galactic magnetic field exceeds the size of the Galaxy disk (300 pc).

Fig. 2 [25] shows a diagram first produced by Hillas (1984). Hillas derived the maximum energy at which a particle of a given charge can be accelerated, independently of the acceleration mechanism, from the simple argument that the Larmor radius of the particle should be smaller than the R_{kpc} size (in kpc) of the acceleration region. This energy E(EeV) (in units of 10^{18} eV) is given by:

$$E(EeV) \sim \beta Z B_{\mu G} R_{kpc} \tag{4}$$

where β is the velocity of the shock wave in the Fermi model or any other acceleration mechanism. Fig. 2 gives the relation between the required magnetic fields to accelerate protons to 10^{20} eV , 10^{21} eV, and iron to 10^{20} eV, and the dimensions of the astrophysical objects needed to contain the accelerating particle. As can be seen from the Hillas plot, plausible acceleration sites may be the radio lobes or hot spots of powerful active galaxies.

The search for UHECR sources must take into account another effect, the Greisen-Zatsepin-Kuzmin cutoff (GZK) [26, 27], which imposes a theoretical upper limit on the energy of cosmic rays from distant sources. Above a threshold of few 10^{19} eV, protons interact with the 2.7^o K cosmic microwave background radiation (CMB) and lose energy. Due to the GZK cutoff, protons above that threshold cannot travel distances further than few tens of Mpc.

From the astrophysical point of view, this cut-off is very important because it limits the existence of standard astrophysical UHECR emitters inside our local super-cluster of galaxies. The GZK cut-off has stimulated important debate, since there were two contradictory measurements in the region between $10^{19} \div 10^{20}$ eV.

The AGASA experiment in Japan [28] (which used extensive air shower detectors and was decommissioned in early 2004) reported high energy events ($> 2 \times 10^{20}$ eV) claiming a continuity in the CR spectrum violating the GZK cutoff. Different is the observations of the High Resolution Fly's Eye (HiRes) in Utah [29], whose data seem to be consistent with a boundary in the CR spectrum. HiRes uses an experimental technique which is completely different from the one of AGASA, the detection of light fluorescence emission by the extensive air showers induced in the atmosphere by UHECR.
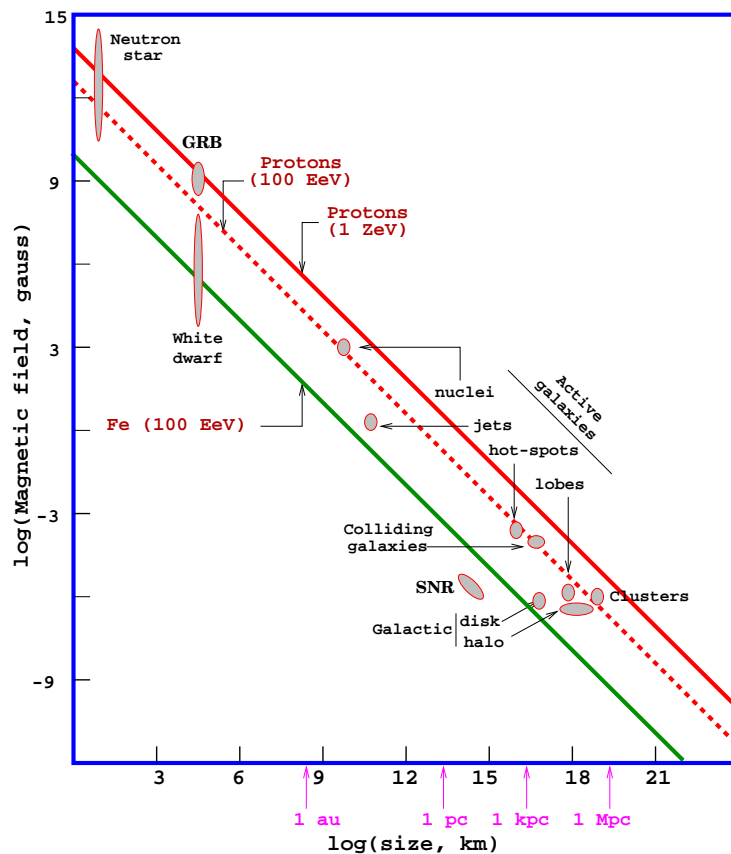
Figure 2: *The Hillas diagram (drawn by Murat Boratav). Acceleration of cosmic rays up to a given energy requires conditions above the respective line. Some sources candidates are still controversial (1 EeV=$10^{18}eV$, 1 ZeV=$10^{21}eV$).*

Nowadays, the largest experiment is the Auger Observatory [31], which combines the measurement of extensive air showers and light fluorescence detection. The Auger Observatory is located in the southern hemisphere in Mendoza, Argentina, and was completed in 2008 with almost 1600 water Cherenkov tanks covering 3000 km^2 and four fluorescence telescopes. One of the major goals of the Auger observatory was to solve the AGASA and HiRes debate, employing the experimental techniques used by both experiments. Auger has recently published [32] the result of the first data set, rejecting the hypothesis that the cosmic ray spectrum continues in the form of a power-law above $10^{19.6}$ eV with 6 sigma significance. The comparison among data from the three experiments can be seen in Fig. 3. In addition, Auger reported the first hints of association of CRs with $E > 6 \times 10^{19}$ eV and nearby (less than 100 Mpc) concentration of matter and AGN [33]. Although its statistical significance is still limited, the results suggest that regions of matter with AGN can be the source candidates for UHECR acceleration.
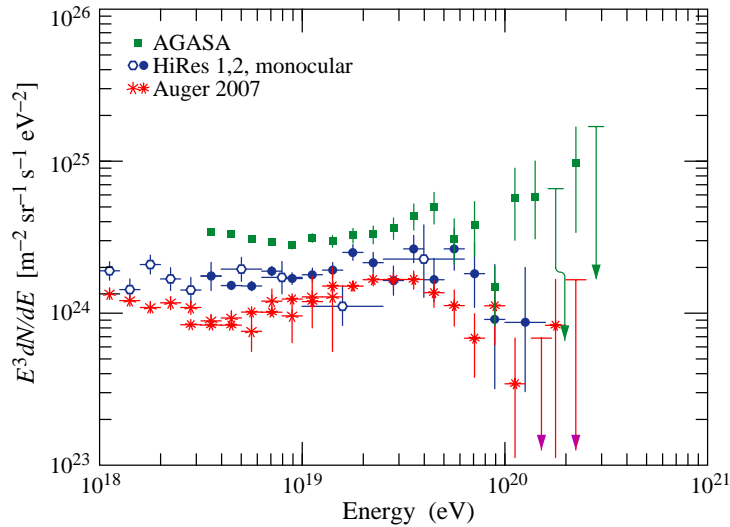
Figure 3: *Expanded view of the highest energy portion of the cosmic-ray spectrum from the three experiment AGASA, HiRes1,2, monocular and Auger. From [30].*

2.2   High energy photons and neutrinos

Due to the influence of galactic magnetic fields, detected charged particles do not point to the sources. Only UHECR can be marginally influenced by magnetic fields, but the GZK cut-off limits the field of view to less than 100 Mpc. Neutral particles (gamma-rays and neutrinos) do not suffer the effect of magnetic fields: they represent the decay products of accelerated charged particles but cannot be directly accelerated.

Both electrons and protons can be accelerated by astrophysical objects. We refer respectively to a *leptonic model* when electrons are accelerated, and to a *hadronic model* when protons or other nuclei are accelerated. When synchrotron radiation is observed from a source, most plausibly electrons are accelerated. On the other hand, we know that protons are accelerated because they are detected as CR. Both models, the leptonic model and the hadronic model should coexist in the universe [34].

In the following, we will focus on the hadronic acceleration [35], because just in this case neutrinos are emitted. High energy photons can be produced both in leptonic and in hadronic models.

2.2.1   TeV γ-rays from leptonic processes

The most important process which produces high energy γ-rays in the leptonic model is the Inverse Compton (IC) scattering [36, 37]. IC γ-rays are produced in the interactions of energetic electrons with ambient background photon fields: the CMB, and the diffuse Galactic radiation of star light. This process is very efficient in producing γ-rays since low energy photons are found in all astrophysical objects. Multi-TeV electrons producing γ-rays of TeV energies via IC, produce synchrotron radiation in the X-ray band as well [38]. Therefore, measurements of the synchrotron X-ray flux from a source is a signal that the accompanying γ-rays are likely produced by leptonic processes.

2.2.2 TeV γ-rays and neutrinos from hadronic processes

The main scenario for the astrophysical production of high energy neutrinos is via the decay of charged pions in the beam dump of energetic protons in dense matter or photons field.
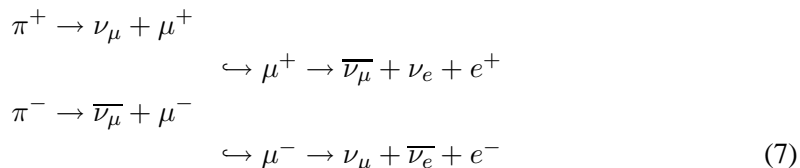
Accelerated protons will interact in the surroundings of the CRs emitter with photons predominantly via the Δ^+ resonance:

$$p + \gamma \to \Delta^+ \to \pi^o + p$$
$$p + \gamma \to \Delta^+ \to \pi^+ + n \tag{5}$$

Protons will also interact with ambient matter (protons, neutrons and nuclei), giving rise to the production of charged and neutral mesons. The relationship between sources of VHE γ-ray ($E_\gamma > 100$ MeV) and neutrinos is the meson-decay channel. Neutral mesons decay in photons:

$$\pi^o \to \gamma\gamma \tag{6}$$

while charged mesons decay in neutrinos:

$$\pi^+ \to \nu_\mu + \mu^+$$
$$\hookrightarrow \mu^+ \to \overline{\nu_\mu} + \nu_e + e^+$$
$$\pi^- \to \overline{\nu_\mu} + \mu^-$$
$$\hookrightarrow \mu^- \to \nu_\mu + \overline{\nu_e} + e^- \tag{7}$$

Therefore, in the framework of the hadronic model and in the case of *transparent sources*, the energy escaping from the source is distributed between CRs, γ-rays and neutrinos. A transparent source is defined as a source of a much larger size that the proton mean free path, but smaller than the meson decay length. For these sources, protons have large probability of interacting once, and a large fraction of secondary mesons decay.

Because the mechanisms that produce cosmic rays can produce also neutrinos and high-energy photons (from eqs. 6,7), candidates for neutrino sources are in general also γ-ray sources. There is a strong relationship between the spectral index of the CR energy spectrum $E^{-\alpha_{CR}}$, an that of γ-rays and neutrinos. It is expected [39] that near the sources, parent proton spectrum index α_{CR} (defined in eq. 3) is almost identical to that of secondary: $\alpha_{CR} \sim \alpha_\nu \sim \alpha_\gamma$. Hence γ-rays from hadronic models have crucial information about primary CRs, and put constraints (see §6) to the expected neutrino flux from sources where γ-rays are observed.

3 Gamma rays astronomy

Different processes occurring in the Universe would result in γ-ray emission, including CR interactions with interstellar gas, supernova explosions, and interactions of energetic electrons with magnetic fields (we do not consider here rapidly transient phenomena as gamma ray bursts). Having no electric charge, γ-rays are not affected by magnetic fields, and can act as messengers of relatively distant cosmic events, allowing straight extrapolation to the source. The first satellite designed as a dedicated gamma-ray mission was the second Small Astronomy Satellite (SAS-2) in 1972. In 1975, the European Space Agency launched a similar satellite, COS-B, which operated until 1982. Photons in the MeV-GeV energy range

were detected by the Energetic Gamma-ray Experiment Telescope (EGRET) [40] on board of the CGRO satellite in the 1990s. The last EGRET catalogue contains 271 detections with high significance, from which 170 are not identified yet.

Following its launch in June 2008 [42], the Fermi Gamma-ray Space Telescope (Fermi) began a sky survey in August. The Large Area Telescope (LAT) on Fermi produced, in 3 months, a deeper and better-resolved map of the γ-ray sky than any previous space mission. The initial result for energies above 100 MeV [43] regards the 205 most significant (statistical significance greater than 10σ) γ-ray sources, which are the best-characterized and best-localized ones. Fig. 4 shows the locations of the 205 bright sources, in Galactic coordinates. All associations with specific source classes are also shown.
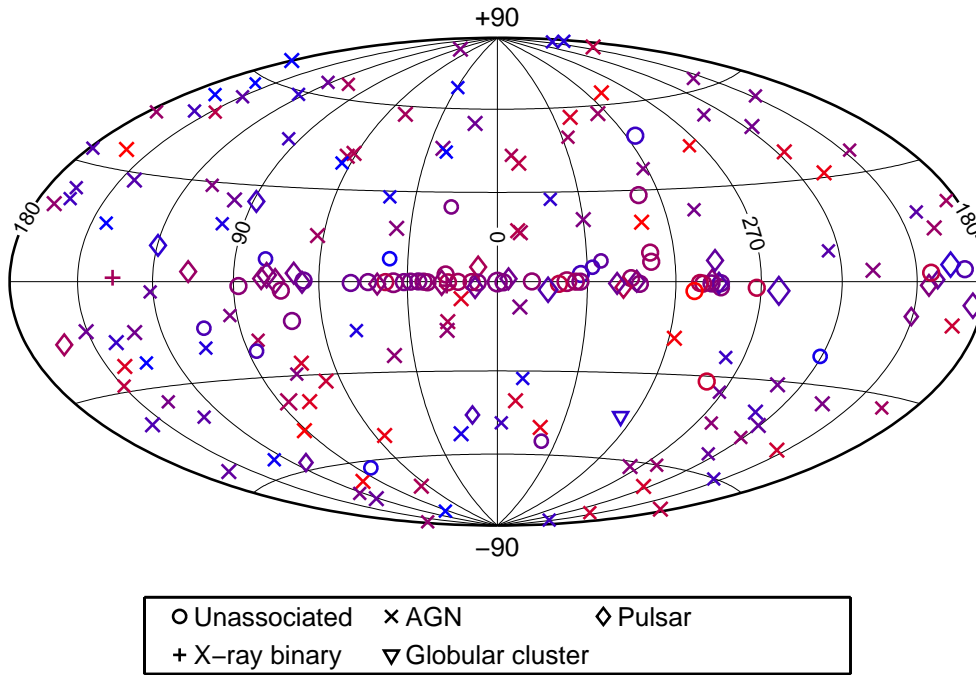

Figure 4: *The Fermi LAT Bright Source List, showing the locations on the sky (Galactic coordinates in Aitoff projection) coded according to the legend. Symbols in blue indicate sources with harder spectra than those in red [43].*

Due to the absorption of the atmosphere, γ-rays above 100 GeV are only detectable in ground based apparatus, using a technique known as Imaging Air-Cherenkov Technique (IACT). These γ-rays are of particular interest, because neutral pion decay (eq. 6) produces photons within this energy range. High-energy gamma rays are absorbed when reaching the Earth atmosphere, and the absorption process proceeds by creation of a cascade or shower of high-energy relativistic secondary particles. These emit Cherenkov radiation, at a characteristic angle in the visible and UV range, which passes through the atmosphere. As a result of Cherenkov light collection by a suitable mirror in a camera, the showers can be observed on the surface of the Earth.

The pioneering ground based γ-ray experiment was built by the Whipple collaboration [44]. During the last decade, several ground based γ-ray detectors were developed.

The HEGRA experiment [45] has pioneered stereoscopic shower imaging by arrays of Cherenkov telescopes. Other detectors are the VERITAS array [46] and the upgrade of the existing CANGAROO array [47]. At present, the two new generation telescopes are the HESS telescope array [48] and the MAGIC telescope [49]. A full and detailed review of VHE astrophysics with the ground-based γ-ray detectors is in [36, 37].

The HESS instrument is an array of 4 telescopes, each one with twelve-meter diameter light collectors. Each instrument combines the stereoscopic imaging with large light collectors and highly segmented detectors with a wide field of view. The HESS telescope has been operational since 2004. The MAGIC telescope is a giant seventeen-meter telescope which provides large photon collection. It uses photon detectors with enhanced quantum efficiency, and image timing information. One of the particular features of this telescope is the fast positioning to a source when alerted by γ-ray burst trigger from satellite detectors. MAGIC started taking data in 2004. A second telescope will be operational from May 2009. These IACTs telescopes produced a catalogue of γ-ray sources emitting at energies above TeV. The sky map can be seen in Fig. 5. Of particular interest is the great population of new γ-ray sources in the Galactic Centre region discovered by the HESS telescope. A list of more than 70 galactic and extra-galactic sources are in [36].
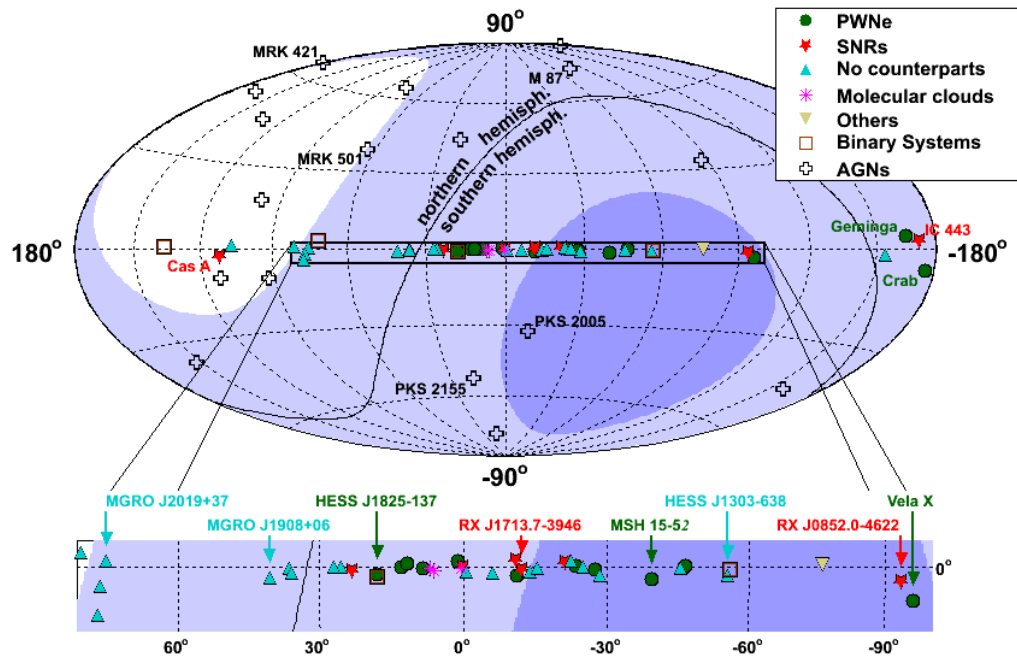

Figure 5: *Sky map of high energy γ-ray sources above 100 GeV. The shading indicates the visibility for a detector in the Mediterranean sea with 2π downward coverage; dark (light) areas are visible at least 75% (25%) of the time (from [8]).*

Gamma astronomy suffers also some limitations. Fig. 6 shows the mean free path travelled by photons as a function of their energy. Photons above 10 GeV are attenuated by

interactions with infrared (IR) and radio photons of the extragalactic background light and with the Cosmic Microwave Background (CMB). In particular, above 10 TeV the horizon of the photons is limited to less than 10 Mpc, much less that the horizon of UHECR. Only neutrinos can open the windows of the extreme regions of the Universe, as we will see in §6.
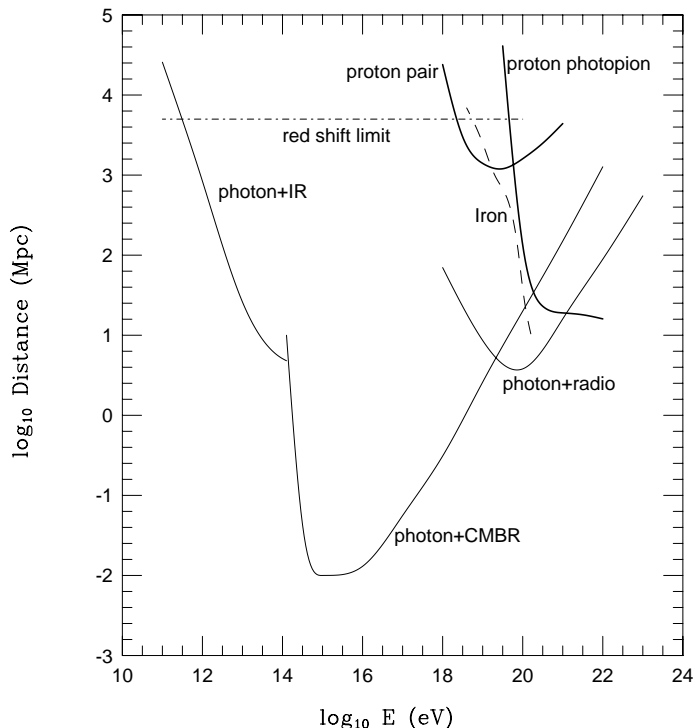

Figure 6: *Absorption length in Megaparsec as a function of photon or proton energy.*

3.1   The standard candle: the CRAB nebula pulsar

The Crab pulsar, with a rotational period of 33 ms and a spin-down luminosity $L = 5 \times 10^{38}$ erg/second, is a particular important source for high energy astrophysics. In fact, the pulsar powers a surrounding synchrotron nebula which has been detected in radio and X-ray wavelengths [51]. It is believed that the rotational energy of the pulsar is mostly carried away by a relativistic wind of electrons and positrons. The interaction of this wind with the surrounding medium creates a relativistic shock wave, where the leptons are thought to be accelerated to high energies [52]. The interaction of accelerated leptons with ambient infra-red photon fields can produce γ-rays via the Inverse Compton process.

   The Crab nebula was discovered at TeV energies in 1989 [53] and it is conventionally used as a standard reference source of TeV γ-rays, due to its relative stability and high flux. It is convenient to use the Crab flux as *reference flux* for TeV γ-ray astronomy. In fact, if VHE γ-rays are produced by hadronic processes, a similar neutrino flux is expected. A reference flux equal to 1 C.U. (Crab Unit) is defined as the flux similar to that of the Crab,

assuming no energy cutoff and a spectral index $\Gamma = 2$:

$$E_\gamma^2 \frac{d\Phi_\gamma}{dE_\gamma} = 10^{-11} \, TeV \, cm^{-2} s^{-1} = 1 \, C.U. \tag{8}$$

The Crab VHE γ-rays spectrum measured by different experiments shows a steepening; a better fit of the data is provided by a power law (energy E in TeV) with an exponential cutoff: $\frac{d\Phi_\gamma}{dE_\gamma} = I_0 E^{-\Gamma} e^{(-E/E_c)}$. This formula, with $\Gamma = 2.39 \pm 0.03_{stat}$ and a cutoff energy $E_c = (14.3 \pm 2.1_{stat})$ TeV, gives a differential flux normalisation at 1 TeV of $I_0 = (3.76 \pm 0.07_{stat}) \times 10^{-11}$ cm^{-2}s^{-1}TeV^{-1} [54].

Regarding neutrino telescopes, the Crab is in a particular sky position (see Fig. 5), because it can be seen for both telescopes located in the Northern or Southern Earth hemisphere. In case of hadronic process involved in the Crab (assuming $E_\nu^2 \frac{d\Phi_\nu}{dE_\nu} \simeq E_\gamma^2 \frac{d\Phi_\gamma}{dE_\gamma}$), the predicted event rate in a neutrino telescope as big as the IceCube experiment is $N(E_\mu > 1$ TeV$) \sim 2.8$ yr^{-1} [55]. Negative or positive detection of neutrinos from the Crab direction will confirm or disprove the proposed leptonic processes.

4 Neutrino detection principle

The basic idea for a neutrino telescope is to build a matrix of light detectors inside a transparent medium. This medium, such as deep ice or water:

- offers large volume of free target for neutrino interactions;

- provide shielding against secondary particles produced by CRs;

- allows transmission of Cherenkov photons emitted by relativistic particles produced by neutrino interaction.

Other possibilities, such as detecting acoustic or radio signals generated by EeV (10^{18} eV) neutrinos in a huge volume of water or ice are not considered in this review.

In general, high energy neutrino interact with a nucleon N of the nucleus, via either charged current (CC) weak interactions

$$\nu_l + N \to l + X \tag{9}$$

or neutral current (NC) weak interactions

$$\nu_l + N \to \nu_l + X \ . \tag{10}$$

The remnants X form a hadronic shower. Relativistic charged particles emit Cherenkov radiation in the transparent medium. A detector can measure the intensity and arrival time of these photons on a three-dimensional array of Photo Multiplier Tubes (PMTs). From these measurements, some of the properties of the neutrino (flavour, direction, energy) can be inferred. The experimental signature (Fig. 7) depends on the type of reaction and on the neutrino flavour. In the case of CC ν_μ interactions, the long range of the muon (§4.2) increases the effective volume of the detector, since neutrinos can be detected even when the interaction occurs several kilometres outside the instrumented volume.

Electron resulting from a charged current ν_e interaction will produce an electromagnetic shower whose size is of the order of a few meters. For ν_τ interactions, the produced τ-lepton travels some distance (depending on its energy) before it decays and produces a second shower. The Cherenkov light emitted by the charged particles in the showers can be detected if both the ν_τ interaction and the τ decay occur inside the instrumented volume of the detector.
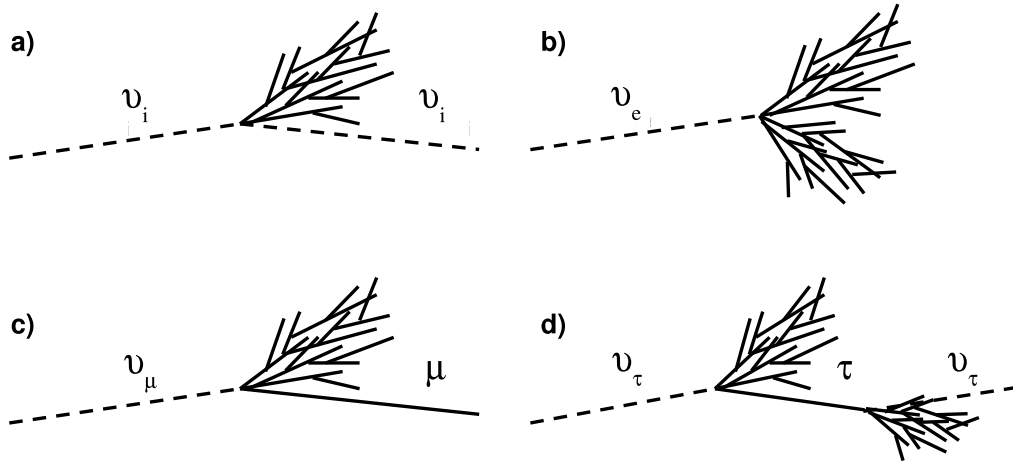

Figure 7: *Event signature topologies for different neutrino flavours and interactions: a) NC interaction producing a hadronic shower; b) CC interaction of ν_e producing both an EM and a hadronic shower; c) CC interaction of ν_μ producing a muon and a hadronic shower; d) CC interaction of ν_τ producing a τ that decays into a ν_τ tracing the double bang event signature. Particles and anti-particles cannot be distinguish in neutrino telescopes. From [56]*

We will mainly focus on muon neutrinos, which are especially interesting in a search for point sources of energies larger than ~ 1 TeV. In this energy range, ν_μ interaction can occur outside the detector volume, while in most cases muons are energetic enough to completely traverse the detector. This gives a clean experimental signal which allows accurate reconstruction of muon direction, closely correlated with neutrino direction (§4.1).

Neutrino telescopes are not background free. Air showers induced by interactions of cosmic rays with the Earth's atmosphere produce the so-called *atmospheric muons* and *atmospheric neutrinos*. In fact, atmospheric muons can penetrate the atmosphere and up to several kilometers of sea water (§4.2). Neutrino detectors must be located deeply under a large amount of shielding in order to reduce the background. The flux of down-going atmospheric muons exceeds the flux induced by atmospheric neutrino interactions by many orders of magnitude, decreasing with increasing detector depth, as is shown in Fig. 8.

Neutrino telescopes, at the contrary of usual optical telescopes, are 'looking downward'. Up-going muons can only be produced by interactions of (up-going) neutrinos. From the bottom hemisphere, the neutrino signal is almost background-free (Fig. 9). Only atmospheric neutrinos that have traversed the Earth, represent the irreducible background for the study of cosmic neutrinos. The rejection of this background depends upon the pointing
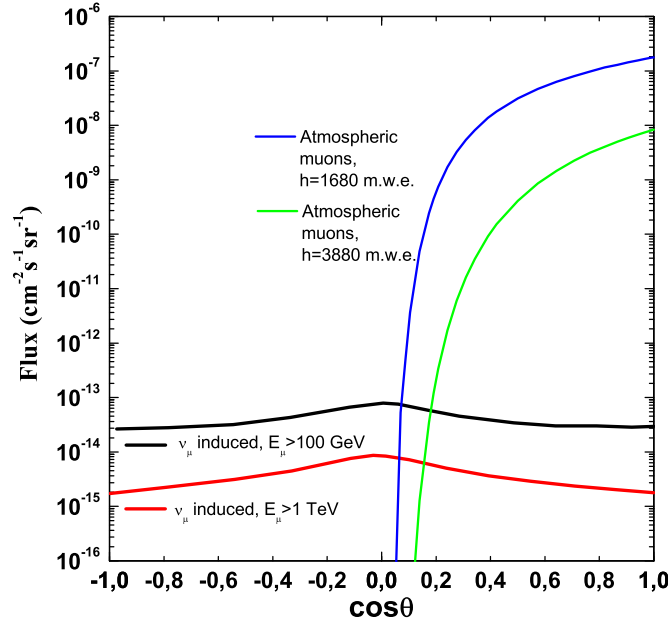
Figure 8: *Different contributions (as a function of the cosines of the zenith angle) of the: i) atmospheric muons (computed according to [57]) for two different depths; ii) atmospheric neutrino induced muons (from [58]), for two different muon energy thresholds.*

capability of the telescope and its possibility to estimate the parent neutrino energy.

The previous generation of experiments looking also for astrophysical neutrinos (MACRO [59], SuperKamiokande [60]) was located under mountains, and reached almost the maximum possible size for underground detectors.

As we will discuss in §7, either water or ice is used as media. A deep sea-water telescope has some advantages over ice and lake-water experiments due to the better optical properties of the medium. However, serious technological challenges must be overcome to deploy and operate a detector in deep sea, as we will discuss in §9.

Detection of astrophysical neutrino by any of these experiments has not been claimed so far.

4.1 Neutrino cross section

For high energy neutrinos, interactions are deeply inelastic. At energies of interest for neutrino astronomy, the leading order differential cross section for the $\nu_l N \to lX$ Charged Current (CC) interactions is given by [67]

$$\frac{d^2\sigma_{\nu N}}{dxdy} = \frac{2G_F^2 m_N E_\nu}{\pi} \frac{M_W^4}{(Q^2 + M_W^2)^2}[xq(x,Q^2) + x(1-y)^2\overline{q}(x,Q^2)] \qquad (11)$$

where $x = Q^2/2m_N(E_\nu - E_l)$ and $y = (E_\nu - E_l)/E_\nu$ are the so-called scale variables or Feyman-Bjorken variables, Q^2 is the square of the momentum transferred between the
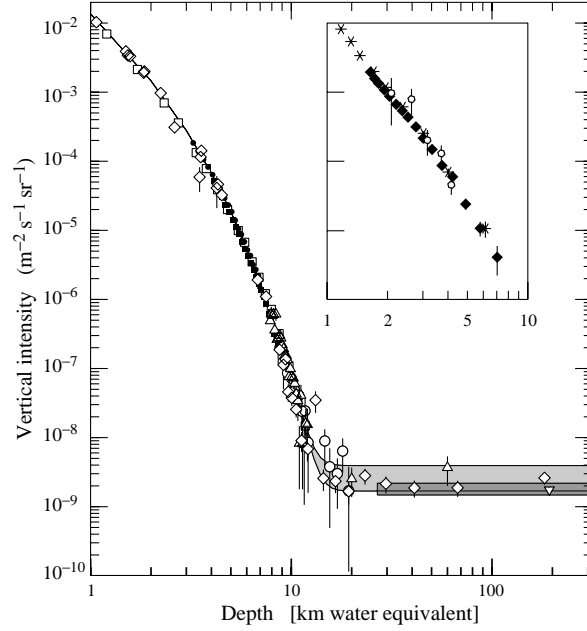
Figure 9: *Vertical muon intensity vs. depth (1 km.w.e.= 10^5 gcm^{-2} of standard rock). Fig. from [30]. The experimental data are from: the compilations of Crouch ◇ [61], Baksan [62], LVD ◦ [63], MACRO ● [64], Frejus [65], and SNO △ [66]. The shaded area at large depths represents neutrino-induced muons of energy above 2 GeV. The upper line is for horizontal neutrino-induced muons, the lower one for vertically upward muons.*

neutrino and the lepton, m_N is the nucleon mass, M_W is the mass of the W boson, and G_F is the Fermi coupling constant. The functions $q(x, Q^2)$ and $\overline{q}(x, Q^2)$ are the parton distributions for quarks and antiquarks. The Bjorken variable x is a measure of the inelasticity of the interaction. Therefore, high energy deep inelastic neutrino interactions are characterized by $x \ll 1$. Fig. 10 shows the ν_μ and $\overline{\nu}_\mu$ cross sections as a function of the neutrino energy. As can be seen, at low energies the neutrino cross section rises linearly with E_ν up to $\sim 10^4$ GeV. For higher energies, the invariant mass $Q^2 = 2m_N E_\nu xy$ could be larger than the W-boson rest mass, reducing the increase of the total cross section. Since there is not data constrain the structure functions at very small x, some uncertainties are estimated on the total cross section at large energies [68].

The relation between neutrino and muon directions is essential for the concept of a neutrino telescope. Since neutrinos are not deflected by (extra-) galactic magnetic fields, it is possible to trace the muon back to the source of the neutrino. This is equivalent to optical astronomy where photons point back to their source. The angle $\theta_{\nu\mu}$ between the incident neutrino and the outgoing muon can be approximated by:

$$\overline{\theta_{\nu\mu}} \leq \frac{1.5^o}{\sqrt{E_\nu(TeV)}} \tag{12}$$

where E_ν is the neutrino energy. A muon travelling through rock or water is subject to multiple scattering. The deviation of the muon direction due to this process after travelling
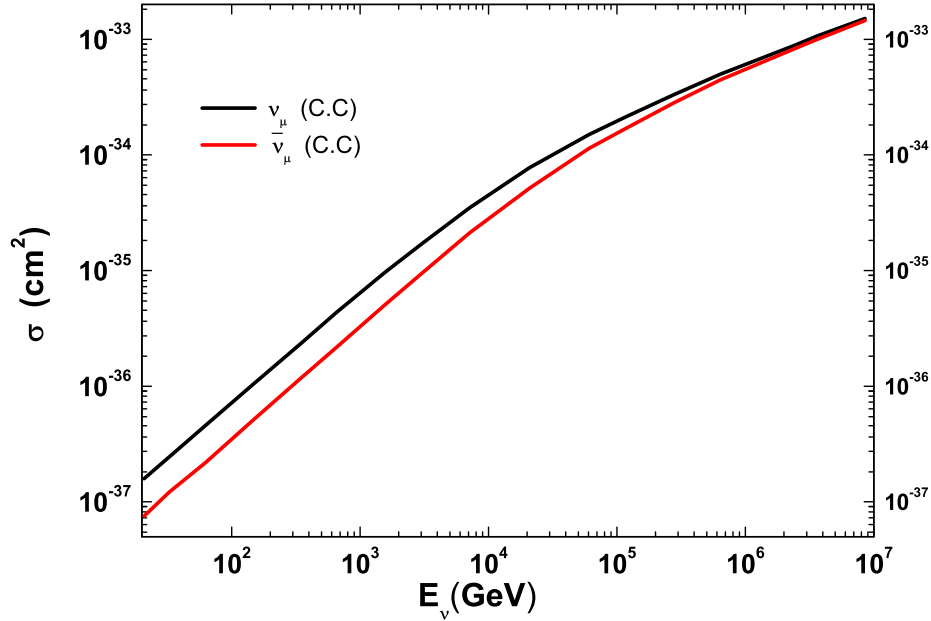
Figure 10: *Cross section for ν_μ and $\overline{\nu}_\mu$ as a function of the (anti)-neutrino energy according to CTEQ6-DIS [68] parton distributions.*

a distance x is given by [30] :

$$\theta_{ms} = \frac{13.6(MeV)}{E_\mu}\sqrt{x/X_0}[1 + 0.0038 ln(x/X_0)] \tag{13}$$

where X_0 is the radiation length of the medium, which is 37 cm for water. At energies and distances that concern us, θ_{ms} is smaller than $\theta_{\nu\mu}$ and the smearing effect can be neglected. Muon direction can be measured with precision of the order of less than 1° in ice, and with $\sim 0.2^o$ in water (see §7).

4.2 Muon energy loss

Muon energy losses are due to several processes such as ionization, pair production, bremsstrahlung and photonuclear interactions. The total energy loss per unit length can be written in a parametrized formula as:

$$dE_\mu/dx = \alpha(E_\mu) + \beta(E_\mu) \cdot E_\mu \tag{14}$$

where $\alpha(E_\mu)$ is an almost constant term that accounts for ionization, and $\beta(E_\mu)$ takes into account the radiative losses. Fig. 11 shows muon energy loss as a function of the energy due to different interactions in water.

Fig. 12 shows the effective muon range $R_{eff}(E_\mu, E_\mu^{min})$ in water as a function of the parent neutrino energy. $R_{eff}(E_\mu, E_\mu^{min})$ represent the range after which the muon has still a residual energy E_μ^{min} at the detector. For instance, at energies larger than 10 TeV, the produced muon travels more than 4 km and arrives with more than 1 TeV of residual energy.
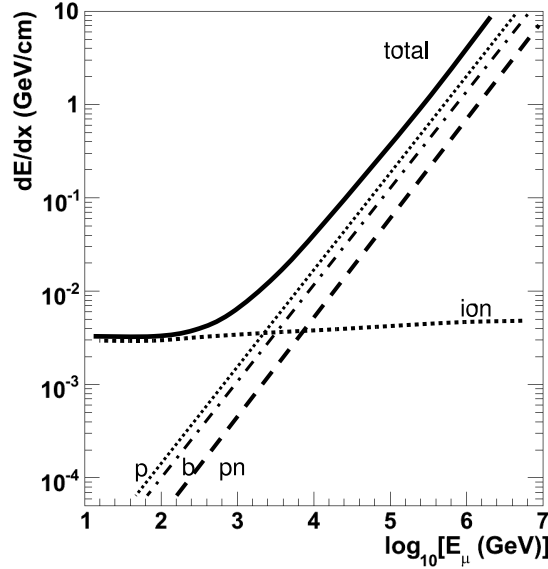
Figure 11: *Energy loss of a muon in water: p, pair production; b, bremsstrahlung; pn, photo-nuclear interactions; ion, ionization.*

The event will be detected even if the neutrino interaction vertex is outside the instrumented detector volume of the telescope.

4.3 Cherenkov radiation

Any operating or proposed neutrino telescope in the TeV-PeV range is working by collecting the Cherenkov light on a three-dimensional array of photomultiplier tubes (PMTs). The information provided by the number of photons detected and their arrival times are used to infer the neutrino track direction and energy.

Cherenkov radiation is emitted by charged particles crossing an insulator medium with speed exceeding that of light in this medium [70]. The charged particle polarizes the molecules along the particle trajectory, but only when the particle moves faster than the speed of light in that medium, an overall dipole moment is present. Light is emitted when the insulator's electrons restore themselves to equilibrium after the disruption has passed, creating a coherent radiation emitted in a cone with a characteristic angle θ_C given by

$$cos\theta_C = \frac{c/n}{\beta c} = \frac{1}{\beta n} \tag{15}$$

where n is the refracting index of the medium and β is the particle speed in units of c. For relativistic particles ($\beta \simeq 1$) in sea water ($n \simeq 1.364$) the Cherenkov angle is $\theta_C \simeq 43^o$.

The number of Cherenkov photons, N_γ, emitted per unit wavelength interval, $d\lambda$ and unit distance travelled, dx, by a charged particle of charge e is given by

$$\frac{d^2N}{dxd\lambda} = \frac{2\pi}{137\lambda^2}(1 - \frac{1}{n^2\beta^2}) \tag{16}$$
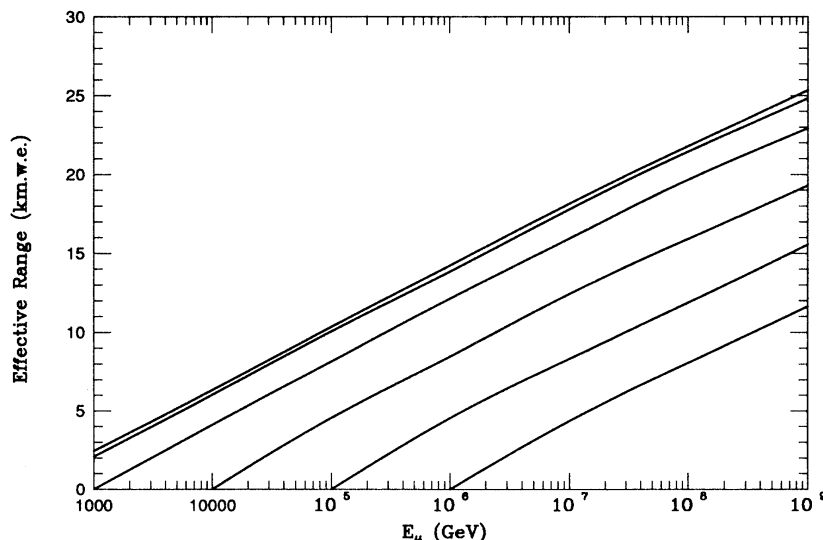
Figure 12: *Effective muon range as a function of the initial energy E_o. Curves correspond (from top to bottom) to different threshold energies E_{thr} of the muon arriving at the detector. $E_{thr} = 1, 10^2, 10^3, 10^4, 10^5, 10^6$ GeV. From [69].*

where λ is the wavelength of the light radiation. From this formula it can be seen that shorter wavelengths contribute more significantly to the Cherenkov radiation. The light absorption by water/ice will strongly suppress some wavelengths, see §7. Typically, in the wavelength range between 300-600 nm of the photomultiplier tubes (PMT), the number of Cherenkov photons emitted per meter is about 3.5×10^4.

Fig. 13 shows one example of optical module used by present neutrino telescopes in ice and water (see §9 and §10). The PMT quantum efficiency is large in the wavelength range between 300-500 nm, matching very well the region in which ice/water are transparent to light.

5   Why a km^3 telescope

In this section we develop a *toy model* for a neutrino telescope. Our aim is to derive, using an analytic calculation, why a cubic kilometre scale detector is needed, and what is the number of optical sensors required to detect neutrinos in the instrumented volume. In sec. 6 we present some theoretical models of galactic and extragalactic neutrino sources. For each model, the source is characterized by the differential neutrino energy spectrum $\frac{d\Phi_\nu}{dE_\nu}$ (TeV^{-1} cm^{-2}s^{-1}) at Earth. The number of *detectable* events induced by this neutrino flux can be simply derived using the *neutrino effective area*. This quantity (defined in sec. 5.2) is computed by each experiment, and can be used to compare the sensitivity of the different experiments to the same neutrino flux.
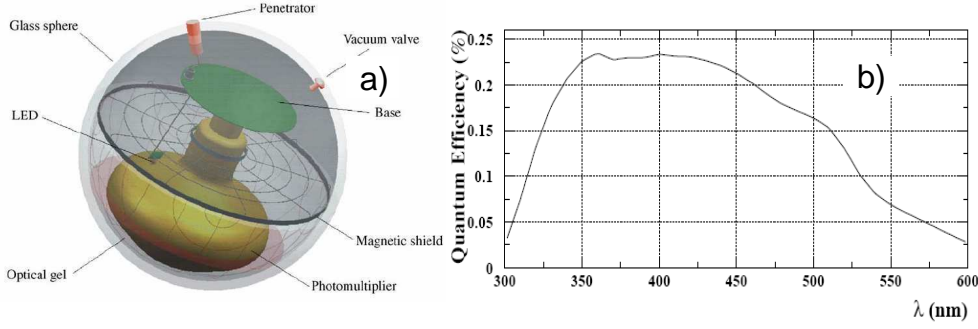
Figure 13: *(a) Sketch of an ANTARES optical module: a large hemispherical (10 inches in diameter) photomultiplier (PMT) is protected by a pressure-resistant glass sphere. The outer diameter of the sphere is 43.2 cm. A mu-metal cage protects the PMT from the Earth magnetic field. An internal LED is used for the calibration. (b) The quantum efficiency for PMTs used by AMANDA, ANTARES and NEMO collaborations (from Hamamatsu).*

5.1 Number of events for a $standard$ neutrino candle

As previously discussed in sec. 4.2, it is possible to enhance the *effective volume* of the detector by looking for muons produced in a larger volume surrounding the detector itself. The effective volume (depending on the neutrino energy) corresponds to the product of the detector effective area and the muon range R_μ.

There is concordance between the estimated α_{CR} of primary CR near the source and the measured spectral index α_γ of TeV gamma-rays from IACT: $\alpha_{CR} \simeq \alpha_\gamma \sim 2$. If the TeV gamma-rays are originated from hadronic processes, an almost equal neutrino flux is expected (sec. 3.1), with $\frac{d\Phi_\nu}{dE_\nu} \simeq \frac{d\Phi_\gamma}{dE_\gamma}$. We will use the Crab reference flux, defined in eq. 8. The event rate in a neutrino telescope can be expressed in terms of:

$$\frac{N_\mu(E_\mu^{min})}{T} = \int dE_\nu \cdot \frac{d\Phi_\nu}{dE_\nu}(E_\nu) \cdot A \cdot P_{\nu\mu}(E_\nu, E_\mu^{min}) \cdot e^{-\sigma(E_\nu)\rho N_A Z(\theta)} \qquad (17)$$

where A and T are the detector area and observation time, respectively. $P_{\nu\mu}$ is the probability that the neutrino gives an observable muon (see below). The *effective neutrino area* is the quantity:

$$A_\nu^{eff}(E_\nu) = P_{\nu\mu}(E_\nu, E_\mu^{min}) \cdot A \cdot e^{-\sigma(E_\nu)\rho N_A Z(\theta)} \qquad (18)$$

The term $e^{-\sigma(E_\nu)\rho N_A Z(\theta)}$, where $\sigma(E_\nu)$ is the total neutrino cross section, N_A the Avogadro number, (ρN_A) the target nucleon density and θ the neutrino direction with respect to the nadir, takes into account the Earth absorption of neutrinos along the Earth path $Z(\theta)$. From the nadir $Z(0) = 6.4 \times 10^8$ cm, the absorption becomes important for $\sigma > 10^{-34}$ cm^2 (or equivalently $E_\nu > 20 \div 50$ TeV, see Fig. 10), when $e^{-\sigma\rho N_A Z} \simeq e^{-0.05} \simeq 0.95$.

Lets consider $P_{\nu\mu}(E_\nu, E_\mu^{min})$. It represents the probability that a neutrino with energy E_ν produces a muon of energy E_μ which survives with energy $> E_\mu^{min}$ after the propaga-

tion from the interaction point to the detector. It can be expressed in terms of:

$$P_{\nu\mu}(E_\nu, E_\mu^{min}) = N_A \int_0^{E_\nu} dE_\mu \frac{d\sigma_\nu}{dE_\mu}(E_\mu, E_\nu) R_{eff}(E_\mu, E_\mu^{min}) \qquad (19)$$

where $d\sigma_\nu/dE_\mu$ is the differential neutrino cross section to produce a muon of energy E_μ, and $R_{eff}(E_\mu, E_\mu^{min})$ is the effective muon range. One can tabulate $P_{\nu\mu}$ for a given muon energy threshold. Fig. 14 shows $P_{\nu\mu}$ for two values of muon threshold energy: 1 GeV (which was the characteristic muon threshold for large area underground detector, like MACRO) and 1 TeV (which is the characteristic value for neutrino telescopes). There is uncertainty in eq. 19 due to the uncertainty in neutrino cross section for energies larger than 10 TeV (§4.1).
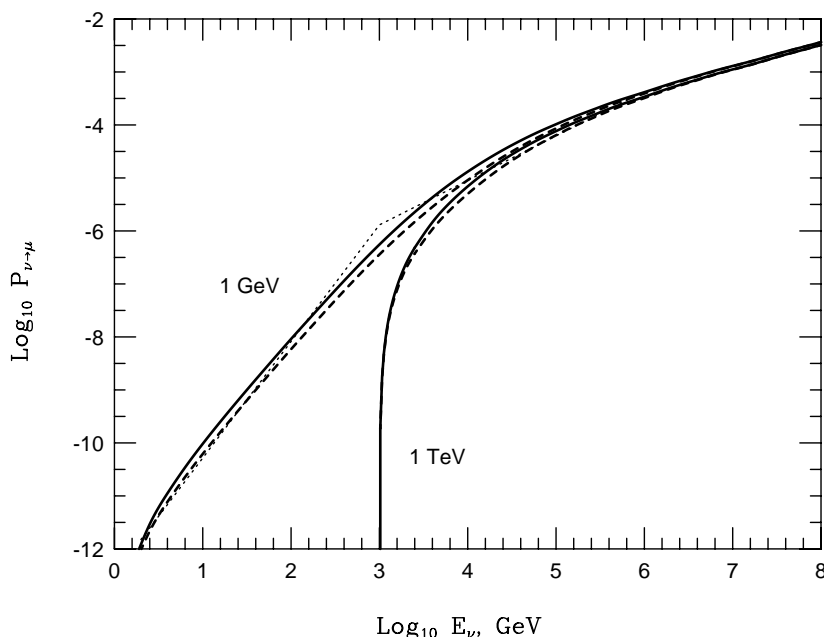

Figure 14: *$P_{\nu\mu}$ [71] for two values of the muon threshold energy: 1 GeV and 1 TeV. The solid line are neutrinos and the dashed line antineutrinos. The dotted lines show a power law approximation.*

It is instructive to note the dependence of $P_{\nu\mu}$ for $E_\mu^{min} > 1$ GeV on neutrino energy [11]: it can be approximated with $P_{\nu\mu} \propto E_\nu^2$ for $E_\nu < 1$ TeV, and $P_{\nu\mu} \propto E_\nu$ for $1 < E_\nu < 10^3$ TeV. The two energy regimes reflect the energy dependence of the neutrino cross section (which depends almost linearly on energy) and effective muon range (which depends linearly on muon energy up to ~ 1 TeV, when muon radiative losses become dominant).

To solve analytically eq. 17 in our simplified model, we can use the approximation for neutrino energies larger than 1 TeV: $P_{\nu\mu}(E_\nu, E_\mu^{min}) \simeq P_o E_\nu^{0.8} = 10^{-6} E_\nu^{0.8}$ (E in TeV) [71]. Using this approximation, the event rate for a source of 1 C.U. (eq. 8) can be

analytically computed in the range between $1 \div 10^3$ TeV, neglecting the Earth's absorption:

$$\frac{N_\mu(E_\mu^{min})}{T} = \int_{1\ TeV}^{10^3\ TeV} dE_\nu \cdot (K E_\nu^{-2}) \cdot A \cdot (P_o E_\nu^{0.8}) = 5 \times 10^{-19} \cdot A\ cm^{-2} s^{-1} \quad (20)$$

where $K = 10^{-11}$ TeV^{-1} cm^{-2} s^{-1}. The area A is the surface surrounding the instrumented volume from which muons of energy E_μ^{min} can be detected. Assuming an area $A \simeq 5$ km^2 (surface of a sphere with 1 km^3 volume), the number of expected events in this calculation is ~ 1/year, in a rough agreement with the more detailed computation of [55].

5.2   The neutrino effective area

For a more detailed computation of the rate of detectable events for a reference neutrino flux, experiments express their sensitivity in terms of the effective area, computed using Monte Carlo (MC) techniques [72]. A flux of neutrino is generated, which interacts in a huge volume V_{gen} of material surrounding the instrumented volume. The MC-evaluated effective neutrino area is computed as:

$$A_\nu^{eff} = \frac{N_x}{N_{gen}} \times V_{gen} \times (\rho N_A) \times \sigma(E_\nu) \times e^{-\sigma(E_\nu)\rho N_A Z(\theta)} \quad (21)$$

where N_x is the number of detected (triggered, reconstructed) events and N_{gen} is the number of generated events. The other quantities have been already defined. Fig. 15 shows the effective neutrino area for IceCube, ANTARES and for two reference detectors in the Km3Net design report for the cubic kilometre detector in the Mediterranean sea [50]. The effective area represents a useful tool to compare different experiments, because for a given source it is straightforward to compute the number of expected events as:

$$\frac{N_\mu}{T} = \int dE \cdot \frac{d\Phi_\nu}{dE_\nu} \cdot A_\nu^{eff}(E_\nu) \quad (22)$$

In eq. 21, N_x depends on neutrino energy and direction. This has two consequences:
i) sources with a similar fluency (number of neutrino per unit of area and unit of time) but different spectral index α produce a different response to neutrino telescopes (harder is the α, better the source is seen);
ii) due to the Earth motion, the position in the detector frame of a given source in the sky changes with daytime. The effective area must be computed for each declination, by averaging over the local coordinates (zenith and azimuth angle).

5.3   Number of optical sensors

The natural effective volume for a neutrino telescope is of the order of a km^3. How many optical sensor (PMTs) are needed? This is the major impact factor on the cost of an experiment.

Lets assume using a PMT with a 10" diameter, detection area $A_{pmt} \sim 0.05\ m^2$ and quantum efficiency $\epsilon_{pmt} \simeq 0.25$ (see Fig. 13). Similar PMTs, which have the advantage to fit inside commercial pressure-resistant glass spheres, have been chosen by the IceCube, ANTARES, NEMO and NESTOR collaborations. As we will discuss in §7.2, ice or sea water absorption length λ_{abs} for light in the 400-500 nm range is larger than 50 m. A photon
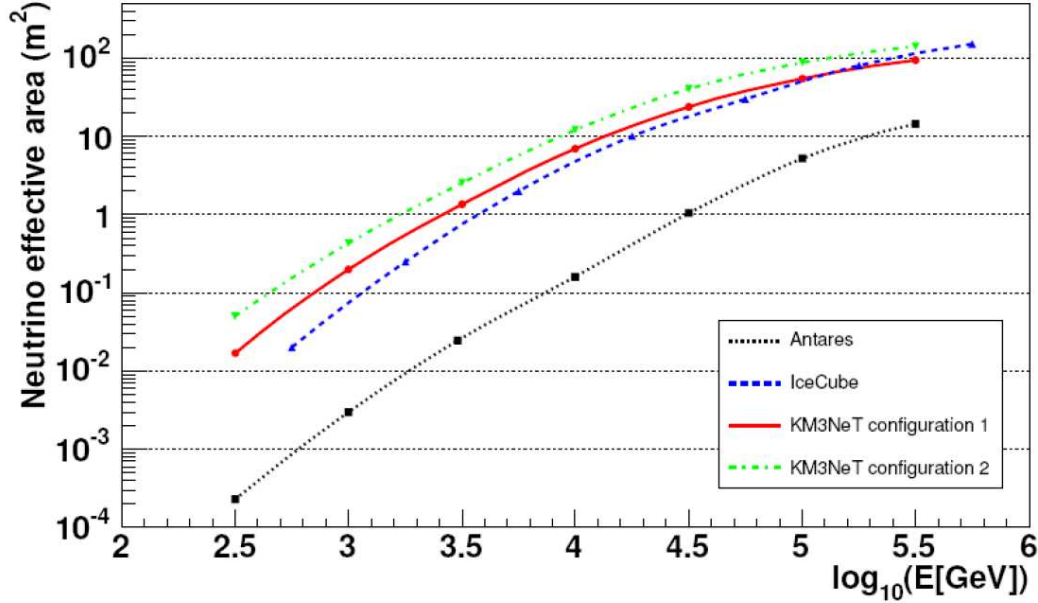
Figure 15: *Neutrino effective area as a function of the true simulated neutrino energy. Two different version of a km^3 (§11) detector in the Mediterranean sea are compared to the IceCube (§9.1) detector in the Antarctic South Pole. The ANTARES (§10.1) neutrino area is shown for comparison.*

falling inside the effective PMT volume $V_{pmt} = A_{pmt} \times \lambda_{abs} \simeq 2.5 \ m^3$ is converted into a photoelectron (p.e.) with a probability (equal to the PMT quantum efficiency) $\epsilon_{pmt} \simeq 0.25$.

Let us call N_{pmt} the number of optical sensors inside the instrumented volume (number to be determined). The rate R between the effective PMT volume of N_{pmt} and the total volume is:

$$R = \frac{V_{pmt} \times N_{pmt}}{10^9 \ m^3} = 2.5 \times 10^{-9} N_{pmt} \tag{23}$$

The total number of Cherenkov photons emitted by a 1 km length muon track in the wavelength range of PMTs sensitivity (sec. 4.3) is $N_\gamma \simeq 3.5 \times 10^7$. The fraction of these photons converted into photoelectrons giving a signal is:

$$N_{p.e.} = N_\gamma \times R \times \epsilon_{pmt} \simeq (3.5 \times 10^7) \cdot (2.5 \times 10^{-9} N_{pmt}) \cdot \epsilon_{pmt} = 2 \times 10^{-2} N_{pmt} \tag{24}$$

The number of different fired PMTs needed to reconstruct a muon track is of the order of a few tens. Taking into account that in most cases more than one single photoelectron is produced by optical photons arriving on the same PMT in the integration window of the electronics (which is of the order of 20-50 ns), a reasonable value of $N_{p.e.}$ is ~ 100. The minimum number of optical sensors follow straightforward from eq. 24:

$$N_{pmt} = 100(p.e.)/2 \times 10^{-2} = 5000 \tag{25}$$

6 Astrophysical sources of HE neutrinos

In this section, we will review the candidate sources of high energy neutrinos. Many of these sources seem to be *guaranteed*, since complementary observations of TeV γ-rays can hardly be explained by leptonic models alone. The expected neutrino fluxes at Earth, however, are uncertainty and predictions differ in some cases up to orders of magnitude.

Finally, the effect of flavour oscillation on neutrinos of cosmic origin is discussed.

6.1 Galactic neutrinos

Some galactic accelerators must exist to explain the presence of CRs with energies up to the $ankle$. These sources can be potentially interesting for a neutrino telescope. Apart from details, it is expected that galactic sources are related to the final stage of the evolution of massive, bright and relatively short-lived stellar progenitors. Some of the most promising candidate sources of neutrinos in our Galaxy are extremely interesting due to the recent results from γ-ray telescopes. A neutrino telescope in the Northern hemisphere (as a detector in the Mediterranean sea) is looking at the same Southern field-of-view as the HESS and CANGAROO Imaging Air Cherenkov telescopes, while the neutrino telescope in the South Pole is looking at the Northern sky.

6.1.1 Shell-type supernova remnants

After a supernova (SN) explosion, particles can be accelerated in the so-called supernova remnants (SNR) in the shock-waves of the expanding shells via Fermi mechanism (§2.1.1). If the final product of the SN is a neutron star, already accelerated particles can gain additional energy due to its strong magnetic fields. Shell-type SNRs are considered to be the most likely sites of galactic CR acceleration, supported by recent observations from the γ-ray IACT.

Of particular interest is the supernova remnant in the Vela Jr. (RX J0852.0-4622). This SNR is one of the brightest objects in the southern TeV sky. Recent observations of γ-rays exceeding 10 TeV in the spectrum of this SNR by HESS [73] have strengthen the hypothesis that the hadronic acceleration is the process that is needed to explain the hard and intense TeV γ-ray spectrum. HESS observed that the γ-ray TeV emission originates from several separated regions in a large apparent size of $\sim 2^o$. As we discuss in §9, angular resolution of underwater neutrino telescopes is much better than 2°. From some calculations [55], the expected neutrino-induced muon rate leads to encouraging results for a detector in the Mediterranean sea.

A second important source is the SNR RX J1713.7-3946, which has been the subject of large debates about the nature of the process (leptonic or hadronic) that originates its gamma-ray spectrum [74]. RX J1713.7-3946 was first observed by the CANGAROO experiment which firstly claimed a leptonic origin [75]. Successive observations with CANGAROO-II [76] disfavour purely electromagnetic processes as the only source of the observed γ-ray spectrum. Neutrino calculations based on this result predicted large event rates also in neutrino telescopes with size smaller than 1 km^3 [77, 78]. This source has successively been observed with higher statistics by the HESS telescope, [79] supporting the hadronic origin. The neutrino flux calculations based on the HESS result (shown in Fig. 16) lead to the prediction that the source should be detectable in a kilometer-scale Mediterranean detector.
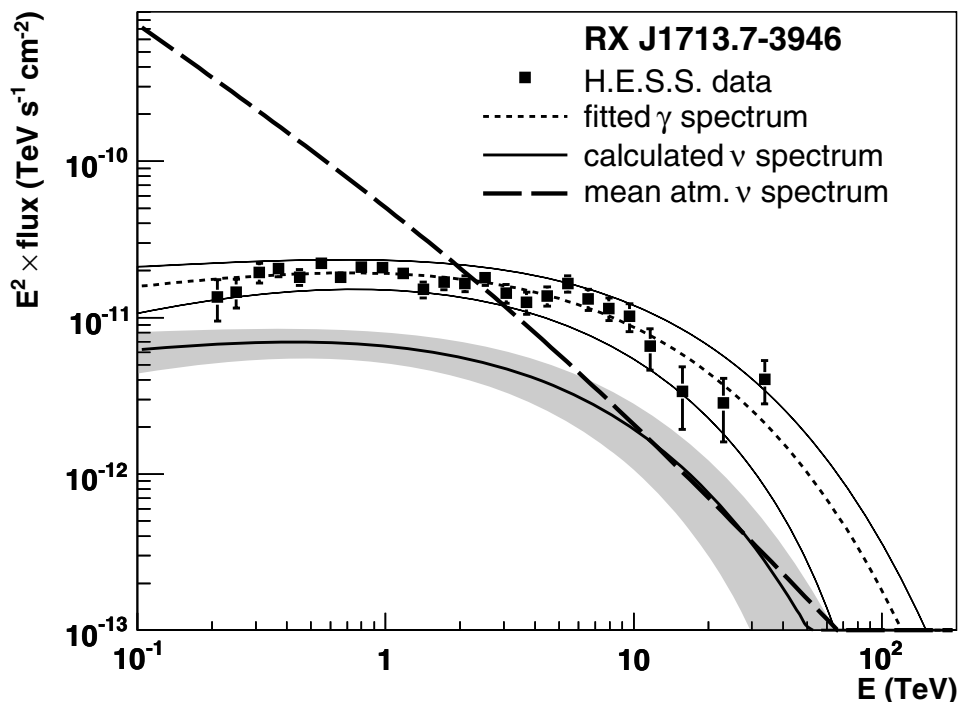
Figure 16: *Measured gamma-ray flux from RX J1713.7-3946 and estimated neutrino flux [39] with their error bands. The atmospheric neutrino flux (with error band) is integrated over the search window and averaged over one day.*

6.1.2   Pulsar wind nebulae (PWNe)

PWNe are also called Crab-like remnants, since they resemble the Crab Nebula (§3.1), which is the youngest and most energetic known object of this type. PWNe differ from the shell-type SNRs because there is a pulsar in the center which blows out jets of very fast-moving material into the nebula. The radio, optical and X-ray observations suggest a synchrotron origin for these emissions. HESS has also detected TeV γ-ray emission from the Vela PWN, named Vela X. This emission is likely to be produced by the inverse Compton mechanism, but the possibility of a hadronic origin for the observed γ-ray spectrum with the consequent flux of neutrinos was also considered [80].

The neutrino flux calculated for a few PWNe in the framework on a hadronic production of the observed TeV γ-rays (such as the Crab, the Vela X, the PWN around PSR1706-44 and the nebula surrounding PSR1509-58) agree with the conclusions that all these PWNe could be detected by a kilometre-scale neutrino telescope [81]. A negative result will help constraining the models or exclude the hadronic production.

6.1.3   The Galactic Centre (GC)

The Galactic Centre is probably the most interesting region of our Galaxy, also regarding the emission of neutrinos. It is specially appealing for a Mediterranean neutrino telescope since it is within the sky view of a telescope located at such latitude. The interest in it has increased after the recent discoveries of HESS.

Early HESS observations of the GC region detected a point-like source at the gravitational centre of the Galaxy (HESS J1745-290 [82]) coincident with the supermassive black hole Sagittarius A* and the SNR Sgr A East. In 2004, a more sensitive campaign revealed a second source, the PWN G 0.9+0.1 [83].

Thanks to the good sensitivity of the HESS telescope, it is possible to subtract the GC sources and search for the diffuse γ- ray emission which spans the galactic coordinates $|l| < 0.8^o, |b| < 0.3^o$. This diffuse emission of γ-ray with energies greater than 100 GeV is correlated with a complex of giant molecular clouds in the central 200 pc of the Milky Way [84].

The measured γ-ray spectrum in the GC region is well described by a power law with index of $\sim$ 2.3. The photon index of the γ-rays, which closely traces back the spectral index of the CR, indicates in the galactic centre a local CR spectrum that is much harder and denser than that measured on Earth, as shown in Fig. 17.

Thus it is likely that an additional component of the CR population is present in the Galactic Centre, above the diffuse CR concentration which fills the whole Galaxy. The proximity of particle accelerators in the GC, and therefore the possibility of neglecting the CR diffusion loss due to propagation (see §2.1.1), gives a natural explanation for the harder spectrum which is closer to the intrinsic CR source spectra. In [84] it is suggested that the central source HESS J1745-290 is likely to be the source of these CR protons, with two candidates for CR accelerations in its proximity: the SNR Sgr A East (estimated age around 10^4 yrs), and the black hole Sgr A*.

6.1.4   Microquasars

Microquasars are galactic X-ray binary systems, which exhibit relativistic radio jets, observed in the radio band [85]. The name is due to the fact that they result morphologically similar to the AGN, since the presence of jets makes them similar to small quasars. This resemblance could be more than morphological: the physical processes that govern the formation of the accretion disk and the plasma ejection in microquasars are probably the same ones as in large AGN.

Microquasars have been proposed as galactic acceleration sites of charged particles up to $E \sim 10^{16}$ eV. The hypothesis was strengthened by the recent discovery of the presence of relativistic nuclei in microquasars jets like those of SS 433. This was inferred from the observation of iron X-ray line [86].

Two microquasars, LS I +61 303 and LS 5039, have been detected as γ-ray sources above 100 MeV and listed in the third EGRET Catalogue. They are also detected in the TeV energy range [87, 88].

There is yet uncertainty as to what kind of compact object lies in LS I +61 303 (observed by the MAGIC telescope, with some not conclusive indication of variability in the γ-ray emission). Because the source is located in the Northern sky, it is specially appealing for a neutrino telescope located in the Southern hemisphere as IceCube, which will be able to detect (or rule out) neutrinos coming from this source [89].

Microquasar LS 5039 (detected by HESS in the Southern sky) has features similar to LS I +61 303, in particular the observed flux does not allow an unequivocal conclusion about the variability of the source. Different astrophysical scenarios have been proposed to explain the TeV γ-ray emission, which involve leptonic and/or hadronic interactions. In particular, the leptonic model is strongly disfavored in [90]. In this case for LS 5039 it is expected to be between $0.1 \div 0.3$ events/year in a detector like ANTARES (see §10.1), depending on the assumed power law neutrino spectrum (from 1.5 to 2.0), and two energy
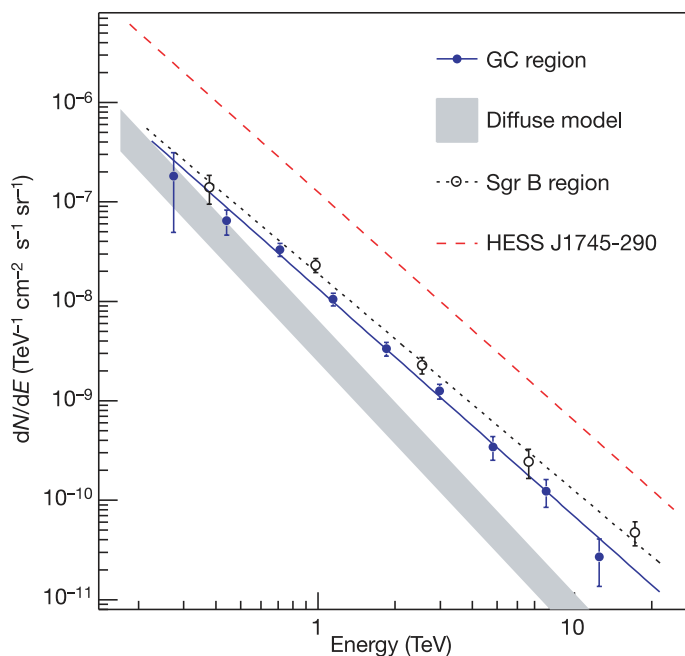
Figure 17: *(From [84]) HESS measurement of γ-ray flux per unit solid angle in the GC region (open circle data points). In comparison, the expected γ-ray flux assuming a CR spectrum as measured in the solar neighbourhood is shown as a shaded band. The measured spectrum in the galactic region $|l| < 0.8^o, |b| < 0.3^o$ is shown using full circles. These data can be described by a power law with spectral index ~ 2.3. The measured γ-ray flux (>1 TeV) implies a high-energy cosmic-ray density which is 4 to 10 times higher than our solar neighbourhood value. The spectrum of the source HESS J1745-290 is also shown for comparison.*

cutoff ($E_{max} = 10$ TeV and 100 TeV [90]).

Other microquasars were considered in [91]. The best candidates as neutrino sources are the steady microquasars SS433 and GX339-4. Assuming reasonable scenarios for TeV neutrino production, a 1 km^3-scale neutrino telescope in the Mediterranean sea could identify microquasars in a few years of data taking, with the possibility of a 5σ level detection. In case of no-observation, it would strongly constrains the neutrino production models and the source parameters.

6.1.5   Neutrinos from the galactic plane

In addition to stars, the Galaxy contains interstellar thermal gas, magnetic fields and CRs which have roughly the same energy density. The inhomogeneous magnetic fields diffusively confine the CRs within the Galaxy. CRs hadronic interactions with the interstellar material produce a diffuse flux of γ-rays and neutrinos (expected to be equal within a factor of ~ 2). The fluency at Earth is expected to be correlated to the gas column density in the Galaxy: the largest emission is expected from directions along the line of sight which

intersects most matter.

Recently, the MILAGRO collaboration has reported the detection of extended multi-TeV gamma emission from the Cygnus region [92], which is well correlated to the gas density and strongly supports the hadronic origin of the radiation. The MILAGRO observations are inconsistent with an extrapolation of the EGRET flux measured at energies of tens of GeV. This supports the hypothesis that in some areas of the galactic disk the CR spectrum might be significantly harder that the local one.

With the assumption that the observed γ-ray emission comes from hadronic processes, it is possible to obtain an upper limit on the diffuse flux of neutrinos from the galactic plane. The KM3NeT consortium [50] made an estimate of the neutrino flux from the inner Galaxy, assuming that the emission is equal to that observed from the direction of the Cygnus region. The expected signal rate for a km^3 neutrino telescope located in the Mediterranean Sea is between 4 and 9 events/year for the soft (index $\alpha = 2.55$) and hard ($\alpha = 2.10$) spectrum respectively, with an atmospheric neutrino background of about 12 events per year.

6.1.6   Unknowns

In addition to SNR, PWNe and microquasars, there are other theoretical environments in which hadronic acceleration processes could take place with production of a neutrino flux. For instance, neutron stars in binary systems and magnetars [93] might be sources of an observable neutrino flux.

New improvements in the GeV- TeV scale γ-ray astronomy are expected in the next years. In particular practically all the IAC telescopes are improving their apparatus. Fermi is a new high-energy gamma-ray observatory designed for making observations of γ-ray sources in the energy band extending from 10 MeV to more than 100 GeV. News are also expected from the ARGO [94] and MILAGRO [95] large field of view observatories. Finally, it is also worth remarking that a non-negligible number of VHE γ-ray sources detected by HESS do not have a known counterpart in other wavelengths. The origin of such sources is a theoretical challenge in which neutrino astronomy may yield some insight.

Although not certainly inspired by neutrino astronomy, it is very interesting to quote this sentence from the former US Secretary of Defense, Donald Rumsfeld. The sentence is the exact words as taken from the official transcripts on the Defense Department Web site [96]: **The Unknown.** *As we know, / There are known knowns. / There are things we know we know. / We also know / There are known unknowns. / That is to say / We know there are some things/ We do not know. / But there are also unknown unknowns, / The ones we don't know / We don't know.*

6.2   Extra-galactic neutrino sources

The extension of measured cosmic ray spectrum above the *ankle* is assumed to be the result of the contribution of extra-galactic sources (§2.1.3). The prediction of high energy neutrino sources of extra-galactic origin is a direct consequence of the CR observations.

As for the origin of UHE Cosmic Rays, Active Galactic Nuclei (AGN) are the principal candidates as neutrino sources. Other potentially promising particle accelerators are γ-ray bursts (GRBs). Here we consider these two astrophysical classes of objects, with a particular attention to the possible neutrino production mechanism. Finally, radio observation of starburst galaxies have motivated the idea of the existence of *hidden* sources of CR. These sources can represent pure neutrino accelerators, and some predictions are presented.

Extra-galactic sources are very far and the possibility of a individual discovery in a km^3 scale neutrino telescope is expected only in particular theoretical models, or using the *source stacking* methods: it is a combined analysis for different classes of objects which enhance the neutrinos detection probability.

An alternative way to prove the existence of extragalactic neutrino sources is through the measurement of the *cumulative flux* in the whole sky. Since there is no directional information, the only way to detect this *diffuse flux of high energy neutrinos* is looking for an excess of high energy events in the energy spectrum over the background of the atmospheric neutrinos.

Theoretical models constrain the neutrino diffuse flux, as we discuss in §6.2.4. These upper bounds are derived from the observation of the diffuse fluxes of γ-rays and UHECR. One of them (the Waxman-Bahcall, shortened as W&B) is used as the reference limit to the predicted neutrino flux coming from different extra-galactic sources (§6.2.4).

In addition to neutrinos generated by high energy cosmic accelerators, there are high energy neutrinos induced by the propagation of CRs in the local Universe (§2.1.3). Protons exceeding the threshold for pions production ($E_P \sim 5 \times 10^{19}$ eV), will lose most of their energy [97]. The subsequent pions decay will produce a neutrino flux (called GZK or *cosmological* neutrinos) similar to the W&B bound above 5×10^{18} eV [98], since neutrinos carry approximately 5% of the proton energy.

6.2.1 Active Galactic Nuclei (AGN)

Active Galactic Nuclei (or AGN) are galaxies with a very bright core of emission embedded in their centre, where a supermassive black hole ($10^6 \div 10^9$ solar masses) is probably present. As outlined in §2.1.3, the Auger observatory has reported the first hints of correlation between CR directions and nearby concentrations of matter in which AGN are present. This measurement (although still controversial) suggests that AGN are the most promising candidates for UHECR emission. For instance, a detailed prediction has recently been carried out for the Centaurus A Galaxy, which is only 3 Mpc away. In [99] the estimate neutrino flux from hadronic process is $E^2 d\Phi_\nu/dE \leq 5 \times 10^{-13}$ TeV^{-1} cm^{-2}s^{-1}, thus between $0.02 \div 0.8$ events/year for a cubic kilometer detector.

The supermassive black hole in the centre of AGN would attract material onto it, releasing a large amount of gravitational energy. According to some models [100], the energy rate generated with this mechanism by the brightest AGNs can be $L > 10^{47}$ erg s^{-1}. Early models [101, 102, 103] postulating the hadronic acceleration in the AGN cores predicted a production of secondary neutrinos well above the W&B upper limit, and the prediction from some of these models has been experimentally disproved by AMANDA [104]. More recent models [105] predict fluxes close to the W&B bound.

A particular class of AGN (called $blazars$) have their jet axis aligned close to the line of sight of the observer. Blazars present the best chance of detecting AGNs as individual point sources of neutrinos because of a significant flux enhancement in the jet through Doppler broadening. Blazars exhibit non-thermal continuum emission from radio to VHE frequencies and are highly variable, with fluxes varying by factors of around 10 over timescales from less than 1 hour to months. Many tens of blazars have been detected by EGRET and Fermi-LAT experiments and an increasing population of TeV blazars at higher redshifts is being detected by the latest generation of γ-ray IACT; so far 18 blazars have been discovered over a range of red-shifts from 0.03 to >0.3 [37].

In hadronic blazar models, the TeV radiation is produced by hadronic interactions of highly relativistic baryonic outflow with the ambient medium or by interactions of UHE

protons with synchrotron photons. An important effect to take into account is that the observed γ-ray spectrum from extragalactic sources is steepened due to absorption by the Extragalactic Background Light (EBL). Neutrinos, however, are unaffected by the EBL and in the case of a distant blazar, such as 1ES1101 at z=0.186, the observed spectral index of 2.9 is estimated to correspond to a spectral index as hard as 1.5 near the source [106]. Because of this hardening, some TeV-bright blazars, in some models, are expected to produce ν_μ fluxes exceeding the atmospheric neutrino background in a cubic kilometer neutrino telescope [107]. HESS recently reported also highly variable emission from the blazar PKS2155 [108]. A two order of magnitude flux increase, reaching 10 Crab Units (C.U., eq. 8) was observed during a one hour period. Such flaring episodes are interesting targets of opportunity for neutrino telescopes. Assuming that half of the γ-rays are accompanied by the production of neutrinos, a flare of 10 C.U. lasting around 2.5 days would result in a neutrino detection at the significance level of 3 sigma [50].

6.2.2 Gamma ray bursts (GRBs)

GRBs are short flashes of γ-rays, lasting typically from milliseconds to tens of seconds, and carrying most of their energy in photons of MeV scale. The likely origin of the GRBs with duration of tens of seconds is the collapse of massive stars to black holes. Recent observations suggest that the formation of the central compact object is associated with Ib/c type supernovae [109, 110, 111].

GRBs also produce X-ray, optical and radio emission subsequent to the initial burst (the so called $afterglow$ of the GRB). The detection of the afterglow is performed with sensitive instruments that detect photons at wavelengths smaller than MeV γ-rays. In 1997 the Beppo-Sax [112] satellite obtained for the first time high-resolution X-ray images of the GRB970228 afterglow, followed by successive observations made in optical and longer wavelengths with an angular resolution of arcminute. This accurate angular resolution allowed the redshift measurement and the identification of the host galaxy. It was the first step to demonstrate the cosmological origin of GRBs.

Leading models assume that a $fireball$, produced in the collapse, expands with an highly relativistic velocity (Lorentz factor $\Gamma \sim 10^{2.5}$) powered by radiation pressure. Protons accelerated in the fireball internal shocks lose energy through photo-meson interaction with ambient photons (the same process of eq. 5). In the observer frame, the condition required to the resonant production of the Δ^+ is $E_\gamma E_p = 0.2$ GeV$^2\Gamma^2$. For the production of gamma-rays with $E_\gamma \sim 1$ MeV the characteristic proton energy required is $E_p = 10^{16}$ eV, if $\Gamma \sim 10^{2.5}$. The interaction rate between photons and protons is high due to the high density of ambient photons and yields a significant production of pions, which decay in neutrinos, typically carrying 5% of the proton energy. Hence, neutrinos with $E_\nu \sim 10^{14}$ eV are expected [113]. Other neutrinos with lower energies can also be produced in different regions or stages where GRB γ-rays are originated. Depending on models, a different contribution of neutrinos is expected at every time stage of the GRB.

Some calculations of the neutrino flux [114] from GRB show that a kilometer-scale neutrino telescope can be sufficient to allow detection. The average energy of these neutrinos (100 TeV) corresponds to a value for which neutrino telescopes are highly efficient. Nevertheless, being transient sources, GRBs detection has the advantage of being practically background free, since neutrino events coming from GRB are correlated both in time and direction with γ-rays. As for the case of ANTARES [115], unfiltered data can be stored in the occurrence of a GRB alert from a satellite or a groundbased telescope. The analysis of collected data around a GRB alert can be carried out some time later, with the advantage of

using very precise astronomical data, improved by later observations of the afterglow with optical telescopes.

6.2.3   Starburst or neutrino factories

Radio observations have motivated the idea of the existence of regions with an abnormally high rate of star formation, in the so-called *starburst galaxies*, which are common throughout the Universe. These regions of massive bursts of star-formation can dramatically alter the structure of the galaxy and input large amounts of energy and mass into the intergalactic medium. Supernovae explosions are expected to enrich the dense star forming region with relativistic protons and electrons [116, 117]. These relativistic charged particles, injected into the starburst interstellar medium, would lose energy through pion production. Part of the proton energy would be converted into neutrinos by charged meson decays. Such hidden sources of CR are thus purely-neutrino accelerators, since only neutrinos would be able to escape from these dense regions. A cumulative flux of GeV neutrinos from starburst galaxies was calculated in [118] as $E_\nu^2 \Phi_\nu \simeq 10^{-7}$ GeV cm^{-2} s^{-1}sr^{-1}, a level which can be detected by a km^3-scale neutrino detector.

6.2.4   The upper limit for transparent sources

The observation of diffuse flux of gamma-rays and of UHE CRs can be used to set theoretical upper bounds on the total flux of neutrino from extragalactic sources (diffuse neutrino flux). High energy γ-rays can be produced in astrophysical acceleration sites by decay of the neutral pion (eq. 6). Neutrinos will be produced in parallel from decay of the charged pions and escape from the source without further interactions, due to their low cross section. High-energy photons from π^o decay, on the contrary, will develop electromagnetic cascades when interacting with the intergalactic radiation field. Most of the γ-ray energy will be released in the 1 MeV-100 GeV range. Therefore, the observable neutrino flux (within a factor of two due to the branching ratios and kinematics at production of charged and neutral pions) is limited by the bolometric observed gamma-ray flux in this energy band.

   The diffuse gamma-ray background spectrum above 30 MeV was measured by the EGRET experiment as [119]:

$$E^2 I_\gamma(E) = (1.37 \pm 0.06) \times 10^{-6} \, GeV \, cm^{-2} s^{-1} sr^{-1} \qquad (26)$$

   If nucleons escape from a cosmic source, a similar bound can be derived from the measured flux of CR from extragalactic origin. Fermi acceleration mechanism can take place when protons are magnetically confined near the source. Neutrons produced by photo-production interactions of protons with radiation fields (eq. 5) can escape from transparent sources and decay into cosmic protons <u>outside</u> the region of the magnetic field of the host accelerator.

   Some additional factors have to be considered before establishing a relationship between CR and neutrino fluxes. These factors take into account the production kinematics, the opacity of the source to neutrons and the effect of propagation. This last factor is the subject to the larger uncertainties, because it has a strong dependence on galactic evolution and on the poorly-known magnetic fields in the Universe. There is some controversy about how to use relationships to constrain the neutrino flux limit. There are however two relevant predictions:

- **The Waxman-Bahcall upper bound.** The upper bound proposed by Waxman-Bahcall [120] (W&B) takes the cosmic-ray observations at $E_{CR} \sim 10^{19}$ eV to constrain neutrino flux. With a simple inspection of Fig. 1, we can see that $E^2 dN/dE \sim 10^{-8}$ GeV cm^{-2}s^{-1}sr^{-1} at 10^{19} eV. This flux is two orders of magnitude lower than the limit provided by the extragalactic MeV-GeV gamma-ray background (eq. 26).

  In the computation of the upper bound, several hypothesis are made: it is assumed that neutrinos are produced by interaction of protons with ambient radiation or matter; that the sources are transparent to high energy neutrons; that the 10^{19} eV CRs produced by neutron decay are not deflected by magnetic fields; finally (and most important) that the spectral shape of CRs up to the GZK cutoff is $dN/dE \propto E^{-2}$, as typically expected from the Fermi mechanism. The upper limit that they obtain is:

  $$E_\nu^2 d\Phi/dE_\nu < 4.5 \times 10^{-8} GeV\, cm^{-2} s^{-1} sr^{-1} \qquad (27)$$

  Although this limit may be surpassed by hidden or optically thick sources for protons to pγ or pp(n) interactions, it represents the "reference" limit to be reached by neutrino telescope sensitivities (see Fig. 18).

- **Mannheim-Protheroe-Rachen (MPR) upper bound.** The W&B limit was criticized as not completely model-independent. In particular, the main observation was about the choice of the spectral index $\alpha = 2$. In [121] a new upper bound was derived using as a constraint not only the CRs observed on Earth, but also the observed gamma-ray diffuse flux. The two cases of sources *opaque* or *transparent* to neutrons are considered; the intermediate case of source partially transparent to neutrons give intermediate limits.

  The limit for sources *opaque* to neutrons is:

  $$E_\nu^2 d\Phi/dE_\nu < 2 \times 10^{-6} GeV\, cm^{-2} s^{-1} sr^{-1} \qquad (28)$$

  This is two orders of magnitude higher than the W&B limit and similar to the EGRET limit on diffuse gamma rays (eq. 26), because a source opaque to neutrons produces very few CRs (neutrons cannot escape and decay outside the source), but it is transparent to neutrinos and γ-rays.

  The limit for sources *transparent* to neutrons decreases from the value of eq. 28 at $E_\nu \sim 10^6$ GeV to the value of eq. 27 at $E_\nu \sim 10^9$ GeV. Above this energy, the limit increases again due to poor observational information.

Both the W&B and the MPR limit are reported in Fig. 18. Experimental upper limits are indicated as solid lines, ANTARES and IceCube 90% C.L. sensitivities with dashed lines. Frejus [122], MACRO [123], Amanda-II 2000-03 [104] limits refer to muon neutrinos. Baikal [124] and Amanda-II UHE 2000-02 [125] refer to neutrinos of all-flavours. The red line inside the shadowed band represents the Bartol [58] atmospheric neutrino flux. The lowest limit of the band represents the flux from the vertical direction, with a negligible contribution from prompt neutrinos. The upper limit of the band represents the flux from the horizontal direction, with one of the prompt model which gives the maximum contribution [126].
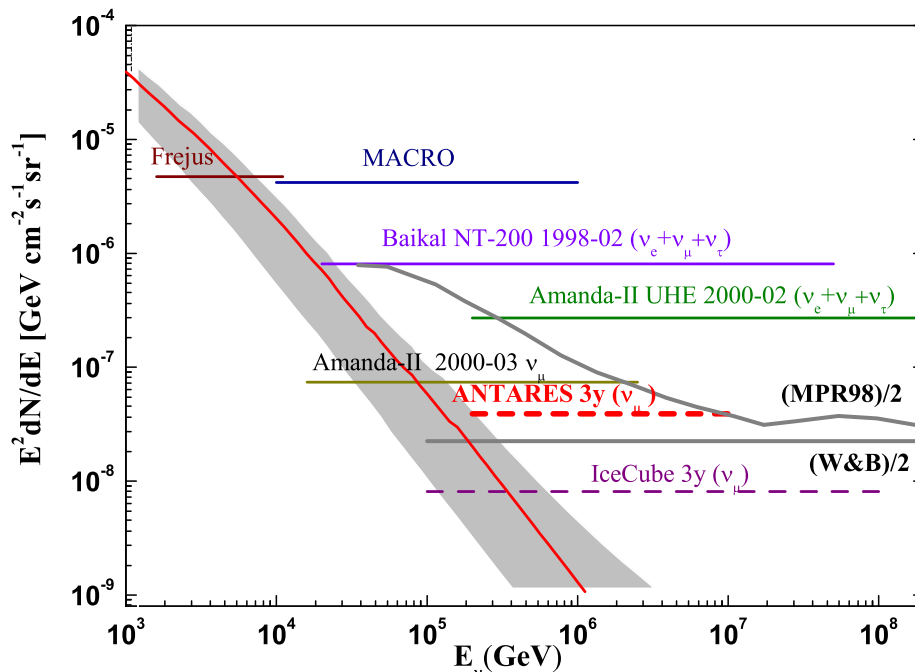
Figure 18: *Sensitivities and upper limits for a E^{-2} diffuse high energy neutrino flux, see text. Experimental upper limits are indicated as solid lines, ANTARES and IceCube 90% C.L. sensitivities with dashed lines. For reference, the W&B and MPR98 limits for transparent sources are also shown. Part of the MPR98 upper bound is already excluded by the AMANDA-II result. Both upper bounds are divided by two, to take into account neutrino oscillations.*

6.3   The effect of neutrino oscillations

Neutrino oscillation is a recent but well known phenomenon that will affect also the cosmic neutrino flavors. Neutrino oscillations were observed in atmospheric neutrinos, in solar neutrino experiments and on Earth based accelerator and reactor experiments. A complete review about neutrino oscillations can be found in [127].

As already mentioned, high energy neutrinos are produced in astrophysical sources mainly through the decay of charged pions, in $p\gamma$, pp, pn interactions (eq. 7). Therefore, neutrino fluxes of different flavours are expected to be at the source in the ratio:

$$\nu_e : \nu_\mu : \nu_\tau = 1 \,:\, 2 \,:\, 0 \tag{29}$$

Neutrino oscillations will induce flavour changes while neutrinos propagate through the Universe. One has to consider *mass eigenstates* $\nu_m = \nu_1$, ν_2, ν_3 in the propagation, instead of *weak flavour eigenstates* $\nu_l = \nu_e$, ν_μ, ν_τ. The weak flavour eigenstates ν_l are linear combinations of the mass eigenstates ν_m through the elements of the mixing matrix

U_{lm}:

$$\nu_l = \sum_{m=1}^{3} U_{lm}\, \nu_m \tag{30}$$

Because mixing angles are large, the flavour eigenstates are well separated from those of mass.

It is instructive to derive the oscillation probability in the simple case of only two flavour neutrinos, for instance $(\nu_\mu,\ \nu_\tau)$ and one mixing angle θ_{23}:

$$\begin{cases} \nu_\mu = \ \nu_2 \cos\,\theta_{23} + \nu_3 \sin\,\theta_{23} \\ \nu_\tau = -\nu_2 \sin\,\theta_{23} + \nu_3 \cos\,\theta_{23} \end{cases} \tag{31}$$

The survival probability for a pure a ν_μ beam:

$$P(\nu_\mu \to \nu_\mu) = 1 - \sin^2 2\theta_{23}\ \sin^2\left(\frac{1.27\Delta m^2 \cdot L}{E_\nu}\right) \tag{32}$$

where $\Delta m^2 = m_3^2 - m_2^2$, L is the distance travelled by the neutrino from production to detection. θ_{23} and Δm^2 may be experimentally determined from the variation of $P(\nu_\mu \to \nu_\mu)$ as a function of the zenith angle Θ, or from the variation in L/E_ν.

With three neutrino flavour, three mass differences can be defined (two linearly independent). The mass difference measured with atmospheric neutrinos is $\Delta m_{atm}^2 = \Delta m_{23}^2 \simeq \Delta m_{23}^2 = \pm 2.5 \times 10^{-3} eV^2$. For the mixing angle, $\theta_{23} \simeq 45^o$ (that correspond to maximal mixing), while θ_{13} is small. The values of Δm_{12}^2 and of the other mixing angle θ_{12} are determined by the solar neutrino experimentsand KamLand. The most recent data favors very clearly the solution with a best fit: $\Delta m_{sol}^2 = \Delta m_{12}^2 = 5 \times 10^{-5} eV^2$ and $sin^2\theta_{12} = 0.24$ ($\theta_{12} = 29.5^o$).

According to these neutrino oscillation parameters, the ratio of fluxes of neutrinos from astrophysical origin (i.e. very large baseline L) in eq. 29 changes to an observed flux ratio at Earth [128] as:

$$\nu_e : \nu_\mu : \nu_\tau = 1\ :\ 1\ :\ 1 \tag{33}$$

Theoretical predictions which does not take into account neutrino oscillations must be corrected to include this effect. In particular, muon neutrinos are reduced at Earth by a factor of two.

7   Water and Ice properties

The effects of the medium (water or ice) on light propagation are absorption and scattering of photons. These affect the reconstruction capabilities of the telescope. In fact, absorption reduces the amplitude of the Cherenkov wavefront, i.e. the total amount of light on PMTs; scattering changes the direction of propagation of the Cherenkov photons and the distribution of their arrival time on the PMTs. This degrades the measurement of the direction of the incoming neutrino.

The propagation of light in a transparent medium is quantified for a given wavelength λ, by the medium inherent optical properties: absorption $a(\lambda)$, scattering $b(\lambda)$ and attenuation $c(\lambda) = a(\lambda) + b(\lambda)$ coefficients, or, alternately, absorption $L_a(\lambda) = a(\lambda)^{-1}$, scattering
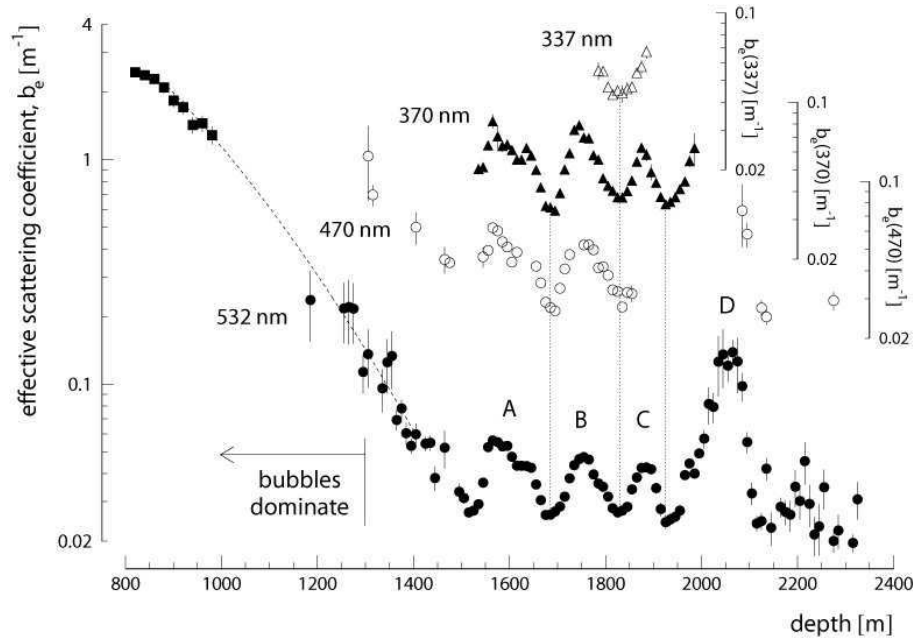
Figure 19: *Depth dependence of scattering coefficient $b_e(\lambda) = 1/L_b^{eff}(\lambda)$ as measured by the IceCube collaboration [129] for 4 different wavelengths.*

$L_b(\lambda) = b(\lambda)^{-1}$ and attenuation $L_c(\lambda) = c(\lambda)^{-1}$ lengths. Each of these lengths represents the path after which a beam on initial intensity I_0 at wavelength λ is reduced in intensity by a factor of 1/e through absorption and scattering, according to the following relation:

$$I_i(x, \lambda) = I_0(\lambda)e^{-x/L_i(\lambda)}; \quad i = a, b, c \tag{34}$$

where x (in meters) is the optical path traversed by the light.

A complete description of light scattering would require, in addition to the geometric scattering length $L_b(\lambda)$, the knowledge of the scattering angular distribution. Gustav Mie developed (1908) an analytical solution of the Maxwell equations for scattering of electromagnetic radiation by spherical particles, which is appropriate for modeling light scattering in transparent media. In particular for ice the predominant scattering centers are sub-millimeter sized air bubbles and micron sized dust particles.

Generally, light is scattered multiple times before it reaches an optical sensor. The average cosine of the light field of photons that have undergone multiple ($= n$ times) scattering obeys a simple relationship:

$$\langle \cos \theta \rangle_n = \langle \cos \theta \rangle^n \tag{35}$$

On average, per step, a photon advances at an angle of $\langle \cos \theta \rangle$ a distance of $L_b(\lambda)$ between each scatter. Hence after n scatters, a photon has moved in the incident direction:

$$L_b^{eff}(\lambda) = L_b(\lambda) \sum_{i=0}^{n} \langle \cos \theta \rangle^i \simeq \frac{L_b(\lambda)}{1 - \langle \cos \theta \rangle} \tag{36}$$

Experimental measurements are generally expressed in terms of the *effective* light scattering length $L_b^{eff}(\lambda)$, instead of the (strongly correlated) values of average scattering angle $\langle \cos \theta \rangle$ and geometric scattering length $L_b(\lambda)$.

In the following discussion, we will point out that seawater has a smaller value of $L_a(\lambda)$ with respect to ice (which is more transparent). By referring to the discussion in §5.2, the same instrumented volume of ice corresponds to a larger effective detector volume with respect to seawater. On the other hand, the effective scattering length L_b^{eff} for ice is smaller than water. This is a cause of a larger degradation of the angular resolution of the detected neutrino-induced muons in ice with respect to the water (see §7.4).

Another difference between ice and water is that optical modules in seawater suffer some background from the natural radioactivity of elements (mainly ^{40}K) and from luminescence produced by organisms living in the deep sea. Ice is (almost) background-free.

7.1   Ice properties

The ice in which AMANDA and IceCube (see §9.1) are embedded has optical properties that vary significantly with depth and that need to be accurately modeled. Impurities trapped in the ice depend on the quality of the air present when the ice was first laid down as snow. This happened over roughly the last 10^5 years. Because of variations in the long-term dust level in the atmosphere during this period, as well as occasional volcanic eruptions, impurity concentrations are depth dependent. IceCube and AMANDA have both pulsed and steady light sources located at various positions under the ice, which are used to measure both the attenuation length and scattering length. This is done by measuring the arrival time distributions of photons at different distances from a light source.

The scattering centers for light propagation in IceCube are dust particles of various types and air bubbles [129].

- There are essentially four components of the dust: insoluble mineral grains, sea salt crystals, liquid acid drops and soot. Sea salt crystals and liquid acid drops contribute negligibly to absorption, sea salt being the strongest scattering component. Insoluble mineral grains are the most common component, and contribute to both absorption and scattering, while soot contributes mainly to absorption. The relative abundance of each of these components was derived from ice core measurements [130].

- Air bubbles would play a major role in scattering in the ice of Antarctica, which is laid down through a process of snowfall, hence trapping bubbles of air as it compacts itself. This is true down to depths of approximately 1250 m below the surface. Then, the pressure of ice layers above compact these air bubbles into air hydrate crystals, which have an index of refraction nearly identical to that of ice.

Fig. 19 shows the effective scattering coefficient $b_e(\lambda)$ measured in Antarctica. The strong drop off from depths of around 1250m is due to the transition from the region where air bubbles are dominant to the region where the four main dust peaks are present in the ice.

The effects of ice properties on photon propagation and arrival times on PMTs are evaluated by the IceCube collaboration through Monte Carlo (MC) simulations. MC parameters are adjusted until an agreement is met between simulation and in situ data for photon timing distributions. Some models were developed inside the AMANDA/ IceCube collaborations [131]. The depths below AMANDA, which are now included in the active volume of Ice-Cube, were described with a model corrected using the measurements in ice cores taken at other sites in Antarctica, in particular at East Dronning Maud Land (EDML). Absorption
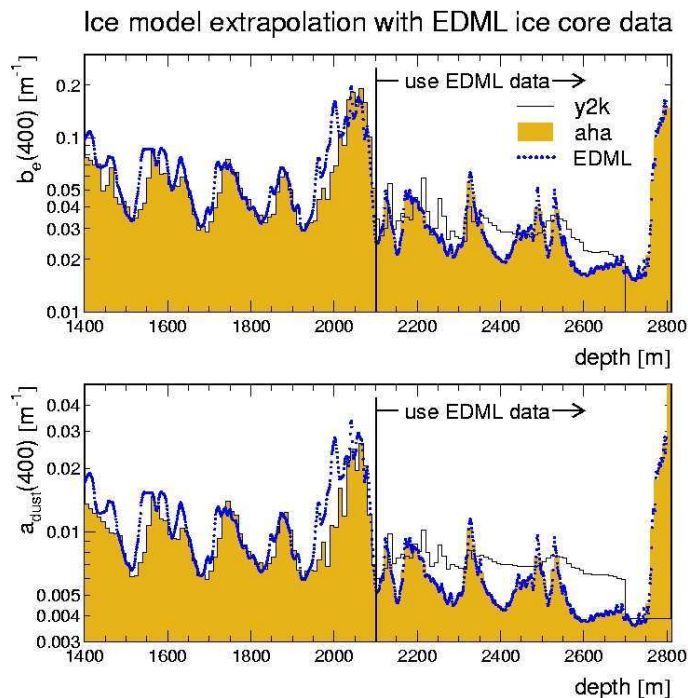
Figure 20: *Depth dependence of scattering coefficient $b_e(\lambda = 400\ nm)$ and absorption coefficient $a_{dust}(\lambda = 400\ nm)$ as used in Monte Carlo simulations in the Antarctica experiments [131].*

(due to dust) and scattering coefficients obtained with different simulations are shown in Fig. 20.

7.2 Optical properties of water

Many agents contribute to the optical properties of water. Environmental parameters such as water temperature and salinity are indicators of the aggregation state of H_2O molecules, which biases the diffusion of light. Water absorption and scattering depend also on the density and the size of the floating particulate, which affects the telescope response also in terms of detector aging: due to bio-fouling and sediments sticking on the optical modules, efficiency of the photon detection can be compromised.

For these reasons, together with the strong necessity of containing the atmospheric muon background, a site for a neutrino telescope must be located at great depth. In this condition, high pressure and extremely slow water currents make the site characteristics stable.

Apart from the BAIKAL experiment (§8.2), situated in the Siberian lake Baikal at a depth of approximately 1 km, submarine sites have been preferred in order to reach deeper locations. The preference for undersea sites is not free from drawbacks: because of the salts into the water, submarine sites present an irreducible optical background due to the ra-
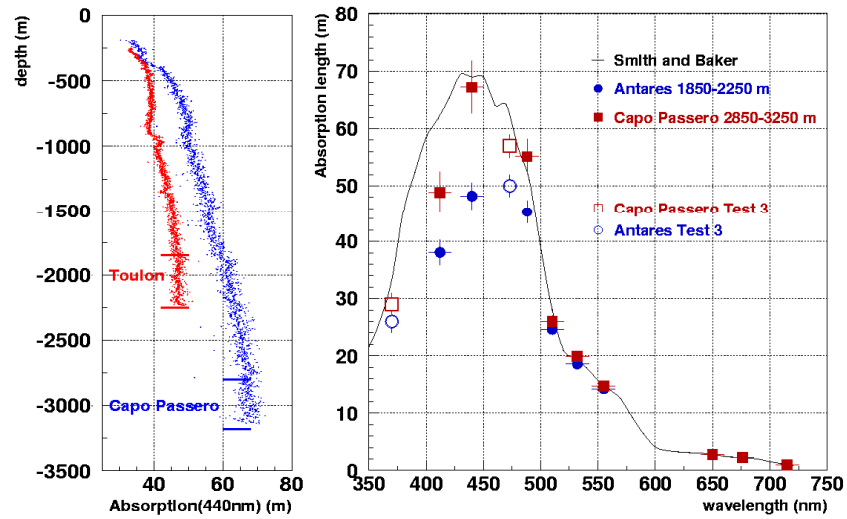
Figure 21: *The absorption length measured in the underwater sites of Toulon (blue) and Capo Passero (red), of the ANTARES (§10.1) and NEMO (see §10.2) experiments, respectively. Left: $L_a(\lambda)$ with $\lambda = 440$ nm as function of the depth. Right: various measurement of the absorption length in the two sites as function of the wavelength, compared to the behaviour of pure seawater (solid line).*

dioactive decay of ^{40}K and the bioluminescence, which strongly depends on environmental factors.

In order to minimize the bias induced by external agents, other than deep, the telescope sites must be far enough from shelf-breaks and river estuaries, which can induce turbulent currents and spoil the purity of water. At the same time, the neutrino telescope must be close to scientific and logistic infrastructures on shore. With such requirements, the Mediterranean Sea offers optimal condition on a worldwide scale to host an underwater neutrino telescope.

In water the absorption and attenuation coefficients $a(\lambda)$ and $c(\lambda)$ are directly measured by means of dedicated instruments, like the AC9 manufactured by WETLabs [132]. Water optical properties are strongly dependent on the wavelength: light transmission is extremely favoured in the range 350-550 nm [133], where the photomultipliers used in neutrino telescopes to detect Cherenkov radiation reach the highest quantum efficiency (see Fig. 13).

In natural seawater, optical properties are also function of water temperature, salinity and dissolved particulate [134, 135]. Measurements of the profiles of temperature, salinity, attenuation and absorption lengths performed by the NEMO collaboration (§10.2) in the site named *Capo Passero*, 100 km off shore from the coast of Sicily, during various sea campaigns from year 1999 to the end of year 2003 show that such quantities are stable and constant at depths greater than $1500 \div 2000$ m [136].

The nature of particulate, either organic or inorganic, its dimension and concentration, affect light propagation. All these environmental parameters may vary significantly, for each marine site, as a function of depth and time. Moreover, it is known that seasonal effects
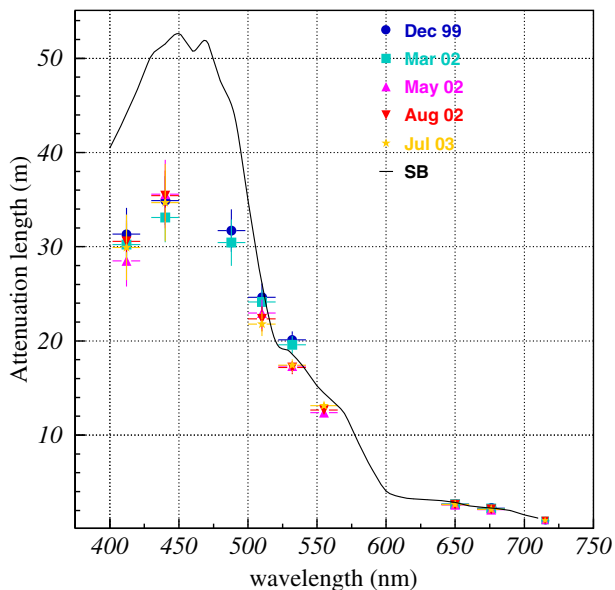
Figure 22: *Average attenuation length measured with the AC9 in the Capo Passero site [136], at depth 2850-3250 m from year 1999 to 2003. Statistical errors are plotted. The solid black line indicates the values of $L_c(\lambda)$ for optically pure seawater reported by Smith and Baker [137].*

like the increase of surface biological activity (typically during spring) or the precipitation of sediments transported by flooding rivers, enlarge the amount of dissolved and suspended particulate, worsening the water transparency.

Fig. 21 shows absorption length measured in the sites of the ANTARES experiment and the Capo Passero site. On the left it is shown the attenuation length $L_a(\lambda = 440$ nm) as a function of depth. The right side of the figure shows the measured absorption length (in the range of 350 nm $\leq \lambda \leq$ 700 nm, circle and square dots) in the two sites, compared to the model of *pure* seawater reported by Smith and Baker [137] (solid black line).

Fig. 22 shows the mean attenuation length $L_c(\lambda)$ measured in different seasons in the Capo Passero site (coloured dots); such averages are performed with measurements from 2850 m to 3250 m depth.

7.3   Optical background in water

The background counting rate in optical modules of an undersea neutrino detector has two main natural contributions: from the decay of radioactive elements in water, and from the luminescence produced by organisms, the so called bioluminescence.

The ^{40}K is by far the dominant of all radioactive isotopes present in natural seawater. ^{40}K decay channels are:

$$^{40}K \quad \rightarrow \quad ^{40}Ca \ + \ e^- \ + \ \bar{\nu}_e \ (\text{BR} = 80.3\%)$$
$$^{40}K \ + \ e^- \quad \rightarrow \quad ^{40}Ar \ + \ \nu_e \ + \ \gamma \ \ (\text{BR} = 10.7\%)$$
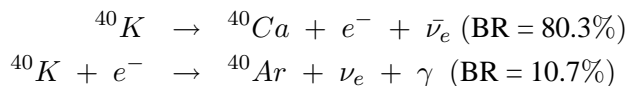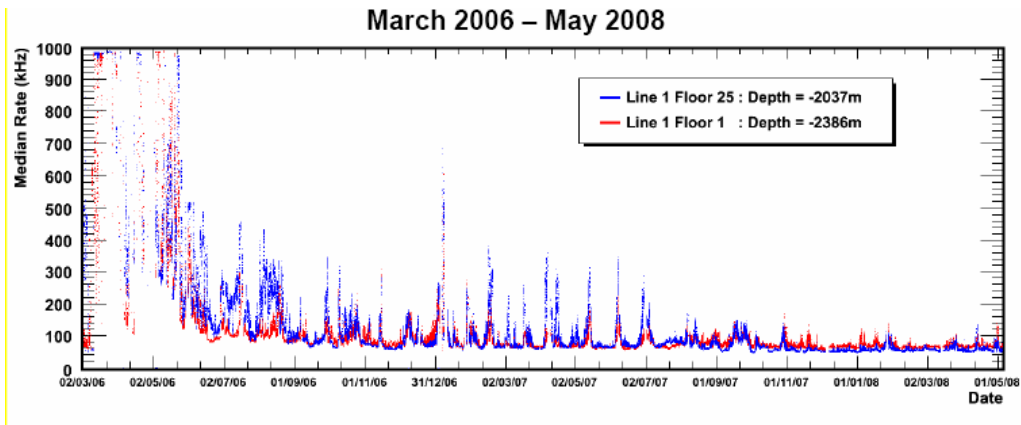
Figure 23: *Median rates (in kHz) on two different optical modules with the 10" PMT of the ANTARES experiments at 2037 m and 2386 m, form March 2006 up to May 2008 [139]. The contribution of the ^{40}K decay is almost constant to $\sim 30 - 40$ kHz.*

and both contribute to the production of optical noise. A large fraction of electrons produced in the first reaction is above the threshold for Cherenkov light production. The photon originating in the second reaction has an energy of 1.46 MeV and can therefore lead through Compton scattering to electrons above the threshold for the Cherenkov emission.

The intensity of Cherenkov light from ^{40}K radioactive decays depends mostly on the ^{40}K concentration in sea water. Since salinity in the Mediterranean Sea has small geographical variation, this Cherenkov light intensity is largely site independent.

Bioluminescence is ubiquitous in oceans and there are two sources in deep sea: steady glow of bacteria and flashes produced by animals. These can give rise to an optical background up to several orders of magnitude more intense than the one due to ^{40}K (see Fig. 23). The two components of optical background described above are clearly visible. Bursts observed in the counting rates are probably due to the passage of light emitting organisms close to the detector.

The phenomena of bioluminescence are not yet fully understood. The typical spectrum of bioluminescence light is centered around 470-480 nm [138, 140], the wavelength of maximal transparency of water, which is of greatest interest to undersea neutrino telescopes. The distribution of luminescent organisms in deep-sea varies with location, depth, and time but there is a general pattern of decrease in abundance with depth. Fig. 24 shows the amount of luminescent cultivable bacteria as a function of depth, measured in the Capo Passero site. Such measurements show a bioluminescence that is significantly lower with respect to what discovered at similar depth in the Atlantic Ocean [141, 142].

Deep sea currents were monitored at the ANTARES, NEMO and Nestor sites for long time periods. ANTARES found that the baseline component is neither correlated with sea current, nor with burst frequency; however, long-term variations of the baseline were observed. Periods of high burst activity are not correlated with variations of the baseline component, suggesting that each of the two contributions is caused by a different population. Moreover, a strong correlation is observed between bioluminescence phenomena and the current velocity, as shown in Fig. 25.
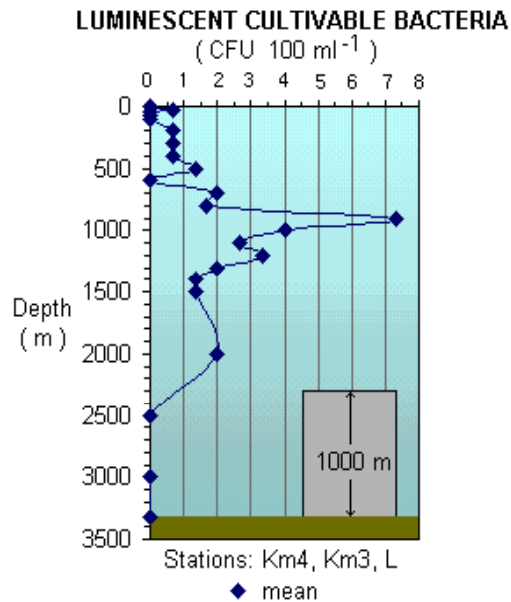
Figure 24: *The amount of luminescent bacteria, sampled in 2000 from the Capo Passero site at different depths, cultivable at atmospheric pressure.*

7.4 Tracking events in water and ice

In a 1 km^3 scale detector, single muon or muon bundle (group of parallel muons from an air shower) produce tracks which are visible over more than 1 km. This long lever arm allows for good directional reconstruction, depending on the medium (water or ice), number and orientation of the optical sensors.

Fig. 26 shows the angular resolution in ice and water resulted from MC calculations. For neutrino-induced muons (up-going) with $E_\mu > 1$ TeV, the directional resolution is of the order of few tenths of degree in water and around 1 degree in ice.

It is also possible a rough estimate of the muon energies either by the length of their tracks, or by measuring the specific energy loss; at energies above 1 TeV, muon energy loss (dE/dx) is proportional to muon energy.

Electron neutrinos, neutral current neutrino interactions and low-energy (below 1 PeV) ν_τ interactions inside the instrumented volume of the detectors produce a 'cascade', a compact deposition of energy. ν_τ interactions of few-PeV form a 'double-bang' event topology. The interaction produces one cascade near the point where the ν_τ interacts. That interaction produces a τ, which, at PeV energies, can travel hundreds of meters before decaying. The second cascade comes when the τ decays.

The bulk of reconstructed events in any neutrino telescope are downward going muons produced in cosmic-ray air showers (see Fig. 8). Rejection of this background is a significant difficulty which must be dealt with in event reconstruction.

Muon reconstruction is done by maximum likelihood methods. The fitter finds the likelihood for different track positions and directions, and, optionally, energy. To do this, it uses functions which model the light propagation, giving the Probability Distribution
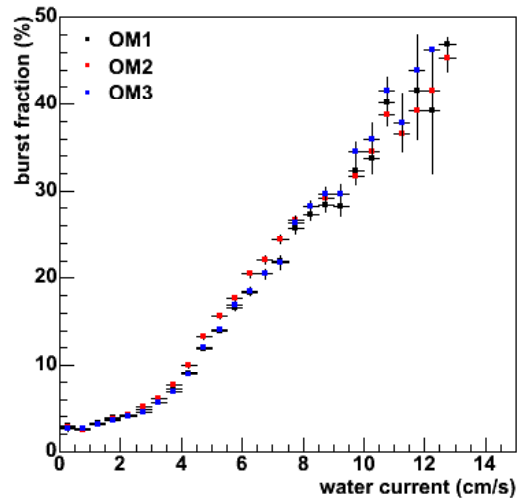
Figure 25: *Correlation between the burst fraction and the seawater current velocity as measured by the ANTARES detector. The burst fraction is the fraction of time with count rates exceeding 120% of the baseline rate.*

Function (PDF) for a photon radiated from a track with a given orientation to reach a PMT at a given perpendicular distance and orientation as a function of time. Usually, these functions are pre-calculated using a simulation that tracks photons through the medium [145, 146].

Because of the high rate of downward going muons, it is not enough to select events with the most likely reconstruction as upward going. Fairly stringent cuts must be applied to eliminate tracks with reasonable likelihoods for being downward going. This can be done by cutting on estimated errors from the likelihood fit, or using other quality estimators. The exact cuts depend on the medium (water or ice); cuts are also analysis-dependent, since different analyses are interested in signals from different energy ranges and zenith angles.

One main difference exists between ongoing and proposed underwater experiments and the ice experiments at the South Pole. The depth of the upper level of IceCube (§9.1) is ~ 1450 m of ice and the detector is large enough to have a significant background due to random coincident muon events. This happens when two (or more) muons from independent cosmic-ray air showers traverse the detector in the same time-windows (few μs) of one event. This is true also for AMANDA-II, where the estimated trigger rates of those events is 80 Hz [104]. Underwater experiments are proposed deeper and this effect is largely reduced (it is completely negligible for the ANTARES case [147]). In IceCube, specific algorithms have been developed to find and reject these events, by separating hits from the two tracks based on their separation in space and/or time. The precision in the measurements of muon direction in ice and water are shown in Fig. 26.
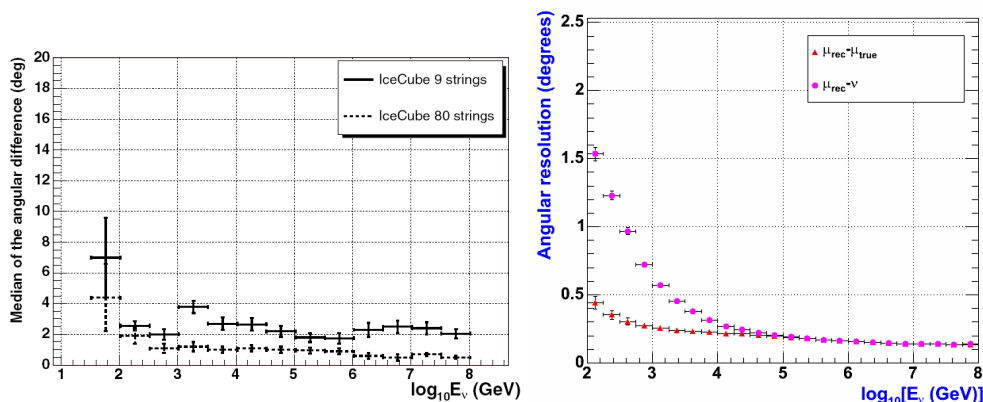
Figure 26: *(Left) MC evaluated angular resolution for 9 strings and for the full IceCube array as a function of event energy [143]. It is shown here the differences between true and reconstructed muon track. (Right) The same, for the underwater ANTARES detector. In this case, it is also shown the difference with respect to neutrino direction.*

8   The pioneers: DUMAND and Lake Baikal experiments

8.1   The prototype: DUMAND

The project of realizing the Markov idea was started in 1973 during the Cosmic Ray Conference in Denver. The Deep Underwater Muon And Neutrino Detection (DUMAND) project [148, 149] was born somewhere in 1976 and existed through 1995. The goal was the construction of the first deep ocean neutrino detector, to be placed at a 4800 m depth in the Pacific Ocean off Keahole Point on the Big Island of Hawaii. Many preliminary studies were carried out, from technology to ocean optics. A prototype vertical string of instruments suspended from a special ship was employed to demonstrate the technology, and to measure the cosmic ray muon flux at various depths (2000-4000 m, in steps of 500 m) in deep ocean [150].

A major operation took place in December 1993, when one string of photo-detectors, a string of environmental instruments and a junction box were placed on the ocean bottom and cabled to shore. While the cable laying was successful, short circuits soon developed in the instruments and it was no longer possible to communicate with the installed apparatus. In 1995 the US DOE cancelled further efforts on DUMAND.

All subsequent designs for underwater experiments have taken advantage of this experience. Some reasons for the long DUMAND development time were: i) huge depth of the chosen site; ii) lack of advanced fibre-optics technology for data transmission; iii) lack of reliable pressure-resistant underwater connectors; iv) lack of Remotely Operated Vehicle (ROV) for underwater connections; v) limited funding.

The Baikal group has been working in Lake Baikal in Siberia for about the same time as the DUMAND group in Hawaii. Initially, in the mid-1970's, the groups worked together. However, political problems developed after the Soviet invasion of Afghanistan, and the US DUMAND group was told by its government (Reagan administration) that no funding would be available to collaborate with the Soviet groups. Hence the teams reluctantly took

separate paths.

8.2   The experiment in Lake Baikal

The possibility to build a neutrino telescope in the Russian Lake Baikal was born with the basic idea of using the winter ice cover as a platform for assembly and deployment of instruments, instead of using a ship [151]. After initial small size tests, in 1984-90 single-string arrays equipped with 12 - 36 PMTs were deployed and operated via a shore cable. During this period, underwater and ice technologies were developed, optical properties of the Baikal water as well as the long-term variations of the water luminescence were investigated in great detail. Deep Baikal water is characterized by an absorption length of $L_a(480\text{nm}) = 20 \div 24$ m, an effective scattering length of $L_b^{eff} = 30 \div 70$ m and a strongly anisotropic scattering function with a mean cosine of scattering angle $\langle \cos\theta \rangle = 0.85 \div 0.9$.

The Baikal Neutrino Telescope NT-200 was a second generation detector, deployed in Lake Baikal 3.6 km from shore at a depth of 1.1 km. It consists of 192 optical modules (OMs). In April 1993, the first part of NT-200, the detector NT-36 with 36 OMs at 3 short strings, was set into operation. A 72-OMs array (NT-72) ran in 1995-96. In 1996 it was replaced by the four-string array (NT-96). Since April 1997 a six-string array with 144 OMs, take data in Lake Baikal (NT-144). NT-200 array was completed in April, 1998. NT200 plus the new external strings form NT200+ (Fig. 27). An umbrella like frame
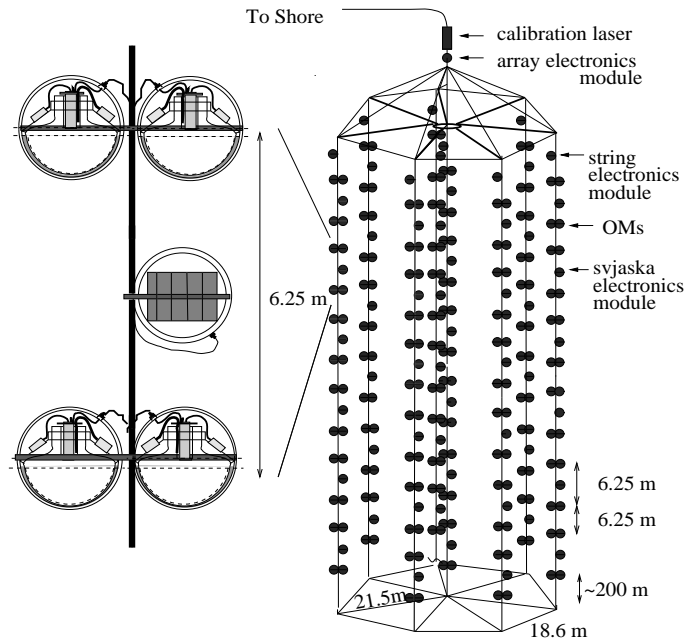

Figure 27: *Sketch of the NT-200 Baikal experiment. The expansion left-hand shows 2 pairs of optical modules (svjaska) with the svjaska electronics module, which houses part of the readout and control electronics.*

carries 8 strings 72 m long, each with 24 pair wise arranged optical modules (OMs). The

OMs contain 37cm PMT QUASAR370 and are grouped in pairs along the strings. The PMs of a pair are switched in coincidence in order to suppress background from bioluminescence and PMT noise [152].

The search strategy for high energy neutrinos relies on the detection of the Cherenkov light emitted by cascades, produced by neutrino interactions in a large volume below NT-200. The results of a search for high energy $\nu_e + \nu_\mu + \nu_\tau$ [124] is $E^{-2}d\Phi/dE < 8.1 \times 10^{-7}$ GeV cm^{-2} s^{-1} sr^{-1} in the energy range of 2×10^4 to 5×10^7 GeV, see Fig. 18.

9   Detectors in the South Pole ice

9.1   The IceCube Project

Neutrino detection requires a thick ice sheet and an experiment at the South Pole, at the Amundsen-Scott station where the ice is about 2800 m deep, was pioneered by the AMANDA collaboration. They drilled holes in the ice using a hot water drill, and lowered strings of optical sensors before the water in the hole refreeze.

The first AMANDA string was deployed in 1993, at a depth of 800-1000 m. It was quickly found that at that depth the ice had a very short scattering length, less than 50 cm (Fig. 19). In 1995-6 AMANDA deployed 4 strings between 1500 and 2000 m deep. These detectors worked as expected, and AMANDA detected its first neutrinos [4]. This success led to AMANDA-II, which consisted of 19 detector strings holding 677 optical sensors.

AMANDA was limited by its small size and some technological problems [153]. Its optical sensors consisted of photomultipliers (PMTs) with resistive bases in a pressure vessel. Not all of the optical modules survived the high pressures present when the water in the drill holes froze and AMANDA consumed considerable electrical power and required manpower-intensive calibrations yearly.

High voltage was generated on the surface, and analogue signals were returned to the surface. In AMANDA several transmission media were tried: coaxial cables, twisted pairs, and optical fibers. The 2.5 km long coaxial cables and twisted pairs dispersed the PMT pulses, while the optical fibers (in roughly half of the OMs) had a very limited dynamic range.

IceCube was designed to avoid these problems and to be much simpler to deploy, operate and calibrate. When it is complete in 2011, it will consist on a deep detector (InIce) and a surface detector (IceTop), see Fig. 28. The design of the main InIce part of the detector [154] consists of 80 strings, buried 1450 to 2450 meters under the surface of the ice, each bearing 60 Digital Optical Modules (DOMs), with 17 m spacing. The strings are placed on a 125 m hexagonal grid, providing a 1 km^3 instrumented volume. The surface electronics are in a counting house located in the center of the array.

The IceTop surface air-shower is an array of 80 stations [155] for the study of extensive air showers. Each IceTop station, located above an IceCube string, consists of two tanks filled with ice. Each of those tanks contains two DOMs of same design as the one used for the InIce part of the detector. The surface array can be operated looking for anti-coincidence with the InIce events to reject downgoing muons. It can also be used in coincidence, to provide a useful tool for cosmic ray composition studies. The array covers an area of about 1 km^2 as shown in Fig. 28. The completed detector will be operated for 20 years.

Because of the Antarctic weather, high altitude and remote location of the South Pole, logistics is a key issue. The construction season lasts from Austral summer, roughly November through mid-February. Everything needed must be flown to the Pole on ski-
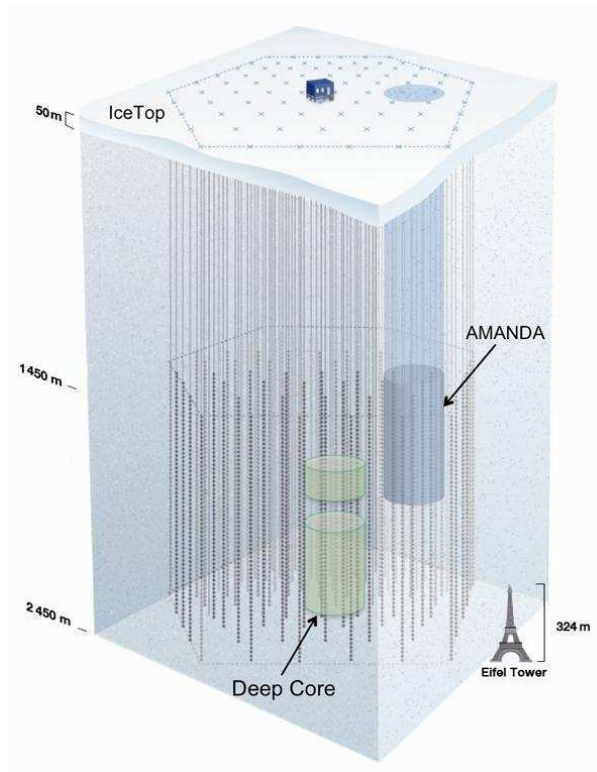
Figure 28: *The IceCube detector side view. Currently there are 59 buried InIce strings. The AMANDA detector appears in the right part of InIce. The IceTop surface array and the DeepCore are also shown.*

equipped LC-130 transports planes. The main task in IceCube construction is drilling holes for the strings. This is done with a 5 MW hot-water drill, which generates a stream of $\sim$ 800 litres/minute of 88^oC water. This water is propelled through a 1.8 cm diameter nozzle, melting a hole through the ice. Drilling a 2500 m deep, 60 cm diameter hole takes about 40 hours. Deploying a string of DOMs takes about another 12 hours.

Data acquisition with the partially finished IceCube detector is running smoothly and the detector is operating as expected. The detector began taking data in 2006 with a nine-string configuration (IC-9) and with a 22-string configuration in 2007 (IC-22) [156]. During the Austral summer 2007/08 18 more strings were buried, and 19 during the summer 2008/09. Currently (May 2009) 59 InIce strings with 3540 DOMS are deployed. Data acquisition with AMANDA also continues, enabling analyses with more than 7 years of accumulated data.

9.1.1 The IceCube Data Acquisition System

Each DOM used by IceCube comprises a 10" Hamamatsu R7081-02 PMT housed in a glass pressure vessel and in situ data acquisition (DAQ) electronics. This electronics is the heart

Figure 29: *The hot water hose and support cables disappear down one of one of boreholes drilled into the Antarctic ice to construct the IceCube Neutrino Observatory. Photo: Jim Haugen [157]*

of the DAQ system: it reads out, digitizes, processes and buffers the signals from the PMT. When individual trigger conditions are met at the DOM, it reports fully digitized waveforms to a software-based trigger and event builder on the surface. The electronics acquire in parallel, on Analog Transcient Waveform Digitizers (ATWDs) at 300 megasamples per second, sampling over a 425 ns window. In addition the electronics also record the signal with a coarser 40 megasamples per second sampling over a 6.4 μs window to record the late part of the signals. Two parallel sets of ATWDs on each DOM operate to reduce the dead-time: as one is active and ready to acquire, the other is read out.

Data is transmitted to the surface via a single twisted copper cable pair, which also provides power. Each DOM consumes about 3.5 W. The cable also includes local coincidence circuitry, whereby DOMs communicate with their nearest neighbours. A more robust connector is used than in AMANDA, and a higher fraction of IceCube OMs survive the freezing of the ice. The main requirement for the IceCube hardware is high reliability without maintenance. Once deployed, it is impossible to repair a DOM. About 98% of the DOMs survive deployment and freeze-in completely; another 1% have lost their local coincidence connections, but they are usable. On the surface, the cables are connected to a custom PCI card in a PC; the remainder of the system is off-the-shelf.

Each DOM also contains a 'flasher' board, which has 12 blue (405 nm) LEDs mounted around its edges. These LEDs are used for calibrations, to measure light transmission and timing between different DOMs, to check the DOM-to-DOM relative timing and study the optical properties of the ice. The time calibration yields a timing resolution with a RMS narrower than 2 ns for the signal sent by the DOM to the surface [158]. The noise rate due to random hits observed for InIce DOMs is of the order of 300 Hz, which gives the possibility to monitor the DOM hit rates. This very low value make the detector able to

have a sensitivity to low energy (MeV) neutrinos from supernova core collapse in the Milky Way and in the Large Magellanic Cloud [159].

Data from the DOMs is time-sorted, combined into a single stream, and then monitored by a software trigger. The main trigger is based on multiplicity: it requires eight DOMs (with local coincidences) fired within 5 μs. This collects most of the neutrino events. Starting from 2008, a string trigger which improved sensitivity for low energy, requiring five out of seven adjacent DOMs fired within 1.5 μs, was added. When any trigger occurs, all data within the $\pm 10\mu s$ trigger window is saved, becoming an event. If multiple trigger windows overlap, then all of the data from the ORed time intervals are saved as a single event.

The total trigger rate for 40 strings was about 1.4 kHz. The majority of the triggers (about 1 kHz) are due to cosmic-ray muons. A fast on-line filter system reduces the triggered events (6% survives, for a data rate of $\sim$30 Gbytes/day), and selected events are transmitted via satellite to the Northern hemisphere. The rest of the data is stored on tapes at the South Pole station, and tapes are carried North during the Austral summer.

9.1.2   Summary of the AMANDA-II results

IceCube has also integrated its predecessor, the AMANDA-II detector (the final configuration of the AMANDA detector as an independent entity). AMANDA is now surrounded by IceCube (see Fig. 28) and it consists of 677 analogic OMs distributed on 19 strings (with spacing of approximately 40 m), corresponding to a lower energy threshold for neutrino detection. For relatively low energy events, the dense configuration of AMANDA gives it a considerable advantage over IceCube. Moreover, IceCube strings surrounding AMANDA can be used as an active veto against cosmic ray muons, making the combined IceCube + AMANDA detector considerably more effective for low energy studies than AMANDA alone.

AMANDA-II has been taking data between 2000 and 2004. This subset on the 5 years of data yields 4282 up-going neutrino candidates with an estimated background from wrongly reconstructed down-ward going muons of approximately 5%. The analysis for point sources in the Northern hemisphere sky [160] for this dataset yielded no statistically significant point source of neutrinos. The highest positive deviation corresponds to about 3.7σ. The estimated probability of such a deviation or higher due to background was 69%. Assuming as usual a source of muon neutrinos with energy spectrum of E^{-2}, an upper limit was placed averaged over declination in the Northern hemisphere sky at 90% confidence level: $E^{-2}d\Phi/dE < 5.5 \times 10^{-8}$ GeV cm^{-2} s^{-1} in the energy range from 1.6 TeV up to 2.5 PeV.

Over the same period of time, a search for neutrino emission from 32 pre-selected specific candidate sources has been performed [160]. No statistically significant evidence for neutrino emission was found, Fig. 35. The highest observed significance, with 8 observed events compared to 4.7 expected background events (1.2σ), is at the location of the GeV blazar 3C273.

In addition to searches for individual sources of neutrinos, AMANDA-II data taken between 2000 and 2003 have been used to set a limit on possible diffuse flux of neutrinos. As described in §6.2.4, this diffuse flux can be distinguished from the background of atmospheric neutrinos due to its harder spectra. This study relies on the number of triggered OMs which serve as an energy estimator. A limit of $E^{-2}d\Phi/dE < 7.4 \times 10^{-8}$ GeV cm^{-2} s^{-1} sr^{-1} was placed (see Fig. 18) on the diffuse muon neutrino in the energy range from 16 TeV to 2.5 PeV at 90% confidence level [104]. Additionally, AMANDA-II has searched for an all-flavour diffuse flux from the Southern sky, setting a limit of $E^{-2}d\Phi/dE < 2.7 \times 10^{-7}$

GeV cm^{-2} s^{-1} sr^{-1} in the energy range of 2×10^5 to 10^9 GeV [125].

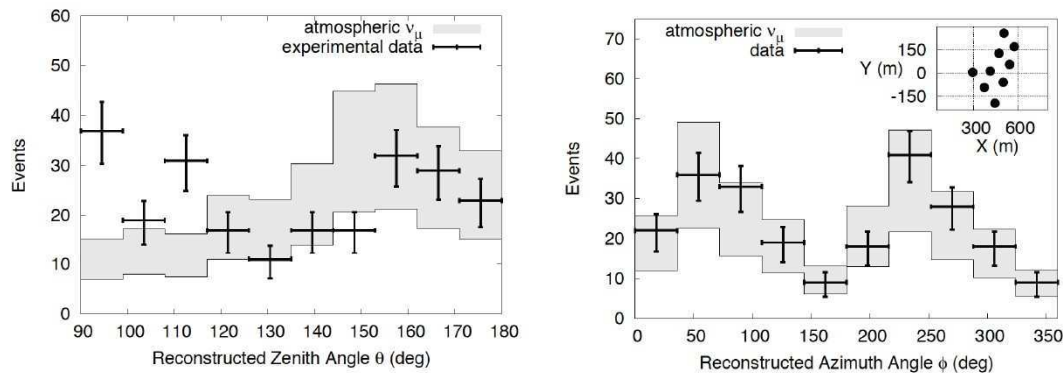### 9.1.3 First results from the IceCube 9 and 22 strings configuration

Figure 30: *Reconstructed zenith (on the left) and azimuth (on the right) angle distributions for the final sample of IC-9 events. A zenith angle of 90° (180°) corresponds to horizontal (straight up-going) event. The shadowed area indicates expectations with systematic errors. The error bars are statistical only. The configuration of the IceCube strings seen from the top is also plotted (box on top of the right). The preferred axis of this configuration explains the features observed in the azimuth angle distribution.*

The IC-9 dataset has a total livetime of 137.4 days taken between June and November 2006. 234 neutrino candidates were identified on this data sample with $211 \pm 76_{syst} \pm 14_{stat}$ events expected from atmospheric neutrinos and less than 10% pollution by the background of down-going muons [161]. Zenith and azimuth angle distributions of these neutrino candidates are shown on Fig. 30. Agreement with simulation is good except for a discrepancy near the horizontal direction due to a residual contamination of down going muons.

The IC-22 detector took data in 2007-2008, with a lifetime of 276 days [162]. This data has been analyzed to search for extraterrestrial point sources of neutrinos using two methods: the binned and the unbinned maximum likelihood method.

The binned method distinguishes a localized excess of signal from a uniform background using a circular angular search bin. The search bin radius depends on declination, and the mean value is 2.1^o. The unbinned maximum likelihood method [163] constructs a likelihood function which depends on signal Probability Density Function (PDF) and background PDF, for a given source location and total number of data events. The number of signal events is found by maximizing the likelihood ratio of the background plus signal hypothesis against the background-only case. Each analysis has followed its own event selection criteria, arriving at a final sample of 5114 (2956) events for the unbinned (binned) method. From simulation, a sky-averaged median angular resolution of 1.4^o is estimated for signal neutrinos with E^{-2} spectrum.

The results from the all-sky search for both analyses are shown in Fig. 31. The best sky-averaged sensitivity (90% C.L.) is $E^{-2}d\Phi/dE < 1.3 \times 10^{-8}$ GeV cm^{-2} s^{-1} to a generic E^{-2} spectrum of ν_μ over the energy range from 3 TeV to 3 PeV. No neutrino point sources

are found from the individual directions of a pre-selected catalogue nor in a search extended to the northern sky. Limits are improved by a factor of two compared to the total statistics collected by the AMANDA-II detector and by IC-9 [164] and represent the best results to date.

A search for neutrinos coming from 26 galactic and extragalactic pre-selected objects has also been performed on this dataset. The most significant excess over the expected background on these sources was found at the Crab nebula with 1.77σ, which again is consistent with random fluctuations. IceCube data can be used to probe the diffuse flux of neutrino from an unresolved population of astrophysical sources [165]. The sensitivity of IC-9 was only a factor of 2 above the value of AMANDA-II despite the much shorter integrated exposure time.

9.1.4   The future

During the coming years, IceCube will continue to grow starting from present configuration of 59 InIce strings. The capabilities of IceCube will be extended at both lower and higher energies in the near future. A compact core of 6 strings using IceCube DOM technology, called the DeepCore detector, will be deployed near the center of the main InIce detector, Fig. 28. The inter-string spacing will be of the order of 72 m, allowing for the exploration of energies as low as 10-20 GeV. Surrounding IceCube strings will be used as an active veto to reduce the atmospheric muon background. The energy range that will be explored is very important for dark matter searches that were initiated with AMANDA [166, 167].

Moreover, the ability to select contained events opens the search for downgoing astrophysical neutrino signals at low energies. This will allow looking above the current horizon of IceCube, even opening the possibility of looking at the galactic center or at the RX J1713.7-3946 source [168].

At EeV energies a possible extension of IceCube is also being studied in order to increase the detection volume and to be sensible to the GZK neutrino using radio and/or acoustic detection of the signals generated by neutrino interacting in a huge volume of ice. With attenuation lengths of the order of a kilometer for acoustic (kHz frequency range) and for radio signals (MHz frequency range), a sparse instrumentation will be sufficient for this extension. Two projects are currently being explored: AURA (Askarian Underice Radio Array) for the radio signal [169] and SPATS (South Pole Acoustic Test Setup) for the acoustic signal [170] . They are currently studying the polar ice and developing the hardware necessary to build a hybrid detector enclosing IceCube.

10   The underwater neutrino projects in the Mediterranean Sea

10.1   The ANTARES experiment

The ANTARES project [171] has been set up in 1996 [172]. Today it involves about 180 physicists, engineers and sea-science experts from 24 institutes of 7 European countries. ANTARES is at present the largest neutrino observatory in the Northern hemisphere, which represents a privileged sight of the most interesting areas of the sky like the Galactic Centre, where many neutrino source candidates are expected.

From 1996 to 1999 an extensive R&D program has been successfully performed to prove the feasibility of the detector concept. Site properties have been studied such as: optical properties of the surrounding water [173]; biofouling on optical surfaces [174]; optical
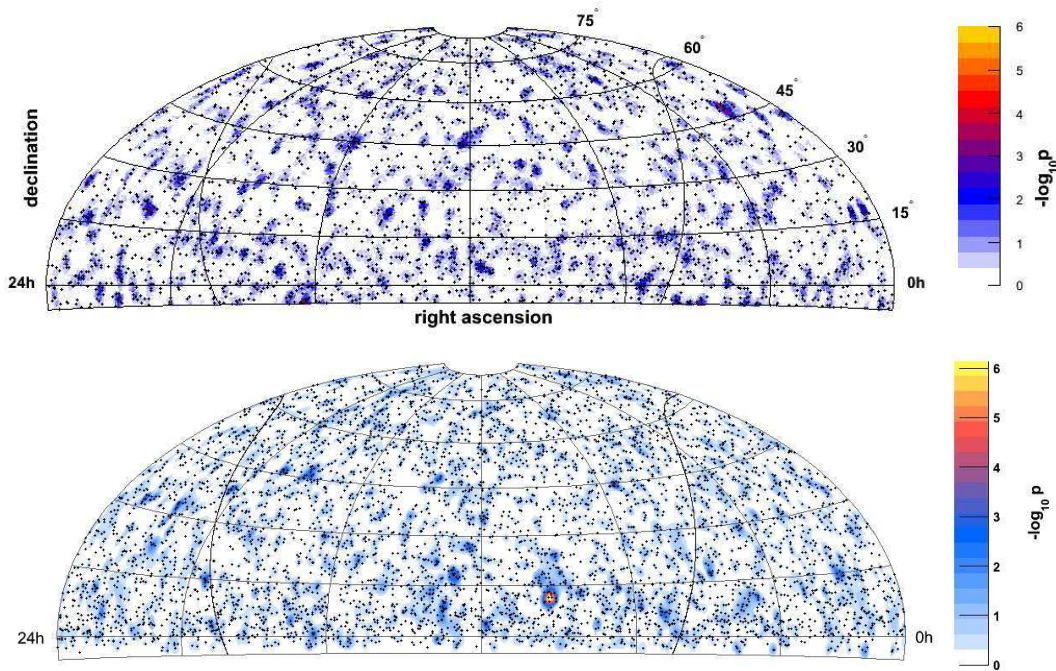
Figure 31: *IC-22 skymap with pre-trial p-values (in colors) and event locations (dots). Top: binned method. Bottom: unbinned method. Each method uses a different direction reconstruction technique [162].*

backgrounds due to bioluminescence and to the decay of the radioactive salts present in sea water [175]; geological characteristics of its ground. These studies lead to the selection of the current site, 40 km off La Seyne-sur-Mer (France) at a 2475 m depth.

A mini-instrumented line has been in operation since March 2005 [176]. The first detector line (also called *string*) was connected in March 2006 [177], and the second line in September 2006. In July 2007, three more lines were connected, and data acquisition with five lines lasted up to December 2007. In this month, five more strings plus a dedicated instrumented line [178] for monitoring environmental quantities were connected. Finally, the detector was completed with the connection of the last two strings on May, 30th 2008. The strings are made of mechanically resistant electro-optical cables anchored at the sea bed at distances of about 70 m one from each other, and tensioned by buoys at the top. Fig. 32 shows a schematic view of the detector array indicating the principal components of the detector. Each string has 25 storeys, which could be considered the elemental part of the detector. Each storey contains three optical modules (OM) and a local control module for the corresponding electronics. The OMs are arranged with the axis of the PMT 45° below the horizontal. In the lower hemisphere there is an overlap in angular acceptance between modules, permitting an event trigger based on coincidences from this overlap.

On each string, and on the dedicated instrumented line, there are different sensors and instrumentation (LED beacons, hydrophones, compasses/tiltmeters) for timing and position calibration. The first storey is about 100 m above the sea floor and the distance between
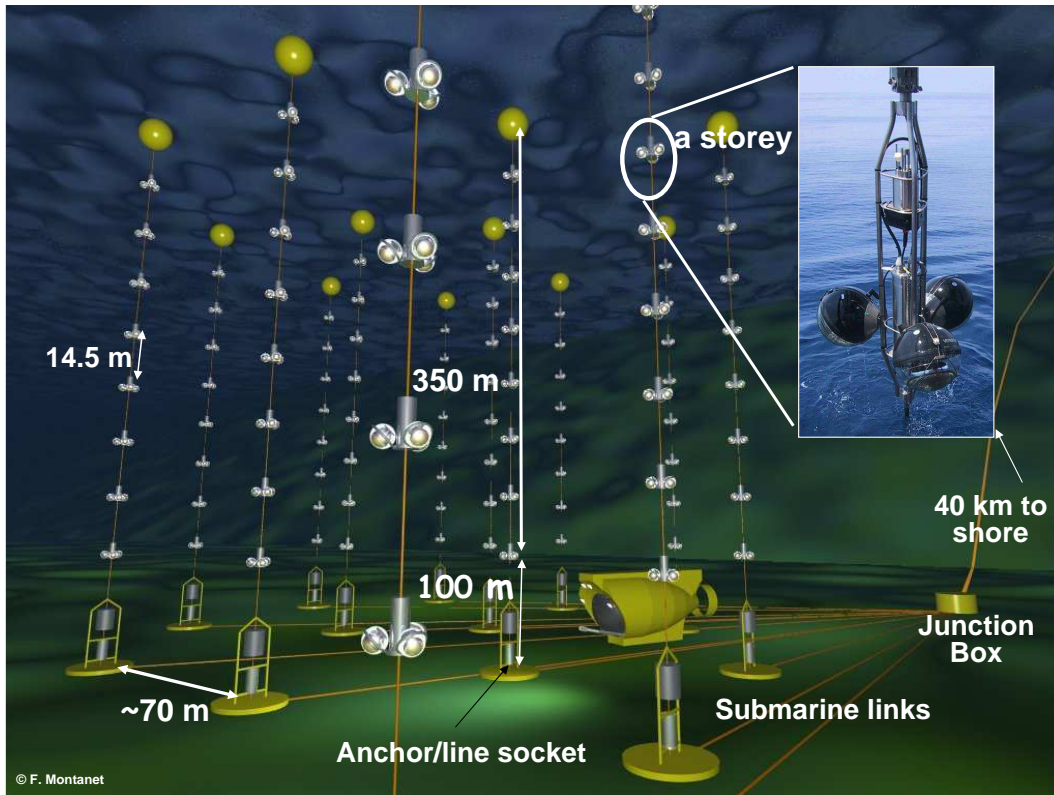
Figure 32: *Schematic view of the ANTARES detector*

adjacent storeys is 14.5 m. The instrumented volume corresponds to about 0.05 km^3.

The basic unit of the detector is the optical module (OM), consisting of a photomultiplier tube, various sensors and associated electronics, housed in a pressure-resistant glass sphere [179]. Its main component is a 10" hemispherical photomultiplier model R7081-20 from Hamamatsu (PMT) glued in the glass sphere with optical gel. A μ-metal cage is used to shield the PMT against the Earth magnetic field. Electronics inside the OM are the PMT high voltage power supply and a LED system used for internal calibration.

The total ANTARES sky coverage is 3.5π sr, with an instantaneous overlap of 0.5π sr with that of the IceCube experiment. The Galactic Centre will be observed 67% of the day time.

10.1.1   The ANTARES Data Acquisition System

The Data acquisition (DAQ) system of ANTARES is extensively described in [180]. The PMT signal is processed by an ASIC card (the Analogue Ring Sampler, ARS) which measures the arrival time and charge of the pulse. On each OM, the counting rates exhibit a baseline dominated by optical background due to sea-water ^{40}K and bioluminescence coming from bacteria, as well as bursts of a few seconds duration, probably produced by bioluminescent emission of macro-organisms. Fig. 23 shows the counting rates recorded by two OMs located on different storeys during the 2006-2008 runs. The average counting

rate increases from the bottom to shallower layers. The baseline is normally between 50 to 80 kHz.

Differently from the ^{40}K background, bioluminescence suffers from seasonal and annual variations, see Fig. 23. There can be large variations of the rate, reaching hundreds of kHz for some small periods. Since September 2006 the mean counting rate is 75% of the time below 100 kHz. A safeguard against bioluminescence burst is applied online by means of a high rate veto, most often set to 250 kHz.

The OMs deliver their data in real time and can be remotely controlled through a Gb Ethernet network. Every storey is equipped with a Local Control Module (LCM) which contains the electronic boards for the OM signal processing, the instrument readout, the acoustic positioning, the power system and the data transmission. Every five storeys the Master Local Control Module also contains an Ethernet switch board, which multiplexes the DAQ channels from the other storeys. At the bottom of each line, the Bottom String Socket is equipped with a String Control Module which contains local readout and DAQ electronics, as well as the power system for the whole line. Both the Master Local Control Modules and the String Control Modules include a Dense Wavelength Division Multiplexing system used for data transmission in order to merge several 1Gb/s Ethernet channels on the same pair of optical fibres, using different laser wavelengths. The lines are linked to the junction box by electro-optical cables which are connected using a unmanned submarine. A standard deep sea telecommunication cable links the junction box with a shore station where the data are filtered and recorded.

All OMs are continuously read out and digitized information ($hits$) sent to shore. A hit is a digitized PMT signal above the ARS threshold, set around 1/3 of the single photoelectron level (Level 0 hits, L0). On-shore, a dedicated computer farm performs a global selection of hits looking for interesting physics events (DataFilter). This on-shore handling of all raw data is the main challenge of the ANTARES DAQ system, because of the high background rates. The data output rate is from 0.3 GB/s to 1 GB/s, depending on background and on the number of active strings. A subset of L0 fulfilling particular conditions (Level 1 hits, L1) were defined for triggering purpose. This subset corresponds either to coincidences of L0 on the same triplet of OM of a storey hits within 20ns, or to a single high amplitude L0 (typically > 3 p.e.). The DataFilter processes all data online and looks for a physics event by searching a set of correlated L1 hits on the full detector on a $\sim 4\ \mu s$ window. In case an event is found, all L0 hits of the full detector during the time window are written on disk, otherwise the hits are thrown away.

The trigger rate is between 1 to 10 Hz, depending on the number of strings in data acquisition. Most of the triggered events are due to atmospheric muons, successively reconstructed by track-finding algorithms. If ANTARES receives external GRB alerts [180], all the activity of the detector is recorded for few minutes. In addition, untriggered data runs were collected on a weekly base. This untriggered data subset is used to monitor the relative PMT efficiencies, as well as to check the timing within a storey, using the ^{40}K activity.

10.1.2   Time and positioning calibration systems

Differently from the strings in ice, the ANTARES lines are flexible and move with the sea current, with displacements being a few metres at the top for a typical sea current of 5 cm/s. The reconstruction of the muon trajectory is based on the differences of the arrival times of the photons between OMs. ANTARES is expected to achieve an angular resolution of $< 0.3^o$ for muon events above 10 TeV, through timing measurements with precision of the order on the ns. This requires the knowledge of the OMs position with a precision of ~ 10

cm (light travels 22 cm per ns in water). Pointing accuracy thus is limited by: i) precision with which the spatial positioning and orientation of the OM is known; ii) accuracy with which the arrival time of photons at the OM is measured; iii) precision with which local timing of individual OM signals can be synchronized with respect to each other.

The positions of the OMs are measured on a real-time, typically once every few minutes, with a system of acoustic transponders and receivers on the lines and on the sea bed, together with tilt meters and compasses. The shape of each string is reconstructed by performing a global fit based on these information. Additional information needed for the line shape reconstruction are the water current flow and the sound velocity in sea water, which are measured using different equipments: an Acoustic Doppler Current Profiler; a Conductivity-Temperature-Depth sensors; a Sound Velocimeter.

Relative time resolution between OMs is limited by the transit time spread of the signal in the PMTs (about 1.3 ns) and by the scattering and chromatic dispersion of light in sea water (about 1.5 ns for a light propagation of 40 m). The electronics of the ANTARES detector is designed to contribute less than 0.5 ns to the overall time resolution.

Complementary time calibration systems are implemented to measure and monitor the relative times between different components of the detector within the ns level. These time calibrations are performed by:

i) the internal clock calibration system. It consists of a 20 MHz clock generator on shore, a clock distribution system and a clock signal transceiver board placed in each LCM. The system also includes the synchronisation with respect to Universal Time, by assigning the GPS timestamp to the data.

ii) The internal Optical Module LEDs: inside each OM there is a blue LED attached to the back of the PMT. These LEDs are used to measure the relative variation of the PMT transit time using data from dedicated runs.

iii) The Optical Beacons [181], which allows the relative time calibration of different OMs by means of independent and well controlled pulsed light sources distributed throughout the detector.

iv) Several thousands of down-going muon tracks are detected per day. The hit time residuals of the reconstructed muon tracks can be used to monitor the time offsets of the OM, enabling an overall space-time alignment and calibration cross-checks.

10.1.3   Measurement of atmospheric muons and atmospheric neutrinos

Atmospheric muons were an important tool to monitor the status of the detector and to check the reliability of the simulation tools and data taking. In ANTARES, two different Monte Carlo (MC) simulations are used to simulate atmospheric muons: one based on a full Corsika simulation [182], and another based on a parameterization of the underwater muon flux [183].

The full MC simulation [184] is based on Corsika v.6.2, with the QGSJET [185] package for the hadronic shower development. Muons are propagated to the detector using the MUSIC [186] code, which includes all relevant muon energy loss processes.

The second MC data set is generated using parametric formulas [57], obtained with a full MC tuned in order to reproduce the underground MACRO flux [187, 188], energy spectrum [189, 190] and distance between muons in bundle [191]. The characteristics of underwater muon events (flux, multiplicity, radial distance from the axis bundle, energy spectrum) are described with multi-parameters formulas in the range $1.5 \div 5.0$ km w.e. and up to $85°$ for the zenith angle. Starting from this parametrization, an event generator (called

MUPAGE) was developed [192] in the framework of the KM3NeT project [8] to generate underwater atmospheric muon bundles.

In both simulations, muons entering the surface of a virtual underwater cylinder (the *can*, which defines the limit inside which charged particles in MC codes produce Cherenkov photons [184]) are propagated using a GEANT-based program. Then, the background (extracted from real data) is added and the events are feed to a program which reproduces the DataFilter trigger logic. After this step, simulated data have the same format of the real ones.
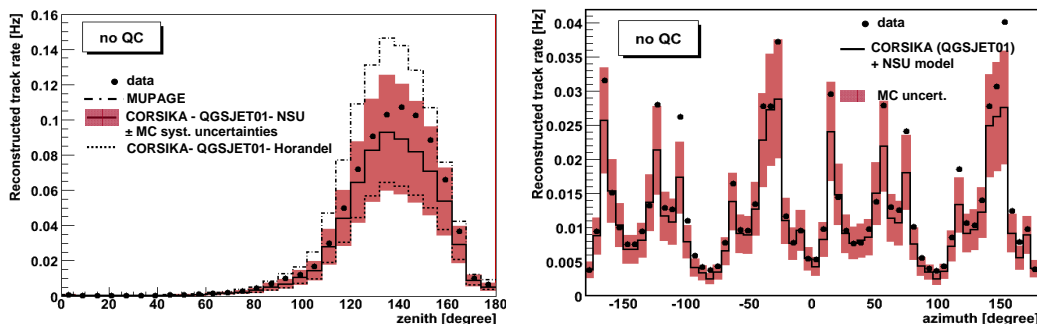
Figure 33: *(a) Zenith and (b) azimuth distributions of reconstructed tracks. Black points represent data. Lines refer to MC expectations, evaluated with two different simulation. The shadowed band represents the systematic error due to environmental and geometrical parameters.*

The main advantage of the full MC simulation (which is very large CPU time consuming) is the possibility of re-weighting the events according to any possible primary Cosmic Rays flux model. The main advantage of the MUPAGE simulation is that a large sample is produced with a relatively small amount of CPU time (much less than the time needed to simulate the Cherenkov light inside the *can*), and it is particularly suited for the simulation of the background for neutrino events.

Fig. 33 shows the zenith and azimuth distributions of reconstructed muon tracks. Black points represent experimental data. The solid [193] and the dotted [194] lines refer to Monte Carlo (MC) expectations obtained using the full MC simulation and two CR composition models. The dashed-dotted line refers to the fast simulation [192]. The shadowed band gives an estimate of the systematic errors, due to the uncertainties on the environmental parameters, like water absorption and scattering lengths in the ANTARES site, and on the geometrical characteristics of the detector. In particular, given the fact that OMs are pointing downwards, at an angle of 135° w.r.t. the vertical, knowledge of the OMs angular acceptance at these large angles is critical for an accurate determination of the muon flux.

A different analysis is necessary when selecting neutrinos. A set of more severe quality cuts must be applied in order to remove downward-going tracks wrongly reconstructed as upward. Data presented in Fig. 34 [183] were collected during the 10-12 line configuration period, from December 2007 to December 2008. Atmospheric neutrino events are simulated using the Bartol flux [58]. Only events detected at least by two lines and with at least 6 floors are considered. Restricting to the upward-going hemisphere (neutrino candidates) the
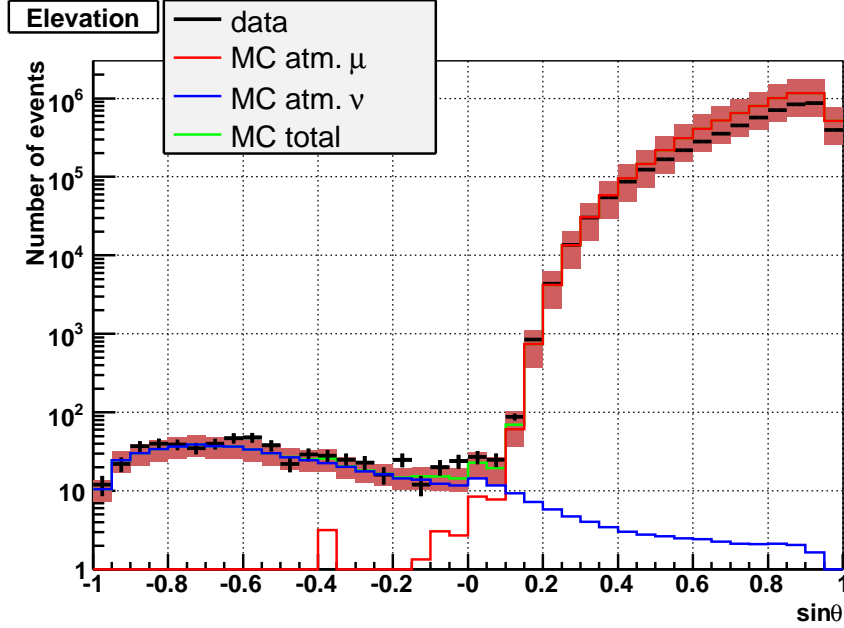
Figure 34: *Data (black crosses): 173 days of active time with 10 to 12 lines. Blue line: MC simulation of atmospheric neutrinos. Red line: atmospheric muons (Corsika+Horandel). 582 upward going events are found, to be compared to 494 expected from atmospheric neutrinos plus 13 from wrong reconstructed atmospheric muons.*

number of events are 3.4 per day for data, and 2.9 per day for simulations. The shadowed band represents the sum of theoretical and systematic uncertainties.

Upper flux limit from the direction of selected candidate sources were also evaluated using still more stringent criteria for the selection of upward-going muons [195]. The data with 5 lines were used and 140 active days. Even with less than half a detector, these limits are the best ones for experiments looking at the Southern hemisphere; they are shown as a function of the declination of the sources, and are compared with other experiments in Fig. 35.

The energy of the crossing muon or of secondary particles generated by neutrino interactions inside the instrumented volume is estimated from the amount of light deposited in the PMTs. Several estimators based on different techniques were developed [196]. MC studies show that this resolution is between $log_{10}(\sigma_E/E) = 0.2 \div 0.3$ for muons with energy above 1 TeV. The event energy measurement is a mandatory requirement for the study of the diffuse flux of high energy neutrinos. MC simulations indicate that after 3 years of data taking ANTARES can set an upper limit for diffuse fluxes of $E^2\Phi < 3.9 \times 10^{-8}$ GeV cm^{-2} s^{-1} sr^{-1} (see Fig. 18).
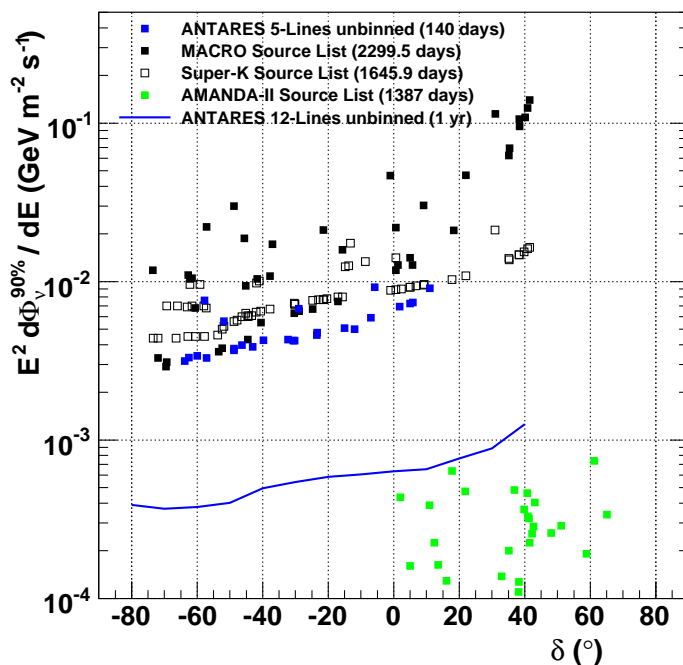
Figure 35: *Blue points: upper flux limit from the direction of selected candidate in the Southern sky for the ANTARES 5-line runs [195]. Results from MACRO [197] and SuperKamiokande [60] are also shown. Green points: upper flux limit from the direction of selected candidate in the Northern sky for AMANDA-II [160]. Full blue line: expected ANTARES sensitivity for 12 lines and one year of data taking using an unbinned method.*

10.2   NEMO

The NEutrino Mediterranean Observatory (NEMO) is a project [198, 199] of the Italian National Institute of Nuclear Physics (INFN). The activity has been mainly focused on the search and characterization of an optimal site for the detector installation; on the development of key technologies for the km^3 underwater telescope; on a feasibility study of the km^3 detector, which included the analysis of all construction and installation issues and optimization of the detector geometry by means of numerical simulations [200].

The validation of the proposed technologies via an advanced R&D activity, the prototyping of the proposed technical solutions and their relative validation in deep sea environment is carried out with two pilot projects NEMO Phase-1 and Phase-2.

Since 1998, the NEMO collaboration conducted more than 20 sea campaigns for the search and the characterization of an optimal site where to install an underwater neutrino telescope. A deep site with proper features in terms of depth and water optical properties has been identified at a depth of 3500 m about 80 km off-shore from Capo Passero (36° 16' N 16° 06' E), see §7.7.2 [201].

The main feature of a km^3 telescope is its modularity. The proposed NEMO basic element is the instrumented *NEMO-tower* (see Fig. 36): it is about 700 m high, and it is composed of 16 floors, 40 m spaced; each floor is rotated by 90°, with respect to the upper and lower adjacent ones, around the vertical axis of the tower. Each floor is equipped with

two OMs (one down-looking and one horizontally looking) at both extremities. In addiction to the OM, the tower hosts several environmental instruments plus the hydrophones for the acoustic positioning system. The tower structure is anchored at the sea bed and it is kept vertical by an appropriate buoyancy on the top.
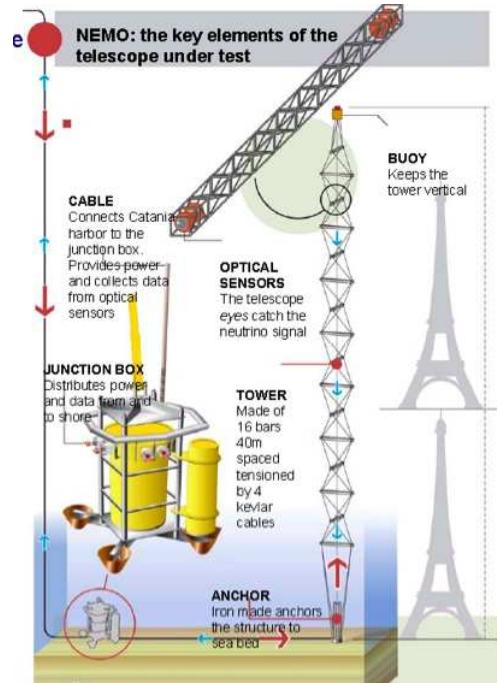

Figure 36: *The key-elements of the NEMO proposed version for the km^3 detector: the Junction Box, for power and data distribution, and the Tower with the bars and OM.*

The NEMO Phase-1 project allowed a first validation of the technological solutions proposed for the km^3 detector [199]. The apparatus included prototypes of all the critical elements: the Junction Box and a reduced version (one fourth) of the tower, called the *mini-tower*. On December 2006, both the Junction Box and the mini-tower were deployed and successfully activated at a test site at 2000 km depth near the Catania harbour. The underwater detector was connected to the shore station via a 28 km electro-optical cable.

The NEMO Phase-1 Junction Box was built following the concept of double containment. Pressure resistant steel vessels were hosted inside a large fiberglass container, which was filled with silicon oil to compensate the external pressure. This solution has the advantage of decoupling the two problems of pressure and corrosion resistance. The electronic components capable of withstanding high pressures were installed directly in the oil bath.

The mini-tower was equipped with sixteen 10" Hamamatsu R7081-SEL PMTs, mounted on 15 m long floors. The floors were spaced 40 m one from the other, with an additional spacing of 150 m from the base.

In addition to the OMs, the installed instrumentation included several sensors for calibrations and environmental monitoring (see Fig. 37, left). In particular two hydrophones were mounted on the tower base and at the extremities of each floor. These, together with
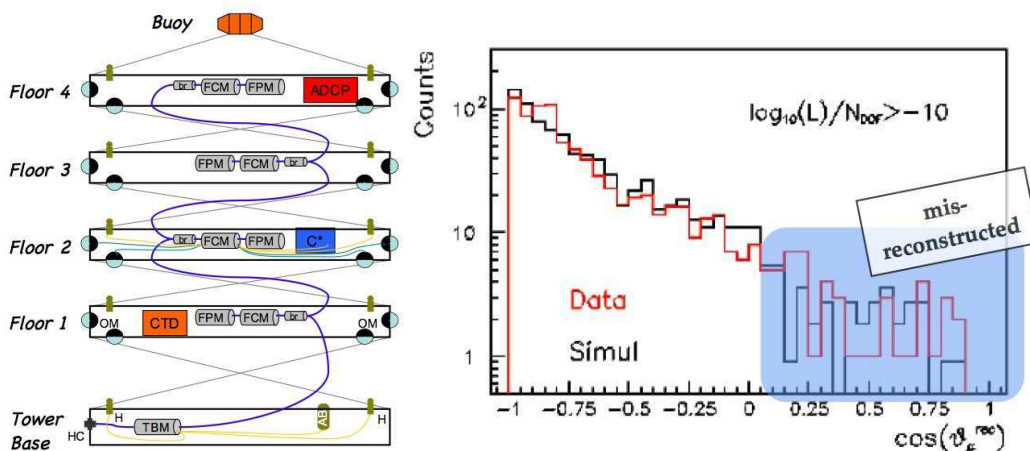
Figure 37: *Left: sketch of the Phase-1 mini-tower: the OMs on the floors and other environmental instruments: the Acoustic Doppler Current Profiler (ADCP), for profiling the sea current velocities; the C*, for measuring the water optical properties; the CTD, for salinity, temperature and density of water. Right: Distribution of the reconstructed events as a function of the cosine of the zenith angle, $\cos(\vartheta_\mu^{rec})$, compared with the MC [192]. There is an apparent excess of statistics both in measured and simulated events among upgoing events, i.e. with $\cos(\vartheta_\mu^{rec}) > 0$. This is explained taking into account that the mini-tower, because its small extension, have a poor angular resolution.*

acoustic beacons placed at the tower base and on the seabed, were used for the determination of the OM positions with a precision of about 10 cm. Moreover, a time calibration system was linked to the OMs through external optical fibres; those acted as flashers for measuring the offsets which bias the local time counters. The time offsets were determined with the precision of 1 ns, which fixed the highest time resolution for the acquired data.

One important technical choice of the design of the data acquisition system for NEMO Phase-1 is the scalability to a much bigger apparatus [202]. The electric signal from the PMTs was sampled with 2 Flash-ADC (100 MHz each) staggered by 5 ns, for a total 200 MHz sampling and a low power consumption. Each PMT generating an over threshold pulse (*hit*) was characterized by its time-stamp, total integrated charge and sampled signal waveform, the latter allowing an off-line reconstruction of the hit time with precision of ∼1 ns [203]. The hits from the four PMTs of each floor were continuously collected by the Floor Control Module (FCM) boards, converted into optical signals by an electro-optical tranceiver and sent to shore through one of the optical-fibre of the 28 km cable by using the Dense Wavelength Division Multiplex protocol. On shore, twin FCM boards de-multiplexed the incoming signal and distributed the data to the on-line trigger for a first raw selection of data. The trigger was based on hits coincidences occurred on near OMs within 20 ns and on large amplitude single hits. When a trigger seed was found, all hits occurred within a time window of ± 2 μs centered on the seed time were recorded.

A data analysis was done on a small sample of selected events, recorded during 23rd and 24th January 2007, corresponding to a livetime of 11.3 hours. From the analyzed data set,

2260 atmospheric muon events were reconstructed and their angular distribution measured [204]. The analysis showed good agreement between data and simulations (see Fig. 37, right).

The Phase-1 project provided a fundamental test of the technologies proposed for the realization and installation of the detector. Some problems occurred in Phase-1 after some months of functioning. Buoyancy of the tower decreased with the time (due to the construction process of the buoy), producing a lowering of the tower position. Another problem was related to a malfunction inside the JB that requires the recovery for a full diagnosis. The main results point out a malfunctioning of the optical penetrator. The Phase-2 was planned to validate the new solutions at the depths of the site of Capo Passero.

In July 2007, a 100 km Alcatel electro-optical cable was laid on the seabed linking the 3500 m deep sea site to shore. The cable is a 10 kV DC, along a single electrical conductor, allowing a power transport larger than 50 kW. The DC/DC converter, which converts the high voltage coming from shore into the 400 V required for the detector, is produced by Alcatel and it is currently under final tests. The data transmission is provided through 20 single mode optical fibres [205]. The shore station, located inside the harbour area of Portopalo di Capo Passero, was completed by the end of 2008 in an ancient *winery* building. A complete mechanical tower, a fully equipped NEMO mini-tower and a reduced version of an ANTARES string are planned to be installed on the Capo Passero Site by the end of 2009. Some features of the tower and mini-tower were modified according to the experience obtained from Phase-1: (*i*) floor length is reduced from 15 m to 12 m; (*ii*) higher simplification of the floor electric connections; (*iii*) new time-calibration flashers embedded directly into the OMs; (*iv*) new electronic components which allow a lower power consumption; (*v*) a new acoustic positioning system with special broad-band hydrophones capable of measuring the environmental acoustic background noise at 3500 m depth.

The cable and the shore station were proposed to the KM3Net consortium as well suited to host the Mediterranean km^3 detector.

10.3   NESTOR

The Neutrino Extended Submarine Telescope with Oceanographic Research (NESTOR) collaboration has developed an approach to operating a deepsea station, in the Southern Ionian Sea off the coast of Greece at depths exceeding 3500 m, permanently connected to shore by an insitu bidirectional cable, for multidisciplinary scientific research.

The basic element of the proposed NESTOR detector is a 32 m diameter hexagonal floor (*star*). A central casing supports a 1 m diameter spherical titanium pressure housing which contains the data acquisition electronics, power converters, monitoring, control and data transmission equipment. Attached to the central casing there are six arms built from titanium tubes to form a lightweight but rigid lattice girder structure. The arms can also be folded for transport and deployment. Two OMs are installed at the two end of each arm, one facing upwards and the other downwards: OMs are also installed above and below the central casing making a total of 14 units per floor. Using the OMs in pairs gives 4π coverage, enhancing discrimination between upward and downward going particles. In the NESTOR version, the tower will consist of 12 such floors, spaced vertically 20-30m (see Fig. 38, left).

In January 2002 a prototype was completed and deployed at a depth of 4100 m (project LAERTIS). The station transmitted the acquired data to shore from temperature and pressure sensors, compass, light attenuation meter, water current meter and an ocean bottom
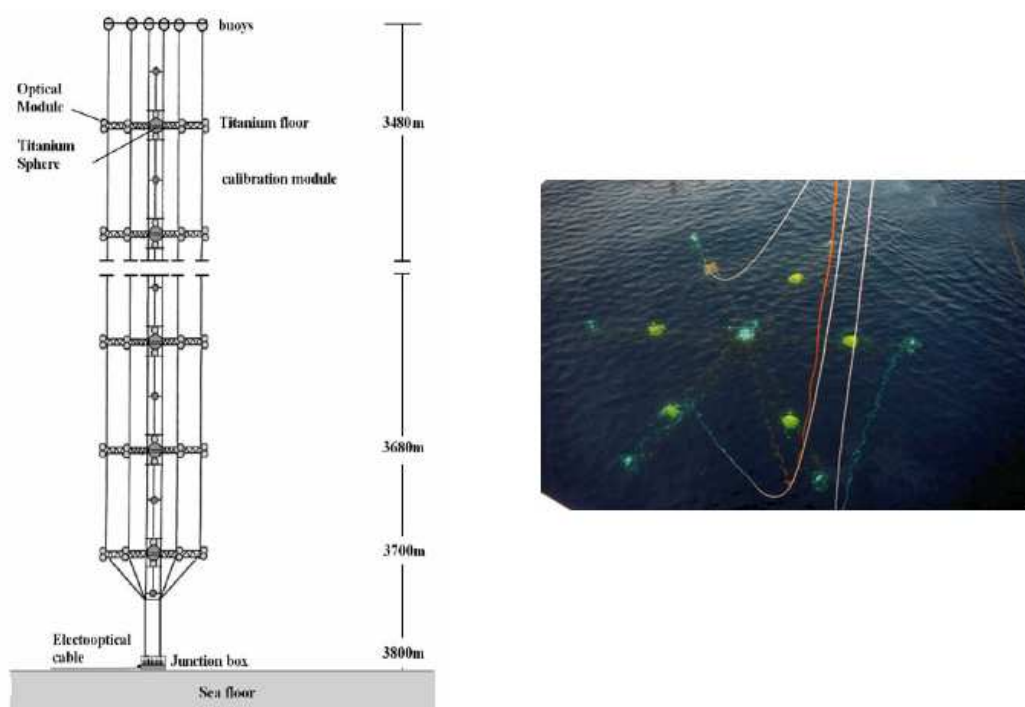
Figure 38: *Left: the proposed full NESTOR Detection Unit. Right: one floor of the NESTOR tower during its deployment for the first test in March 2003.*

seismometer. After a period of some months, the station was recovered.

In March 2003, the NESTOR collaboration successfully deployed a test floor of the detector tower, fully equipped with 12 OMs, final electronics and associated environmental sensors [206] (see Fig. 38, right). The detector continuously operated for more than a month. For about 1.1% of the total experimental time, bioluminescent activity was observed around the detector. This caused about 1% dead time. The prolonged period of running under stable operating conditions made it possible to measure the cosmic ray muon flux as a function of zenith angle and to derive the deep intensity relation [207].

11 The KM3NeT Consortium

KM3NeT is a future deep-sea research infrastructure hosting a neutrino telescope with a volume of at least one cubic kilometre to be constructed in the Mediterranean Sea. In February 2006, the Design Study for the infrastructure, funded by the EU FP6 framework, started. The KM3NeT research infrastructure has been singled out by ESFRI (the European Strategy Forum on Research Infrastructures) to be included in the European Roadmap for
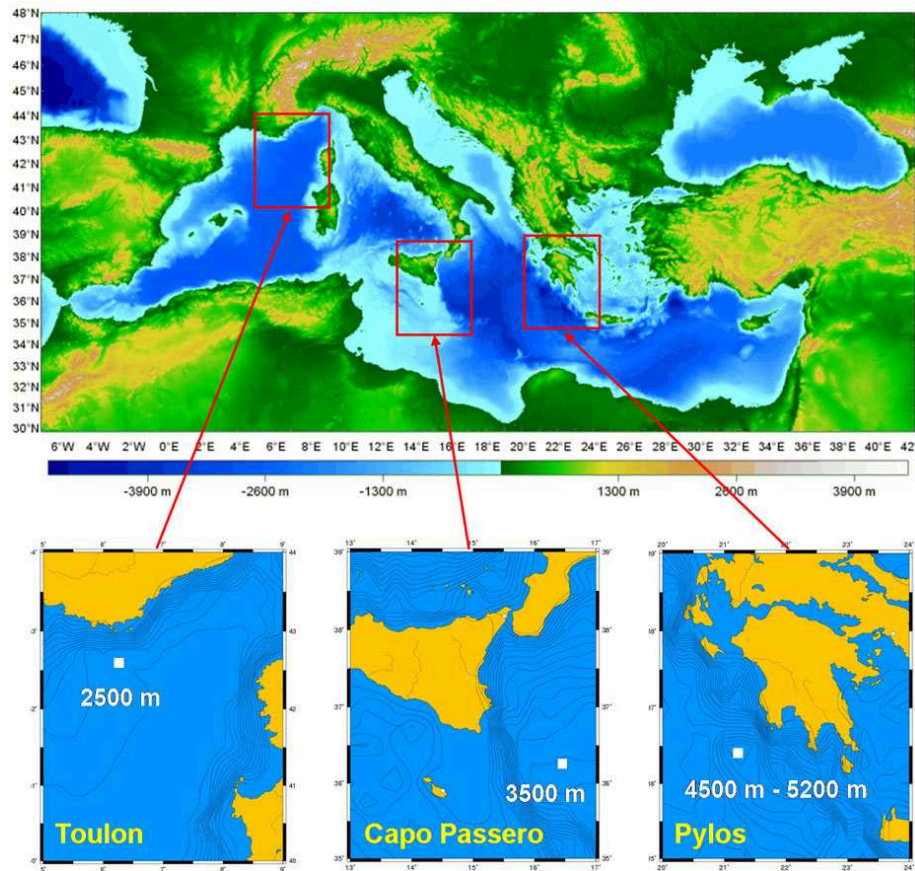
Figure 39: *The three candidate sites for the KM3Net telescope.*

Research Infrastructures. The primary objective of the Design Study is the development of a cost-effective design for a cubic-kilometre sized deep-sea infrastructure housing a neutrino telescope with unprecedented neutrino flux sensitivity at TeV energies and providing long-term access for deep-sea research. In April 2008 the Conceptual Design Report for the KM3NeT infrastructure was made public [50].

The Preparatory Phase of the infrastructure, funded by the EU FP7 framework, started in March 2008. The primary objective of the KM3NeT Preparatory Phase is to pave the way to political and scientific convergence on legal, governance, financial engineering and siting aspects of the infrastructure and to prepare rapid and efficient construction once it gets approved. Reconciliation of national and regional political and financial priorities with scientific and technological considerations will be a major issue, as has become apparent in the KM3NeT Design Study. The construction of the KM3NeT infrastructure is foreseen to start after the three year Preparatory Phase, which has been organised in work packages. Each work package has its own coordinator and executive committee.

Design, construction and operation of the KM3NeT neutrino telescope will be pursued by a consortium formed around the institutes currently involved in the ANTARES, NEMO and NESTOR pilot projects (see Fig. 39). Based on the leading expertise of these research
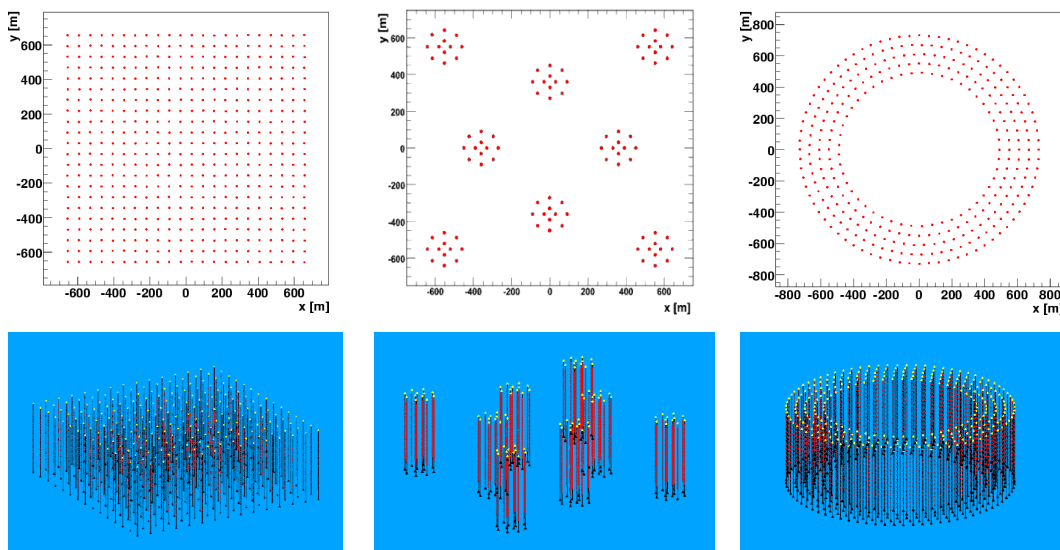
Figure 40: *Three geometry layouts for the KM3NeT detector: left, a squared grid; center, clustered Detection Units; right, ring configuration*

groups, the development of the KM3NeT telescope is envisaged to be achieved, after the Preparatory Phase, within a period of about four years for construction and deployment.

The KM3NeT facilities will provide support to scientific, long term and real-time measurements, also to a wide range of other *associated* earth and marine sciences, like oceanology, geophysics and marine biology.

The KM3Net detector is expected to exceed IceCube in sensitivity by a substantial factor, exploiting the superior optical properties of sea water as compared to the Antarctic ice and an increased overall PMT area. In Table 1, we summarize the required angular and energy resolution needed by the future KM3NeT detector, according to different types of astrophysical neutrino sources.

Source	E_ν range	channel	KM3NeT requisites
Steady point Source	$10 - 10^3$ TeV	$\nu_\mu N \to \mu X$	Angular res. $\sim 0.1°$
Transient point Source (e.g. GRBs)	$10 - 10^3$ TeV	$\nu_\mu N \to \mu X$	Angular res. $\sim 0.1°$ + time coincidence with a GRB Coordination Network
Diffuse Flux	$> 10^2$ TeV	$\nu_l N \to l X$ $\nu_l N \to \nu_l X$	Energy res.~ 0.3 in $\log E$

Table 1: *Target sources, neutrino energy range, interaction channels and resolution constraints for the KM3NeT telescope.*

The KM3NeT neutrino telescope will be composed of a number of vertical structures (detection units) which are anchored to the sea bed and usually kept vertical by one or sev-

eral buoys at their top. Since there is still a variety of viable design options, corresponding simulation studies are rather generic, concerning both assumed neutrino fluxes and detector properties. Fig. 40 shows three possible layouts: a squared grid of Detection Units (left), clustered (middle) and ring (right) configurations. Another configuration could consist of arranging the Detection Units in a homogeneous hexagon.
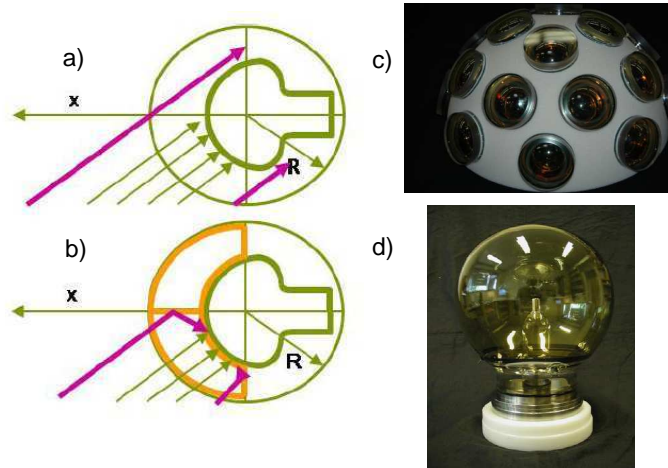

Figure 41: *The studied optical modules: (a) One single 10" PMT in a "benthos" sphere; (b) Multi-cathode PMT, with mirror separations to subdivide the PMT acceptance; (c) Multi-PMT optical module made by 20 PMTs, 3" each; (d) Spherical geometry X-HPD (8" prototype).*

Each detection unit will carry the photo-sensor and possibly further devices for calibration and environmental measurements on mechanical structures which can be like ANTARES *storeys*, NEMO's *floors* or NESTOR's *stars*. Such structure will support the necessary sensors, supply interfaces, data lines and electronic components where applicable. The basic photo-sensor unit remains the Optical Module (OM) [209, 210], which can host one or several PMTs, their high-voltage bases and their interfaces to an acquisition system of nanosecond-precision data.

Whereas all of the current neutrino telescope projects use OMs composed of a single large (tipically 10") standard PMT per OM, alternative solutions are also under investigation for KM3NeT. In addition to the *classical* solution described above (see Fig. 41, case a), various tests with multi-cathode PMTs (see Fig. 41, case b), multi-PMT OMs (see Fig. 41, case c), and large spherical hybrid PMTs (see Fig. 41 case d) [208] are performed together with computer simulation for studying the telescope response accordingly.

The data transport devices and power harness of each Detection Unit is planned to be connected via the anchor to a deep-sea cable network. This network can contain one or more junction boxes and one or several electro-optical cables to shore. It also provides power and slow-control communication to the detector. On shore, a station equipped with appropriate computing power is required for collecting the data, applying online filter algorithms and transmitting the data to mass storage devices (see Fig. 42 where the trigger and DAQ system is sketched).

The deployment of the Detection Units on the sea bed and their maintenance along

the years of the telescope live time require the development of appropriate machines and infrastructures. For Detection Units deployment, the NESTOR Institute has developed a central-well, ballasted platform called *Delta Berenike*. For completing the detector construction (junctions between meatable underwater connectors) ad maintenance down in the deep-site, underwater robotic devices will be necessary. These devices are either remotely operated underwater vehicles or autonomous underwater vehicles.
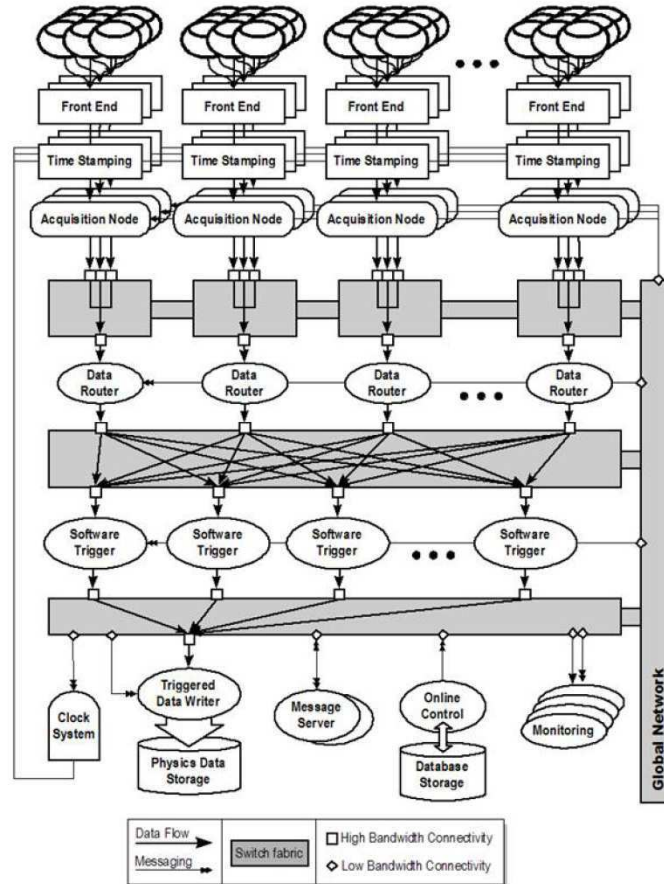

Figure 42: *The Trigger and Data Acquisition System (TRIDAS) for the KM3NeT project.*

12   Conclusion

The next years will be decisive for neutrino astronomy. While a large neutrino telescope is in an advanced stage of construction under the South Pole ice (the IceCube experiment), the technological challenges to build a neutrino telescope in deep sea have been surmounted by experiments like ANTARES, NEMO and NESTOR, which have motivated the approval

of the design study of the kilometre-scale version in the Mediterranean sea (the KM3NeT consortium). These new generation of neutrino telescope experiments will achieve effective volumes which will be able to explore the Northern sky (the IcuCube experiment in the South Pole) and the Southern sky (the underwater Mediterranean experiment) in a way never seen before.

High energy astrophysical neutrinos have not been observed so far; their flux can only be evaluated using models. The hunt for the first high energy neutrino of cosmic origin has started.

References

[1] M.A. Markov, Proceedings Int. Conf. on High Energy Physics, p. 183, Univ. of Rochester (1960).

[2] P. Bosetti et al. (DUMAND collaboration). Astrop.Phys. 7 (1997) 263.

[3] V. Aynutdinov et al. (the Baikal Collaboration) *The Baikal neutrino experiment: Status, selected physics results, and perspectives*, Nucl. Instrum. Meth. A588 (2008) 99-106.

[4] E. Andres et al. (the AMANDA Collaboration). *Observation of high-energy neutrinos using Cherenkov detectors embedded deep in Antarctic ice*, Nature 410,(2001) 441.

[5] J.A. Aguilar et al. (ANTARES Collaboration). Astrop. Phys. 26 (2006) 314.

[6] P. Piattelli (NEMO collaboration). Nucl.Phys.Proc.Suppl. 143 (2005) 359.

[7] G. Aggouras et al. (NESTOR collaboration). Astrop. Phys. 23 (2005) 377.

[8] http://www.km3net.org

[9] A. M. Hillas *Recent progress and some current questions*. astro-ph/0607109. The figure is due to T. Gaisser.

[10] P.L. Biermann, T. K. Gaisser , T Stanev. *Origin of galactic cosmic rays* Phys. Rev. D 51 (1995) 3450 - 3454

[11] T. K. Gaisser.*Cosmic Rays and Particle Physics*, Cambridge University Press, 1990. ISBN 0521326672

[12] P. K. F. Grieder. *Cosmic Rays at Earth: Researcher's Reference Manual and Data Book* Elsevier, 2001. ISBN 0444507108

[13] E. Fermi. *On the origin of cosmic rays*. Phys. Rev. 75(1949) 1169.

[14] E. Fermi. *Galactic magnetic fields and the origin of cosmic radiation*. Astrophys. J. 119 (1954) 16.

[15] V. L. Ginzburg and V. S. Ptuskin. *On the origin of cosmic rays: Some problems in high-energy astrophysics*. Rev. Mod. Phys. 48 (1976) 161.

[16] A. M. Hillas. *Can diffusive shock acceleration in supernova remnants account for high-energy galactic cosmic rays* J. Phys. G: Nucl. Part. Phys. 31 (2005) 39.

[17] E. G. Berezhko and L. T. Ksenofontov. *Composition of cosmic rays accelerated in supernova remnants*. JETP 89 (1999) 391.

[18] V.L. Ginzburg, Y.M. Khazan and V.S. Ptuskin. Astrophysics and Space Science 68 (1980) 295.

[19] J. R. Horandel. *Models of the knee in the energy spectrum of cosmic rays*. Astrop. Phys. 21 (2004) 241265.

[20] D. Kazanas and A. Nicolaidis. In Proceedings of the 27th International Cosmic Ray Conference, Hamburg, Germany, 2001. astro-ph/0103147.

[21] T. Antoni et al. *Electron, muon, and hadron lateral distributions measured in air-showers by the KASCADE experiment*. Astrop. Phys., 14 (2001) 245260.

[22] F. Halzen et al. *The highest energy cosmic ray*. Astrop. Phys., 3 (1995) 151.

[23] B. Peters. *Primary cosmic radiation and extensive air showers*. Nuovo Cimento, 22 (1961) 800.

[24] P. Sokolsky. *Introduction to Ultrahigh Energy Cosmic Ray Physics*, Westview Press Advanced Book Program, 2004.

[25] M. Ostrowski. *Mechanisms and sites of ultra high energy cosmic ray origin*, Astrop. Phys. 18 (2002) 229-236.

[26] K. Greisen. *End to the cosmic ray spectrum*, Phys. Rev. Lett. 16 (1966) 748.

[27] G. T. Zatsepin and V. A. Kuzmin. *Upper limit of the spectrum of cosmic rays*. Sov. Phys. JETP Lett. 4 (1966) 78.

[28] M. Takeda et al.. *Extension of the cosmic ray energy spectrum beyond the predicted Greisen-Zatsepin-Kuz'min cutoff*, Phys. Rev. 81 (1998) 1163.

[29] T. Abu-Zayyad et al. (HiRes Collaboration). *Measurement of the flux of ultrahigh energy cosmic rays from monocular observations by the high resolution Fly's Eye experiment*, Phys. Rev. Lett. 92 (2004) 151101.

[30] W.-M.Yao et al. (Particle Data Group), J. Phys. G 33, 1 (2006) and 2007 partial update for the 2008 edition.

[31] See the web site of the Pierre Auger observatory: http://www.auger.org/

[32] The Pierre Auger Collaboration: *Upper limit on the cosmic-ray photon flux above 10^{19} eV using the surface detector of the Pierre Auger Observatory* Astrop. Phys. 29 (2008) 243-256, arXiv:0712.1147.

[33] J. Abraham et al. *Correlation of the highest-energy cosmic rays with nearby extra-galactic objects*. Science, 318:938943, 2007.

[34] V. Berezinsky et al., *Astrophysics of Cosmic Rays*, North-Holland, Amsterdam (1990).

[35] F. Halzen and D. Hooper, *High-energy neutrino astronomy: The Cosmic ray connection*, Rept. Prog. Phys. 65 (2002) 1025-1078.

[36] A. de Angelis et al., *Very-high-energy gamma astrophysics*, Riv. Nuovo Cimento 31 (2008) 187.

[37] F. Aharonian et al., *High energy astrophysics with ground-based gamma ray detectors*, Rep. Prog. Phys. 71 (2008) 096901.

[38] F. A. Aharonian. *Very High Energy Cosmic Gamma-Ray Radiation*. World Scientific Publishing, 2004.

[39] C. Stegmann , A. Kappes, J. Hinton and F. Aharonian. *Potential neutrino signals in a northern hemisphere neutrino telescope from galactic gamma-ray sources*, Astrophysics and Space Science 309 (2007) 429.

[40] C. E. Fichtel and J. I. Trombka. *Gamma-ray astrophysics: New insight into the Universe*. Technical report, 1997. NASA-RP-1386.

[41] http://cossc.gsfc.nasa.gov/docs/cgro/cossc/egret/3rd_EGRET_Cat.html

[42] N. Gehrels and P. Michelson. *GLAST: The next-generation high energy gamma ray astronomy mission*. Astrop. Phys. 11 (1999) 277282.

[43] A. Abdo et al. (Fermi LAT Coll.) *Fermi Large Area Telescope Bright gamma-rays source list* arXiv:0902.1340 [astro-ph.HE]

[44] T. C. Weekes et al., *Observation of TeV gamma rays from the Crab nebula using the atmospheric Cherenkov imaging technique*. Astrophys. J. 342 (1989) 379395.

[45] R. Mirzoyan et al., *The first telescope of the HEGRA air Cherenkov imaging telescope array*. Nucl. Instr. and Meth. Phys. Res. A 351 (1994) 513526.

[46] J. Holder et al. In Proceedings of the 29th International Cosmic Ray Conference, Pune, India, 2005. astro-ph/0507451.

[47] R. Enomoto et al., *Design study of CANGAROO-III, stereoscopic imaging atmospheric Cherenkov telescopes for sub-TeV gamma-ray*. Astrop. Phys. 16 (2002) 235244.

[48] J. A. Hinton. *The status of the HESS project*. New Astron. Rev. 48 (2004) 331337.

[49] J. Albert et al., *Physics and Astrophysics with a ground-based gamma-ray telescope of low energy threshold*. Astroparticle Physics 23 (2005) 493-509.

[50] KM3neT: Conceptual Design Report. http://www.km3net.org/CDR/CDR-KM3NeT.pdf

[51] F. Aharonian et al. (HEGRA Collaboration). Astrophys. J. 614 (2004) 897.

[52] A. Achterberg, Y.A. Gallant, J.G. Kirk, A.W.Guthmann, MNRAS 393A (2001) 328.

[53] T.C. Weekes. et al., Astrophys. J. 342 (1989) 379.

[54] F. Ahronian et al., (The HESS Coll.), *Observations of the Crab Nebula with H.E.S.S.*, Astron. Astrophys. 457 (2006) 899-915.

[55] M. D. Kistler and J. F. Beacom. *Guaranteed and prospective galactic TeV neutrino sources*. Phys. Rev. D 74 (2006) 063007. astro-ph/0607082.

[56] Franck Bernard *Caractrisation des performances d'un tlescope sous-marin neutrinos pour la dtection de cascades contenues dans le cadre du projet ANTARES*. PhD thesis Universit de la Mditerrane, Aix-Marseille II, Marseille, France (2000).

[57] Y. Becherini, A. Margiotta, M. Sioli and M. Spurio. Astrop. Phys. 25(2006) 1.

[58] V. Agrawal, T.K. Gaisser, P. Lipari, T. Stanev. Phys. Rev. D53 (1996) 1314.

[59] M. Ambrosio et al. *Neutrino astronomy with the MACRO detector*. Astrophys. J., 546 (2001) 10381054.

[60] K. Abe et al. *High energy neutrino astronomy using upward-going muons in Super-Kamiokande-I*. Astrophys. J., 652 (2006) 198205.

[61] M. Crouch, in Proc. 20th Int. Cosmic Ray Conf., Moscow, 6 (1987) 165 .

[62] Yu.M. Andreev, V.I. Gurentzov, and I.M. Kogai, in Proc. 20th Int. Cosmic Ray Conf., Moscow, 6, 200 (1987).

[63] M. Aglietta et al., (LVD Collaboration), Astrop. Phys. 3 (1995) 311 .

[64] M. Ambrosio et al., (MACRO Collaboration), Phys. Rev. D52 (1995) 3793 .

[65] Ch. Berger et al., (Frejus Collaboration), Phys. Rev. D40 (1989) 2163 .

[66] C. Waltham et al., in Proc. 27th Int. Cosmic Ray Conf., Hamburg (2001) 991 .

[67] R. Gandhi et al., Astrop. Phys. 5 (1996) 81.

[68] J. Pumplin et al. *New generation of parton distributions with uncertainties from global QCD analysis*. JHEP, 07 (2002) 012. hep-ph/0201195.

[69] P. Lipari and T. Stanev. *Propagation of multi-TeV muons*. Phys. Rev. D 44 (1991) 3543.

[70] P. A. Cherenkov. Phys. Rev. 52 (1937) 378 .

[71] T. K. Gaisser, F. Halzen and T. Stanev, Phys. Rep. 258 (1995) 173-236; Erratum-ibid. 271 (1996) 355-356, arXiv:hep-ph/9410384v1.

[72] D. J. L. Bailey. *Monte Carlo tools and analysis methods of understanding the ANTARES experiment and predicting its sensitivity to Dark Matter*. PhD thesis, University of Oxford, United Kingdom, 2002.

[73] F. Aharonian et al. *Detection of TeV gamma-ray emission from the shell-type super-nova remnant RX J0852.0-4622 with HESS*, Astron. & Astrophys., 437:L7 (2005). astro-ph/0505380.

[74] O. Reimer and M. Pohl. *No hadronic TeV gamma-rays from SNR RX J1713.7-3946*. Astron. & Astrophys., 390:L43 (2002).

[75] H. Muraishi et al. *Evidence for TeV gamma-ray emission from the shell-type SNR RX J1713.7-3946*. Astron. & Astrophys., 354:L57 (2000).

[76] R. Enomoto et al. *The acceleration of cosmic-ray protons in the supernova remnant RX J1713.7-3946*. Nature, 416 (2002)823. Astron. & Astrophys., 449 (2006) 223.

[77] J. Alvarez-Muniz and F. Halzen. *Possible high-energy neutrinos from the cosmic accelerator RXJ1713.7-3946*. Astrophys. J., 576:L33 (2002). astro-ph/0205408.

[78] M. L. Costantini and F. Vissani. *Expected neutrino signal from supernova remnant RXJ1713.7-3946 and flavor oscillations*. Astrop. Phys. 23 (2005) 477485.

[79] F. Aharonian et al. (HESS Collaboration). *A detailed spectral and morphological study of the gamma-ray supernova remnant RX J1713.7-3946 with HESS* Astron.& Astrophys. 449 (2006) 223-242.

[80] D. Horns, F. Aharonian, A. Santangelo, A. I. D. Hoffmann, and C. Masterson. *Nucleonic gamma-ray production in Vela X*. Astron. & Astrophys., 451 (2006) 51.

[81] D. Guetta and E. Amato. *Neutrino flux predictions for galactic plerions*. Astrop. Phys. 19 (2003) 403. astro-ph/0209537.

[82] F. Aharonian et al. (HESS Collaboration). *Very high energy gamma rays from the direction of Sagittarius A**. Astron. & Astrophys., 425:L1317, 2004.

[83] F. Aharonian et al. (HESS Collaboration). *Very high energy gamma rays from the composite SNR G0.9+0.1*. Astron. & Astrophys., 432:L2529, 2005.

[84] F. Aharonian et al. (HESS Collaboration). *Discovery of very high energy gamma-rays from the galactic centre ridge*. Nature, 439 (2006) 695. astro-ph/0603021.

[85] S. Chaty. In Proceedings of Rencontres de Moriond, Very High Energy Phenomena in the Universe, La Thuile, Italy, 2005. astro-ph/0506008.

[86] S. Migliari, R. Fender, and M. Mendez. *Iron emission lines from extended X-ray jets in SS 433: Reheating of atomic nuclei*. Science, 297 (2002) 1673.

[87] J. Albert et al. (MAGIC Collaboration). *Variable very high energy gamma-ray emission from the microquasar LS I+61 303*. Science, 312 (2006) 1771. astro-ph/0605549.

[88] F. Aharonian et al. (HESS Collaboration). *Discovery of very high energy gamma rays associated with an X-ray binary*. Science, 309 (2005) 746.

[89] D. F. Torres and F. Halzen. *LS I+61 303 as a potential neutrino source on the light of MAGIC results*. astro-ph/0607368.

[90] F. Aharonian, L. Anchordoqui, D. Khangulyan, and T. Montaruli. *Microquasar LS 5039: a TeV gamma-ray emitter and a potential TeV neutrino source*. J. Phys. Conf. Ser., 39:408.

[91] S. Aiello et al. (The NEMO Collaboration), *Sensitivity of an underwater Cherenkov km^3 telescope to TeV neutrinos from Galactic microquasars*, Astrop. Phys. 28(2007) 1-9 .

[92] R. Atkins et al. (MILAGRO collaboration). Phys. Rev. Lett. 95 (2005) 251103.

[93] W. Bednarek, G. F. Burgio, and T. Montaruli. *Galactic discrete sources of high energy neutrinos*. New Astron. Rev., 49 (2005) 1. astro-ph/0404534.

[94] G. D'Ali Staiti, *The ARGO-YBJ experiment in Tibet*. Nucl. Instr. Meth. A588 (2008) 7. See also: http://argo.na.infn.it/

[95] MILAGRO project, http://www.lanl.gov/milagro

[96] Slate: http://www.slate.com/id/2081042/

[97] R. Engel, D. Seckel, and T. Stanev. *Neutrinos from propagation of ultra-high energy protons*. Phys. Rev. D, 64 (2001) 093010. astro-ph/0101216, and references therein.

[98] E. Waxman. *Extra galactic sources of high energy neutrinos*. Phys. Scripta, T121(2005) 147. astro-ph/0502159.

[99] F. Halzen, A. O'Murchadha; *Neutrinos from Auger sources* arXiv astro-ph 0802.0887

[100] R. V. E. Lovelace. *Dynamo model of double radio sources*. Nature, 262 (1976) 649.

[101] K. Mannheim. *High-energy neutrinos from extragalactic jets*. Astrop. Phys., 3 (1995) 295.

[102] F. Halzen and E. Zas. *Neutrino fluxes from active galaxies: A model independent estimate*. Astrophys. J., 488 (1997) 669.

[103] R. J. Protheroe. *High energy neutrinos from blazars*. ASP Conf. Ser., 121 (1997) 585.

[104] A. Achterberg et al. (IceCube Coll.), *Multiyear search for a diffuse flux of muon neutrinos with AMANDA II*. Physical Review D, 76 (2007) 042008.

[105] J. K. Becker, P. L. Biermann, and W. Rhode. *The diffuse neutrino flux from FR-II radio galaxies and blazars: A source property based estimate*. Astrop. Phys. 23 (2005) 355368. astro-ph/0502089.

[106] F. Aharonian et al. (H.E.S.S. collaboration). Nature 440 (2006) 1018.

[107] R. White, Proc. 30th International Cosmic Ray Conference, Merida, 2007.

[108] W. Benbow et al. (H.E.S.S. collaboration). Proc. 30th International Cosmic Ray Conference, Merida, 2007.

[109] T. J. Galama et al. *Discovery of the peculiar supernova 1998bw in the error box of GRB980425*. Nature, 395 (1998) 670.

[110] K. Z. Stanek et al. *Spectroscopic discovery of the supernova 2003dh associated with GRB030329*. Astrophys. J. 591:L17, 2003.

[111] J. Hjorth et al. *A very energetic supernova associated with the gamma-ray burst of 29 March 2003*. Nature, 423 (2003) 847.

[112] http://heasarc.gsfc.nasa.gov/docs/sax/sax.html

[113] E. Waxman and J. N. Bahcall. *High energy neutrinos from cosmological gamma-ray burst fireballs*. Phys. Rev. Lett. 78 (1997) 2292.

[114] D. Guetta et al. *Neutrinos from individual gamma-ray bursts in the BATSE catalog*. Astrop. Phys., 20 (2004) 429. astro-ph/0302524.

[115] J.A. Aguilar et al. (The ANTARES Coll.). *The data acquisition system for the ANTARES neutrino telescope*. Nucl. Instr. Meth. A570 (2007) 107 .

[116] H. Dannerbauer et al. *Follow-up near-infrared spectroscopy of ultraluminous infrared galaxies observed by ISO*. Astron. & Astrophys., 441 (2005) 999.

[117] V. Springel et al. *Modeling feedback from stars and black holes in galaxy mergers*. Astron. Soc., 361 (2005) 776.

[118] A. Loeb and E. Waxman. *The cumulative background of high-energy neutrinos from starburst galaxies*. JCAP, 0605 (2006) 003. astro-ph/0601695.

[119] P. Sreekumar et al. (EGRET Collaboration), Ap. J. 494 (2000) 523.

[120] E. Waxman and J. Bahcall. Phys. Rev. D59 (1998) 023002-1; J. Bahcall, E. Waxman. Phys. Rev. D64(2001) 023002-1 .

[121] K. Mannheim, R. J. Protheroe, J. P. Rachen, *Cosmic ray bound for models of extragalactic neutrino production*, Phys. Rev. D 63 (2000) 023003.

[122] W. Rhode et al. (Frejus Collaboration), Astrop. Phys. 4 (1996) 217 .

[123] M. Ambrosio et al. (MACRO Collaboration), Astrop. Phys. 19 (2003) 1.

[124] V. Aynutdinov et al. *Search for a Diffuse Flux of High-Energy Extraterrestrial Neutrinos with the NT200 Neutrino Telescope*. Astrop. Phys. 25 (2006) 140-150. astro-ph/0508675.

[125] M. Ackermann et al. (AMANDA Collaboration), Ap. J- 675 (2008) 1014.

[126] G. Fiorentini, A. Naumov, F.L. Villante. Phys. Lett. B510 (2001) 173

[127] C. Giunti. *Neutrino Flavor States and the Quantum Theory of Neutrino Oscillations*. J. Phys. G: Nucl. Part. Phys. 34 (2007) R93-R109, arXiv:hep-ph/0608070. See also the very interesting and exhaustive web page on neutrinos: http://www.nu.to.infn.it/

[128] J. G. Learned and S. Pakvasa. *Detecting nutau oscillations as PeV energies*. Astrop. Phys., 3 (1995) 267.

[129] M. Ackermann et al. *Optical properties of deep glacial ice at the South Pole*. J. Geophys. Res. 111(D13) (2006) 1-4.

[130] Y. He and P. Price. *Remote sensing of dust in deep ice at the South Pole*. Journal of Geophysical Research, 103(D14) (1998) 1704117056.

[131] Y. R. Whitehead. *On the Properties of Ice at the IceCube Neutrino Telescope*. Master of Science thesis, University of Canterbury, Christchurch, New Zealand, 2008. http://www.icecube.wisc.edu/science/

[132] http://www.wetlabs.com

[133] C.D. Mobley, *Light and Water*, Academic Press, San Diego, 1994.

[134] R.M. Pope, E.S. Fry, Appl. Opt. 36 (1997) 33.

[135] L. Kou, D. Labriel, P. Chylek, Appl. Opt. 32 (1993) 3531.

[136] G. Riccobene et al. Astroparticle Physics 27 (2007) 1-9.

[137] R.C. Smith, K.S. Baker, Appl. Opt. 20 (1981) 177.

[138] Henning, P.J., *Bioluminescence in action*, Academic Press, London, 1978.

[139] M. Circella, *The construction of ANTARES, the first undersea neutrino telescope*. Nucl. Instrum Meth. A602 (2009) 1-6.

[140] Widder, E.A., Latz, I.M. and Case, J.F. Biol. Bull. 165 (1983) 791.

[141] Gillibrand et al., Marine Ecology Progress, Series 341 (2007) 37.

[142] I.G. Priede et al. submitted to Deep Sea Research.

[143] J. Dumm, H. Landsman for the IceCube Collaboration: *IceCube - First Results*. Journal of Physics: Conference Series 60 (2007) 334336.

[144] J. Ahrens et al. (the AMANDA Collaboration). *Muon track reconstruction and data selection techniques in AMANDA*, Nucl. Instrum. Meth. A524 (2004) 169-194.

[145] J. Lundberg et al. *Light tracking through ice and water Scattering and absorption in heterogenous media with PHOTONICS*. Nucl. Instrum. and Meth. A581 (2007) 619-631.

[146] A. Heijboer. *Track reconstruction and point source searches with Antares*. June 2004, Universiteit van Amsterdam, Amsterdam, The Netherlands. http://antares.in2p3.fr/Publications/index.html

[147] G. Carminati, A. Margiotta, M. Spurio. *MUons from Parametric formulas: A fast Generator of atmospheric μ-bundles for neutrino telescopes(MUPAGE)*. Nucl. Instr. Methods A602 (2009) 95.

[148] http://www.phys.hawaii.edu/dmnd/dumand.html

[149] A. Roberts, Rev. Mod. Phys. 64 (1992) 259.

[150] J. Babson et al. (The DUMAND Coll.). *Cosmic-ray muons in the deep ocean*. Phys. Rev. D42 (1990) 3613.

[151] http://baikalweb.jinr.ru/

[152] L. Kuzmichev (for the Baikal Collaboration). *The Baikal neutrino experiment: from NT200 to NT200+*, ICRC 2005.

[153] S. R. Klein. *IceCube: A Cubic Kilometer Radiation Detector*. arXiv:0807.0034v2 [physics.ins-det]

[154] J.Ahrens et al. (IceCube Collaboration). *IceCube preliminary design document*. http://icecube.wisc.edu

[155] T. Gaisser et al. (IceCube Collaboration), ICRC 2007 proc., Merida. arXiv:0711.0353

[156] C. Portello-Roucelle. *High Energy Neutrinos from the Cold: Status and Prospects of the Icecube Experiment*. arXiv:0805.3546 [astro-ph]

[157] http://www.icecube.wisc.edu/science/

[158] A. Achterberg et al. (AMANDA Collaboration). *First year performance of the Ice-Cube neutrino telescope*. Astrop. Phys. 26 (2006) 155-173.

[159] F. Halzen, J.E. Jacobsen, E. Zas. Phys.Rev. D53 (1996) 7359-7361, arXiv:astro-ph/9512080v1

[160] A. Achterberg et al. (IceCube Collaboration), Phys. Rev. D75 (2007)102001. arXiv:astro-ph/0611063.

[161] A.Achterberg et al, (IceCube collaboration), Phys. Rev. D 76 (2007) 027101.

[162] J.L. Bazo Alba. *Search for neutrino point sources with IceCube 22-strings*. arXiv:0811.4110v1 [astro-ph]

[163] J. Braun et al., APh. 29 (2008) 299.

[164] C. Finnley, J. Dumm and T. Montaruli for the IceCube Collaboration. ICRC2007 proc., Merida. arXiv:0711.0353

[165] K. Hoshina, J. Hodges, G. C. Hill for the IceCube Collaboration. ICRC2007 proc., Merida. arXiv:0711.0353

[166] A. Achterberg et al. (AMANDA Collaboration), Astrop. Phys. 26 (2006) 129 .

[167] M. Ackermann et al. [AMANDA Collaboration], Astrop. Phys. 24 (2006) 459. arXiv:astroph/0508518.

[168] J. Alvarez-Muñiz, F. Halzen, Astrophys. J. 576 (2002), arXiv:astro-ph/0205408v3

[169] H. Landsmann et al. (IceCube collaboration). ICRC2007 proc., Merida,arXiv:0711.0353

[170] S. Boser et al. (IceCube Collaboration). ICRC2007 proc., Merida, arXiv:0711.0353

[171] For more information and for a complete list of the ANTARES members see: http://antares.in2p3.fr

[172] P. Amram et al., Astropart, Phys. 13 (2000) 127.

[173] J. A. Aguilar et al. Astropart, Phys. 23 (2005) 131.

[174] P. Amram et al., Astropart, Phys. 19 (2003) 253.

[175] P. Amram et al., Nucl. Instr. Meth. A484 (2002) 369.

[176] M. Ageron et al.. Nucl. Instrum. Meth. A581 (2007) 695.

[177] M. Ageron et al. (ANTARES Collaration), *Performance of the First ANTARES Detector Line*. arXiv:0812.2095 [astro-ph]. Submitted to APP

[178] J. A. Aguilar et al. Astropart, Phys. 23 (2005) 131.

[179] J.A. Aguilar et al., Nucl. Instr. Meth. A555 (2005) 132.

[180] J.A. Aguilar et al., Nucl. Instr. Meth. A570 (2007) 107.

[181] M. Ageron et al., Nucl. Instr. Meth. A578 (2007) 498 .

[182] A. Margiotta (ANTARES Collaboration): *Systematic uncertainties in MonteCarlo simulations of the atmospheric muon flux in the 5-line ANTARES detector*. Nucl. Instrum. Meth. A602 (2009) 76. arXiv:0809.0268 [astro-ph].

[183] M. Spurio (ANTARES Collaboration). *ANTARES neutrino telescope: status, first results and sensitivity for the diffuse neutrino flux*, 2nd Heidelberg Workshop on High-Energy Gamma-rays and Neutrinos from Extra-Galactic Sources, arXiv:0904.3836 [astro-ph]

[184] J. Brunner. *Antares simulation tools*. VLVnT Workshop on Technical Aspects of a Very Large Volume Neutrino Telescope in the Mediterrenean Sea, Amsterdam, The Netherlands, 5-8 Oct 2003. http://www.vlvnt.nl/proceedings/

[185] N.N.Kalmykov, S.S.Ostapchenko, A.I.Pavlov, Nucl. Phys. B (Proc. Suppl.) 52B (1997) 17.

[186] P. Antonioli, et al., Astrop. Phys. 7 (1997) 357.

[187] M. Ambrosio et al. (The MACRO Collaboration), Phys. Rev. D56 (1997) 1407.

[188] M. Ambrosio et al. (The MACRO Collaboration), Phys. Rev. D56(1997) 1418.

[189] M. Ambrosio et al. (The MACRO Collaboration), Astrop. Phys. 10 (1999) 11.

[190] M. Ambrosio et al. (The MACRO Collaboration), Astrop. Phys. 19 (2003) 313.

[191] M. Ambrosio et al. (The MACRO Collaboration), Phys. Rev. D60 (1999) 032001.

[192] G. Carminati, M. Bazzotti, A. Margiotta and M. Spurio . Comput. Phys. Commun. 179 (2008) 915. arXiv:0802.0562[physics.ins-det]

[193] E.V. Bugaev et al., Phys. Rev. D58 (1998) 054001.

[194] Horandel J., Astrop. Phys. 19 (2003) 193.

[195] C. Bigongiari (ANTARES Collaboration): *Search for steady and transient point-like sources of neutrinos with ANTARES*, 2nd Heidelberg Workshop on High-Energy Gamma-rays and Neutrinos from Extra-Galactic Sources.

[196] A. Romeyer, R. Bruijn, and J.D. de Zornoza: 2003, Proceedings of the 28th International Conference on Cosmic Rays, vol. 3, pp. 13291332.

[197] M. Ambrosio et al. (The MACRO Collaboration), Ap. J. 546 (2001) 1038.

[198] A. Capone et al., *Status of the NEMO Project*. Nucl. Instrum Meth. A602 (2009) 47-53.

[199] E. Migneco et al., *Recent achievements of the NEMO project*. Nucl. Instr. Meth. A588 (2008) 111.

[200] P. Sapienza, http://www.vlvnt.nl/proceedings, Amsterdam (2003).

[201] A. Capone, et al., Nucl. Instrum. Meth. A487 (2002) 423.

[202] F. Ameli, et al., EEE Trans. Nucl. Sci. 55 (2008) 233.

[203] F. Simeone, Nucl. Instrum. Methdods A588 (2008) 119 .

[204] I. Amore et al. *First results from the NEMO Phase-1 experiment*. Nucl. Instrum Meth. A602 (2009) 68-71.

[205] M. Sedita (NEMO Collaboration). Nucl. Instrum. Meth. A567 (2006) 531.

[206] E.G. Anassontzis et al., Nucl. Instrum. Meth. A479 (2002) 439.

[207] G. Aggouras et al., Astrop. Phys. 23 (2005) 377.

[208] 12 R.I. Bagduev et al., Nucl. Instr. Meth. A320 (1999) 139.

[209] S. Kuch, PhD thesis 2007, University of Erlangen, Germany. FAU-PI1-DISS-07-001, www.slac.stanford.edu/spires/find/hep/www?irn=7232764

[210] J. Carr et al. *Configuration studies for a cubic-kilometer deep sea neutrino telescope - KM3NeT- with NESSY, a fast and flexible approach*, Proceedings of 30th Int. Cosmic Ray Conf. July 2007. Merida, Mexico.

[211] U. Katz, *Status of the KM3NeT Project*, Nucl. Instrum Meth. A602 (2009) 40-46.